Experimental Investigations of Magnetohydrodynamic Plasma Jets

Thesis by
Deepak Kumar

In Partial Fulfillment of the Requirements
for the Degree of
Doctor of Philosophy

California Institute of Technology
Pasadena, California

2009

(Defended March 9, 2009)

To the joy and beauty of life.

Acknowledgements

It may seem that completing one's doctoral research is a great personal achievement. While this is certainly the case and I would like to bask in the glory, I would also like to give credit where it is due - to the numerous people who have influenced me in a positive way and helped me during my stay at Caltech.

My stay at Caltech has been extremely enjoyable because of the people I have interacted with, both on and off campus. I had the opportunity to learn karate at the Caltech Karate Club - the first university karate club in the United States. Randy McClure and Pamela Logan were my first instructors. They are champion instructors who made the trainings difficult - and hence fun. The practices were invigorating and taught me the nuances of how best to teach, communicate and motivate. A lot of these skills translated to other aspects of my life. I also had the opportunity to train with many other excellent people related to SKA (Shotokan Karate of America) at our practices, including Mr. Ohshima, Bruce Kanegai, Tom Heyman, David Gabai, Paul Morgan, Dan Sakurai, Kevin Bench, Daniel McSween and numerous others. I am thankful to my current instructor Ian Ferguson for training me in class, especially for tournaments. Over the course of numerous karate practices, I made a lot of friends. Unlike normal friends, they enjoyed hurting me, but I cherished them nonetheless. They include Jon Hartzberg, Tom Livermore, Sasha Tsapin, Peter Ilott, Ted Yu, Udi Vermesh, Charles Cohen, Maria, Michelle Blackway, Eric Wambach, Chris Finch, Tom Mainiero, Rey Rodriguez, Dominic Hougham, Omar Facory, Alexey Solomatin, Raffi, David Berry, Michael Busch, Chip Miller, and others. I would like to thank them all for making practices enjoyable. I will always remember them because of the various bruises and scars they gave me.

I would also like to thank the athletics department at Caltech (especially Howard, Jean Fees, Wendell Jack, and Carlos Basulto) and the facilities management (Anthony Ford and Delmy Emerson) for their constant support to the Caltech Karate Club.

During my stay at Caltech, I got in touch with a few alumni who were building a robot car called "Golem." As a team we participated in the DARPA Grand and Urban Challenges. Even though, I had a very limited role in the team, it was a thrilling experience, and I learned a lot of skills. The people involved with the project were smart and dedicated and made the

whole experience fun. I would like to thank Jim Radford, Richard Mason, Robb Walters, Brian Fulkerson, Bill Caldwell, Dave Caldwell, Dima Kogan, Jim Swenson, Emilio Frazzoli, Josh Arensberg, Eagle Jones, Michael Linderman, Roy Pollock, Ken Kappler, Brandyn Webb, Brent Morgan, Jeff Elings, Izaak Giberson, and other members of the team.

Throughout my research, I often relied on help from representatives from other companies for the maintenance of equipment or getting a new equipment. I am grateful to the following individuals (companies) for their help - Todd Rumbaugh and Frank Kosel (DRS Imaging), Raj Korde (International Radiation Detectors), Dan Gorzen (X-ray and Speciality Instruments), Dr. Matthias Kirsch (Struck Innovative Systeme GmbH), Rolando (APD Cryogenics), Del Munns (DV Manufacturing), and Mark Slattery (Berkeley Nucleonics).

One of the reasons why I enjoyed my time at Caltech was the excellent support from members of the Caltech community. In particular, I would like to thank Rick Germond at facilities stockroom, and Mike Gerfen at central engineering services. Mike was an excellent help with designing and machining most of the parts I used for my experiments. I would also like to thank the administrative assistants at the applied physics department at Caltech - Eleonora Vorobieff, Connie Rodriguez, Irene Loera, Cierina Marks and Mary Metz. It was extremely pleasing to be pampered, as they took care of all the administrative issues I was bothered with. I would also like to thank Jim Endrizzi, Athena Trentin and Tina Lai from the International Student Program office at Caltech. Their support is much appreciated.

I consider myself lucky to have had Dave Felt as an engineer in our lab. Experimental research often involves troubleshooting and reconstructing equipment, and Dave has been a tremendous help with it on numerous occasions. I would also like to thank Doug Strain for writing the software interface for the timing sequencers used in the experiment.

The pace of experimental research is often slow at the beginning and relies on learning good skills from mentors and collaborators. I am indebted to Setthivoine You and Shreekrishna Tripathi for being excellent mentors and helping me get started in the field of plasma physics. They were the postdoctoral scholars in our research group when I joined and were extremely diligent and methodical in upkeep of the experiment.

During my first couple of years at Caltech, I shared an office with senior graduate students - Eli Jorné, Carlos Romero-Talamás and Steve Pracko. They ensured that the office was a lively place - somewhere I looked forward to come to every morning. The office banter was lighthearted and fun, even though I was the target of most of the office jokes.

Over the last three to four years of my stay at Caltech, I also had the opportunity to collaborate with new graduate student members of our research group - Rory Perkins, Auna Moser, Eve Stenson, Mark Kendall, Bao Ha and Vernon Chaplin. It was wonderful to collaborate with Rory on our quest to understand the origin of the X-rays in our experiment. I am also grateful to him for proof reading parts of this thesis and for other physics discussions we have had over the years. Auna carried on the tradition of keeping the office a lively place. I am thankful to her for the various upkeep and calibrations she performed on the spheromak experiment. I would also like to acknowledge the feedback from Vernon while he proofread most of this thesis. It was fun to get to know Eve, and I will certainly miss the cookies she used to bring to the lab. Mark and Bao brought a young positive energy to the group. Their help in maintaining the computing infrastructure in the group is gratefully acknowledged.

I would like to acknowledge the helpful tips and guidance from other scientists during my research - Freddy Hansen, Scott Hsu, Uri Shumlak, Brian Nelson, Raymond Golingo, Tony Peebles, Terry Rhodes, Simon Woodruff, Richard Lovelace, Hui Li, Mike VanZeeland, Carl Sovinec, William Bridges and Heun-Jin Lee.

I would also like to acknowledge Raffi Nazikian, Alan Hoffman, Cary Forest, Tom Jarboe, Troy Carter, Walter Gekelman, and Dave Hammer for inviting me to present my research during the last year. My presentation skills improved with each such opportunity as I received positive feedback from the audience. I am also grateful to them for sharing ideas and showing me their experiments.

I would also like to thank the members of my candidacy committee (Prof. Giapis, Prof. Vahala, Prof. Rutledge, and Prof. Bellan) and the members of my thesis committee (Prof. Gould, Prof. Shepherd, Dr. Meier, and Prof. Bellan) for their tips and feedback on the thesis and presentation.

Completing the doctoral research is similar to running a marathon. It requires strong determination and continuous effort for extended periods of time. During hard times, words of support and encouragement help a lot. I would like to thank family and friends for their continuous zealous support. I am blessed to have a lot of caring friends, but would like to acknowledge a few of them in particular - my parents, Sonal, Sabiha, Ila and Zuma.

Last but not least, I would like to acknowledge the mentor-ship of the two most helpful people in my research - Paul Bellan and Gunsu Yun. Gunsu was a graduate student in our lab. He is an excellent experimentalist, and I had the great fortune of collaborating with him on many occasions. He single-handedly performed many upgrades to the experimental setup. Paul has been a constant help throughout my stay at Caltech, and no words can do justice to the positive impact he has had on me when it comes to doing research. I have always been impressed by his knowledge and skills; however, his patience, diligence and dedication have been even more motivating.

Abstract

This thesis primarily focuses on understanding the plasma behavior during the helicity injection stage of a pulsed spheromak experiment. Spheromak formation consists of a series of dynamic steps whereby highly localized plasma near the electrodes evolves toward a Taylor state equilibrium. The dynamical evolution stage has been modeled as a series of equilibrium states in the past. However, the experiments at the Caltech spheromak facility have revealed that unbalanced $\mathbf{J} \times \mathbf{B}$ forces drive non equilibrium Alfvénic flows during these preliminary stages.

The Caltech spheromak experiment uses coplanar electrodes to produce a collimated plasma jet flowing away from the electrodes. The jet formation stage precedes the spheromak formation and serves as a mechanism for feeding particles, magnetic helicity, energy, and toroidal flux into the system. Detailed density and flow velocity measurements of hydrogen and deuterium plasma jets have revealed that the jets are extremely dense with $\beta_{\text{thermal}} \sim 1$. Furthermore, the flow velocity was found to be Alfvénic with respect to the the toroidal magnetic field produced by the axial current within the plasma. An existing magnetohydrodynamics (MHD) model has been generalized to successfully predict the effect of plasma current on the jet's density and flow velocity. The behavior of these laboratory jets is in stark contrast to the often considered model for astrophysical jets describing them as equilibrium configurations with hollow density profiles.

Other contributions of this thesis include the following.

1. The thesis presents an analytical proof that resistive MHD equilibrium with closed flux tubes is not feasible. This implies that sustained spheromak experiments cannot maintain helicity while being in a strict equilibrium.

2. The thesis describes measurements to characterize the circuit parameters of the high voltage discharge circuit used in the Caltech spheromak experiment.

3. The thesis also describes the setup of novel He-Ne laser interferometers used to measure the density of plasma jets. The ease of alignment of these interferometers was greatly enhanced by having unequal path lengths of the scene and reference beams.

4. Finally, the thesis details the setup for a soft X-ray (SXR)/Vacuum ultra violet (VUV)

imaging system. Some preliminary images of reconnecting flux tubes captured by the imaging setup are also presented.

Contents

List of Figures

List of Tables

Chapter 1

Introduction

Plasma is an ionized gas. Some of the applications of plasma physics are fusion energy research, plasma processing, arcs, space propulsion, and understanding many solar and astrophysical phenomena.

The fusion reaction between deuterium and tritium has the highest reaction rate [1] ($\sim 10^{-22}$ m^3/s) at moderately high temperatures (~ 10 keV). It yields $E_{\text{reaction}} = 17.6$ MeV per reaction.

$$\mathrm{D} + \mathrm{T} \rightarrow \mathrm{He}^4(3.5\ \mathrm{MeV}) + \mathrm{n}(14.1\ \mathrm{MeV}).$$

To achieve fusion, hot and dense D-T plasma has to be confined long enough for substantial fusion reactions to occur. A fusion reactor will be profitable if the energy spent in confining the hot plasma is less than the energy output from the fusion reaction. This argument is used to derive the Lawson criterion

$$n\tau_E \gtrsim \frac{kT}{E_{\text{reaction}} \ \times \ \text{reaction rate}} \sim 10^{20} - 10^{21}\ \text{sec} \times \text{m}^3, \tag{1.1}$$

where n is the plasma density, τ_E is the energy confinement time, and T is the temperature of the plasma. A tokamak is a donut shaped device that confines hot plasma particles on toroidal magnetic flux surfaces. The tokamak concept is the most widely pursued magnetic fusion reactor design. The ITER device [2] being built in Cadarache, in the South of France is an experimental reactor which is expected to demonstrate an energy efficiency of 10 by confining hot plasma ($T \sim 10$ keV, $n \sim 10^{20}$ m^{-3}) with confinement time of ~ 4 s (the experimental pulse will be substantially longer ~ 500 s). However, there are huge technological and monetary constraints for building tokamak reactors. The budget of ITER is approximately 10 billion US dollars.

Spheromaks [3] are simply connected (and hence topologically simple) plasma configurations which may provide a cheaper alternative to other fusion reactor designs. The Sustained Spheromak Physics Experiment (SSPX) at the Lawrence Livermore National Laboratory has been the most successful spheromak experiment to date. It achieved plasma temperatures of few 100 eV and $n\tau_E$ approximately three orders of magnitude less than the Lawson criterion [4] described in equation (1.1). Huge improvement in the spheromak performance is required to make it a viable fusion reactor. The progress in the last three decades has been exceptional and substantial progress is expected in near future.

Spheromaks configurations are constrained minimum energy states, and thus plasmas have a natural tendency of evolving toward a spheromak equilibrium. Thus, concepts of spheromak research have often been used to explain plasma behavior in many naturally evolving plasma structures, for example solar prominences [5] and astrophysical jets [6].

1.1 Magnetohydrodynamics-MHD

Magnetohydrodynamics (MHD) is a description of the plasma which models it as an electrically conducting fluid [7, Chapter 2.6]. A MHD description of plasma behavior is valid under the following assumptions:

1. Plasma is charge neutral. This is true when considering plasma behavior at length scales much greater than the Debye length.
2. The plasma is collisional, or equivalently the collision times are much shorter than the characteristic timescales of the experiment. This ensures that the particle distribution is Maxwellian.
3. The plasma behavior under consideration has velocity much smaller than the speed of light.
4. Either the timescales under consideration are much longer than the ion cyclotron frequency or the electron cyclotron frequency is much smaller than the electron-ion collision frequency.

5. The pressure and density gradients are parallel in the plasma.

The mass conservation equation in MHD is

$$\frac{\partial \rho}{\partial t} + \nabla \cdot (\rho \mathbf{u}) = 0, \tag{1.2}$$

where ρ is the mass density of the plasma and $\mathbf{u}$ is its velocity. The MHD equation of motion is

$$\rho \left(\frac{\partial \mathbf{u}}{\partial t} + \mathbf{u} \cdot \nabla \mathbf{u} \right) = \mathbf{J} \times \mathbf{B} - \nabla P, \tag{1.3}$$

where $\mathbf{J}$ is the current density, $\mathbf{B}$ is the magnetic field and P the fluid pressure. Using equation (1.2), the left hand side of equation (1.3) can be expressed as

$$\begin{aligned} \rho \left(\frac{\partial \mathbf{u}}{\partial t} + \mathbf{u} \cdot \nabla \mathbf{u} \right) &= \frac{\partial (\rho \mathbf{u})}{\partial t} + \nabla \cdot (\rho \mathbf{u} \mathbf{u}) - \left[\frac{\partial \rho}{\partial t} + \nabla \cdot (\rho \mathbf{u}) \right] \mathbf{u} \\ &= \frac{\partial (\rho \mathbf{u})}{\partial t} + \nabla \cdot (\rho \mathbf{u} \mathbf{u}) . \end{aligned}$$

Thus, the MHD equation of motion can be expressed in the following alternative form

$$\frac{\partial (\rho \mathbf{u})}{\partial t} + \nabla \cdot (\rho \mathbf{u} \mathbf{u}) = \mathbf{J} \times \mathbf{B} - \nabla P. \tag{1.4}$$

MHD Ohm's law is

$$\mathbf{E} + \mathbf{u} \times \mathbf{B} = \eta \mathbf{J}, \tag{1.5}$$

where $\mathbf{E}$ is the electric field in the plasma and η is its resistivity. In a plasma with negligible resistivity, the MHD Ohm's law can be used to show that the magnetic flux linked by any closed loop in the plasma is conserved.

The MHD heat transport equation [7, page 73],[8, section 10.6] is

$$\begin{aligned} \frac{\partial}{\partial t} \left(\frac{NP}{2} + \frac{\rho u^2}{2} \right) + \nabla \cdot \left(\mathbf{q} + \frac{(N+2)P}{2} \mathbf{u} + \frac{\rho u^2}{2} \mathbf{u} \right) &= \mathbf{J} \cdot \mathbf{E} - S_l \\ &= \eta J^2 - \mathbf{J} \cdot (\mathbf{u} \times \mathbf{B}) - S_l, \end{aligned} \tag{1.6}$$

where N is the dimensionality of the system (usually $N = 3$), $\mathbf{q}$ is the heat flux, and S_l is the rate of energy loss by radiation.

1.1.1 Energy Conservation in MHD

Dotting electric field $\mathbf{E}$ with the pre-Maxwell form of Ampere's law gives

$$\mathbf{E} \cdot \nabla \times \mathbf{B} = \mu_\circ \mathbf{J} \cdot \mathbf{E}.$$

Similarly, dotting the magnetic field with Faraday's law gives

$$\mathbf{B} \cdot \nabla \times \mathbf{E} = -\frac{\partial \mathbf{B}}{\partial t} \cdot \mathbf{B}.$$

Subtracting these two equations and using the vector identity $\nabla \cdot (\mathbf{E} \times \mathbf{B}) = \mathbf{B} \cdot \nabla \times \mathbf{E} - \mathbf{E} \cdot \nabla \times \mathbf{B}$ gives

$$\nabla \cdot \left(\frac{\mathbf{E} \times \mathbf{B}}{\mu_\circ} \right) = -\frac{\partial}{\partial t} \frac{B^2}{2\mu_\circ} - \mathbf{J} \cdot \mathbf{E}.$$

Using equation (1.6) gives

$$\nabla \cdot \left(\frac{\mathbf{E} \times \mathbf{B}}{\mu_\circ} + \frac{\rho u^2}{2} \mathbf{u} + \frac{(N+2)P}{2} \mathbf{u} + \mathbf{q} \right) = -\frac{\partial}{\partial t} \left(\frac{B^2}{2\mu_\circ} + \frac{\rho u^2}{2} + \frac{NP}{2} \right) - S_l.$$

This can be integrated over the entire volume of plasma and over time. By Gauss' law, the volume integral of the terms on the left-hand side turns into a surface integral. If the plasma velocity is zero at the boundary of the volume, the surface integration terms involving the plasma velocity are zero as well. Assuming that there is no heat flux at the boundary, we get

$$\underbrace{\int_0^t \mathrm{d}\mathbf{s} \cdot \left(\frac{\mathbf{B} \times \mathbf{E}}{\mu_\circ} \right)}_{W_{\text{input}}} = \underbrace{\int \frac{B^2}{2\mu_\circ} \mathrm{d}^3 r}_{W_{\text{mag}}} + \underbrace{\int \frac{\rho u^2}{2} \mathrm{d}^3 r}_{W_{\text{kin}}} + \underbrace{\int \frac{NP}{2} \mathrm{d}^3 r}_{W_{\text{th}}} + \underbrace{\int \left(\int_0^t S_l \, \mathrm{d}t \right) \mathrm{d}^3 r}_{W_{\text{radiation-loss}}}. \tag{1.7}$$

equation (1.7) is the MHD energy conservation equation. Note that d$\mathbf{s}$ is pointing outwards from volume bounding the plasma. The left-hand term (W_{input}) is the energy input into the plasma and is the surface integral of the Poynting flux over time. If the plasma is bounded by electrodes which link external current, then W_{input} can also be expressed as $\int_0^t VI \mathrm{d}t$. V is the voltage at the electrodes, and I is the current linked by the electrodes. W_{kin} is the kinetic energy in the plasma and W_{th} is the thermal energy. The thermal energy of the plasma can be increased by adiabatic compression or from Ohmic heating from the ηJ^2

term in equation (1.6). $W_{\text{radiation-loss}}$ accounts for the radiation losses in the plasma. The energy lost in radiation also comes from the Ohmic term ηJ^2. W_{mag} is the energy in the magnetic field in the plasma. In case of azimuthically symmetric plasma configurations, W_{mag} can be expressed as the sum of toroidal and poloidal field energies.

$$\underbrace{\int \frac{B^2}{2\mu_\circ} \mathrm{d}^3 r}_{W_{\text{mag}}} = \underbrace{\int \frac{B_{\text{tor}}^2}{2\mu_\circ} \mathrm{d}^3 r}_{W_{\text{tor}}} + \underbrace{\int \frac{B_{\text{pol}}^2}{2\mu_\circ} \mathrm{d}^3 r}_{W_{\text{pol}}} . \tag{1.8}$$

1.2 Helicity Injection and Spheromak Formation

Magnetic helicity in a plasma is defined as

$$K = \int \mathbf{A} \cdot \mathbf{B} \mathrm{d}^3 r,$$

where $\mathbf{A}$ is the magnetic vector potential. Magnetic helicity as defined above is gauge invariant if there is no normal magnetic field component on the surface bounding the volume under consideration. However, this condition is not satisfied in most spheromak experiments. For such scenarios, an alternate concept of relative helicity is used [3, Section 3.5].

$$K_{\text{rel}} = \int \left(\mathbf{A} \cdot \mathbf{B} - \mathbf{A}_{\text{vac}} \cdot \mathbf{B}_{\text{vac}} \right) \mathrm{d}^3 r,$$

where $\mathbf{A}_{\text{vac}}$ and $\mathbf{B}_{\text{vac}}$ are the vacuum solutions to the magnetic vector potential and the magnetic field inside the volume, and $\mathbf{B}_{\text{vac}}$ satisfies the same boundary conditions as $\mathbf{B}$. The dissipation of relative helicity by plasma resistivity and its implications on plasma equilibrium is considered in chapter 2.

Woltjer [9] showed that the helicity is conserved in an ideal plasma, and conjectured that in a slightly resistive plasma, magnetic helicity is nearly a constant in the time scale of decay of magnetic energy. He considered a plasma with negligible thermal energy ($P \to 0$), and used a variational principle to show that the minimum energy state satisfying the constraint of constant helicity is characterized by

$$\nabla \times \mathbf{B} = \lambda \mathbf{B}, \tag{1.9}$$

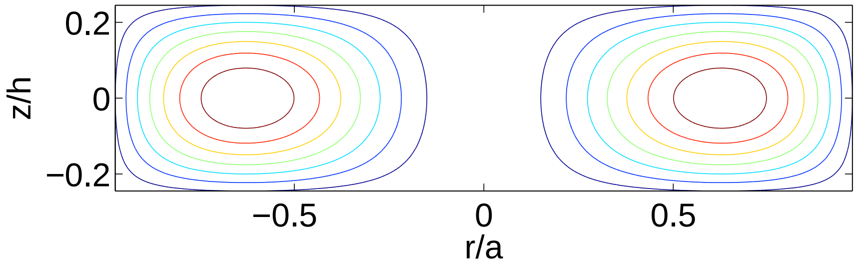

Figure 1.1: Closed poloidal flux surfaces in an isolated spheromak in a cylindrical flux conserver with aspect ratio $r/z = 1.9$.

where λ is constant throughout the volume. Plasmas defined by equation (1.9) are often called force-free plasmas, as equation (1.3) shows that there are no forces in a uniform plasma if current density is parallel to the magnetic field.

Taylor [10] argued that magnetic reconnection conserves the total magnetic helicity in a plasma, but lowers the magnetic energy to a force-free plasma state. He used this hypothesis to explain the spontaneous existence of a reversed toroidal field in a toroidal device called a reversed field pinch (RFP).

The relative magnetic helicity conservation equation is

$$\frac{\mathrm{d}K_{rel}}{\mathrm{d}t} + \int_{\partial\mathcal{V}} (2V\mathbf{B}) \cdot \mathrm{d}\mathbf{n} = -2\int_{\mathcal{V}} \eta\mathbf{J} \cdot \mathbf{B}\mathrm{d}^3 r.$$

It shows that magnetic helicity can be injected into a plasma by maintaining an electric potential difference V across open magnetic field lines on its boundary $\partial\mathcal{V}$. This is the most common technique for helicity injection in spheromak plasmas and is called electrostatic helicity injection. Initial spheromak experiments were non steady-state experiments which involved electrostatic helicity injection and relaxation of the plasma into a force-free state in a flux conserver. The eigenvalue λ in the force-free equation (1.9) is determined by the shape of the flux conserver. Spheromak plasmas in the flux conserver can have closed flux surfaces which are beneficial for particle confinement. Figure 1.1 shows an example of the closed poloidal flux contours in a cylindrical flux conserver.

Helicity can also be injected in a spheromak experiment in steady state. Figure 1.2 shows the open and closed flux surfaces in a steady state spheromak. Particle confinement is expected to be good on the closed flux surfaces, however chapter 2 shows that such a

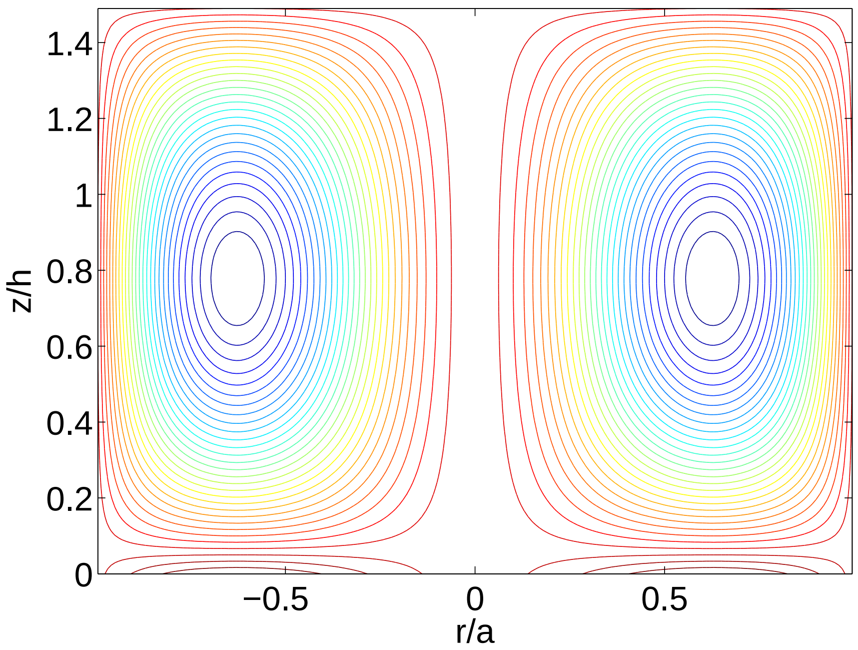

Figure 1.2: Open and closed poloidal flux surfaces in an steady state spheromak in a cylindrical flux conserver with aspect ratio $r/z = 0.67$.

system can not be in a strict equilibrium. Magnetic helicity conservation in a steady state spheromak was experimentally demonstrated by Barnes et al. [11].

1.3 Overview of the Caltech Spheromak Experiment

The Caltech spheromak experiment is a pulsed helicity injection experiment without a flux conserver. The experiment employs a coaxial planar electrode design for helicity injection. Figure 1.3 shows the design of the electrodes. The setup is installed inside a cylindrical vacuum chamber with length ~ 1.6 m and diameter ~ 1.4 m. The inner disk cathode is 20 cm in diameter, and the outer annular anode has a diameter of 50 cm. Plasma is created by discharging up to two high voltage 59 μF capacitors across the electrodes. Details of the discharge circuit are presented in chapter 3.

Throughout this thesis, a cylindrical coordinate system $\{r, \phi, z\}$ is considered while describing plasma dynamics in the spheromak experiment. The z axis is coming out of the plane of the figure 1.3, r axis points radially outwards from the center of the electrodes, and ϕ is the toroidal direction to form a right-handed coordinate system around the z axis.

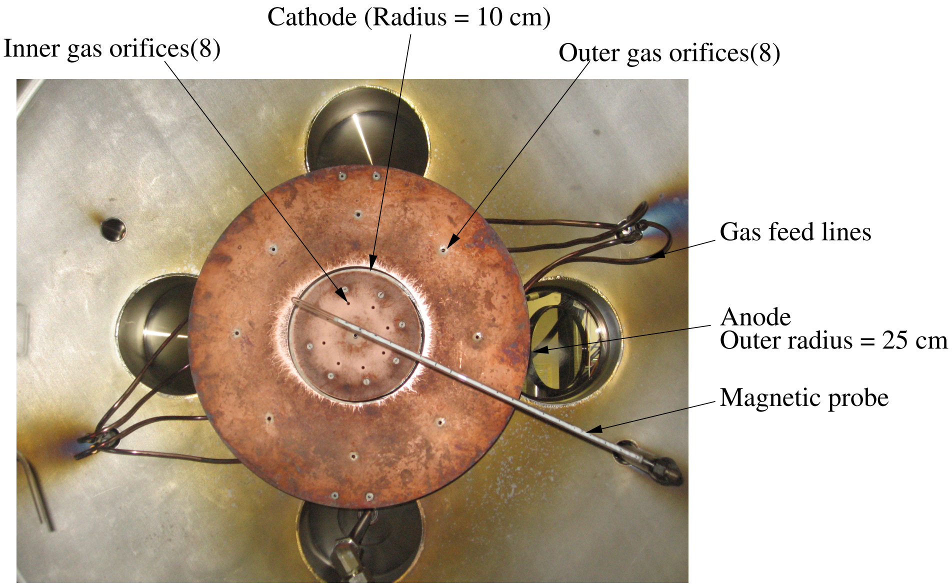

Figure 1.3: Electrodes in the Caltech spheromak experiment.

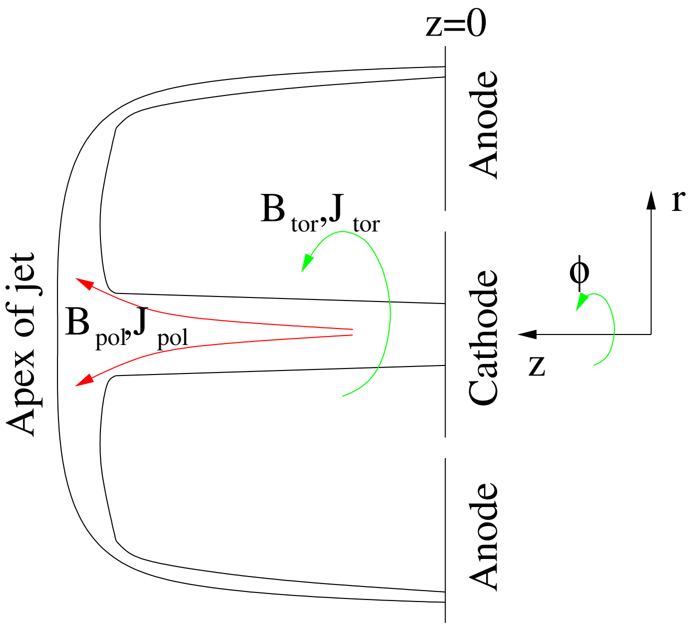

Figure 1.4: Cartoon showing the definition of the cylindrical coordinate system for the Caltech spheromak experiment. The red arrows represent the poloidal $r - z$ direction, and the green arrows represent the toroidal ϕ direction. The poloidal current in the experiment is driven by an external capacitor bank linked to the electrodes. The poloidal current creates a toroidal magnetic field. An external magnetic field coil (see figure 1.5) creates a poloidal magnetic field in the experiment.

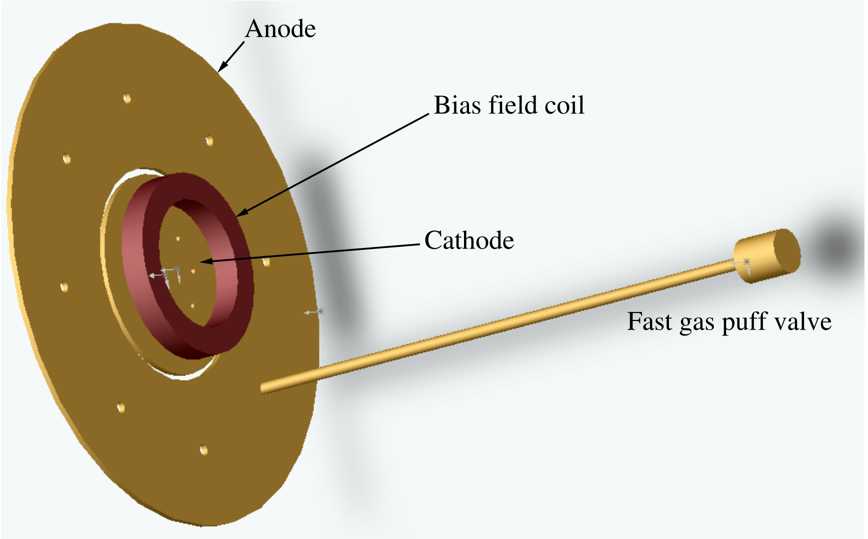

Figure 1.5: Cartoon showing the location of bias field coil behind the cathode of the Caltech spheromak experiment. Also shown is the location of a fast gas puff valve. Image courtesy of Paul Bellan.

The electrodes are located at $z = 0$. Vectors which lie in the $r - z$ plane are referred to as poloidal vectors. Vectors oriented along the $\hat{\phi}$ direction are referred to as toroidal vectors. Poloidal and toroidal vectors are often referred to by subscripts "pol" and "tor" respectively. Also, scalar quantities which are independent of ϕ are referred to as poloidal. The coordinate system is described in figure 1.4.

A poloidal vacuum magnetic field created by a 2.8 mH coil behind the electrodes links the two electrodes (see figure 1.5). The coil was powered by an electrically isolated 14.4 mF capacitor bank. The voltage of the capacitor bank could be varied to create a magnetic flux of up to 4.9 mWb at the cathode. The applied flux remains constant for the time scale of the experiment and is referred to as the poloidal bias flux.[1] Changing the direction of the bias flux did not cause any change in the plasma behavior in the experiment.

Neutral gas was puffed near the electrodes using 16 orifices, eight each on the two electrodes (see figure 1.5). Two fast gas puff valves [3, Chapter 14] each were used to supply neutral gas at the anode and the cathode.

The following sequence of events was followed to create a plasma discharge (refer to

---

[1] Calibration of the poloidal bias flux was done by Auna Moser, Gunsu Yun, and Deepak Kumar.

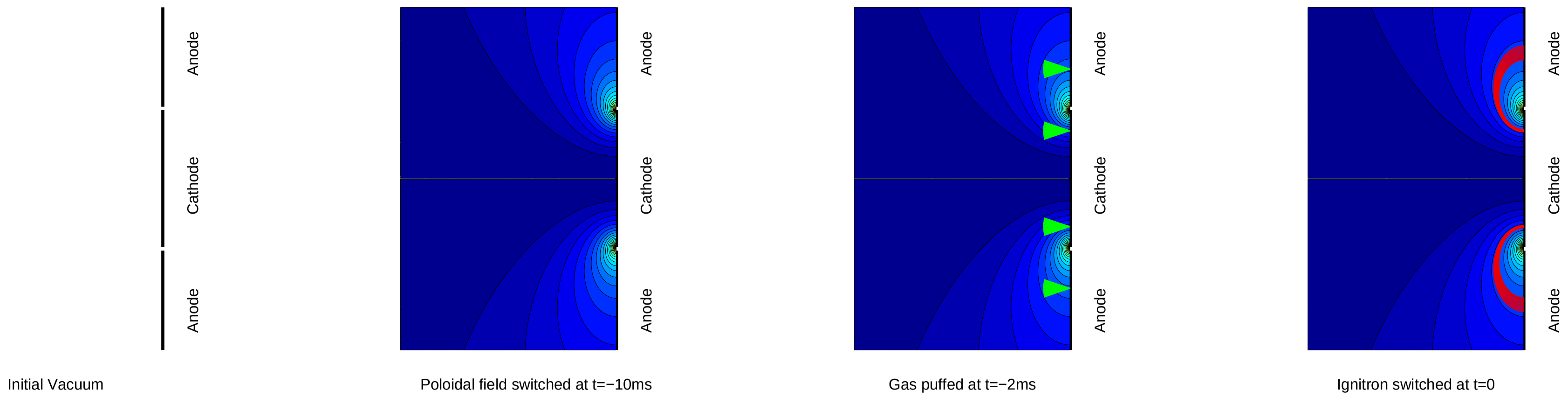

Initial Vacuum

Poloidal field switched at t=−10ms

Gas puffed at t=−2ms

Ignitron switched at t=0

Figure 1.6: Cartoon showing the sequence of events leading to plasma breakdown in the Caltech spheromak experiment. The figures show: (a) Initial vacuum in front of the electrodes, (b) Poloidal flux surfaces created by the bias coil, (c) Neutral gas (green) being puffed near the electrodes, and (d) Spider leg formation (plasma is represented by red color) from neutral gas breakdown.

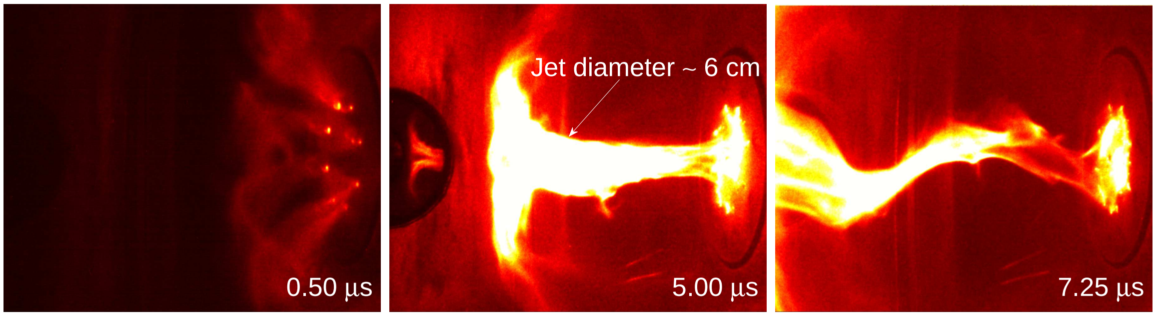

(a) Eight spider legs (b) Collimated jet (c) Kink unstable jet

Figure 1.7: Visual images of the three distinct stages of plasma evolution in the Caltech spheromak experiment.

figure 1.6):

1. The poloidal flux power supply was triggered 10 ms before the plasma discharge. It takes 10 ms for the magnetic field to reach its maximum and link the two electrodes.
2. Fast gas valves were triggered ~ 2 ms before the plasma discharge. It takes ~ 2 ms for neutral gas to travel from the fast gas puff valves to the orifices.
3. The high voltage capacitor bank was discharged across the electrodes to create a plasma. Initially the plasma links the gas nozzle along poloidal magnetic field lines. The eight plasma filled flux tubes linking the two electrodes resemble the eight legs of a spider as shown in figure 1.7(a). The capacitor bank drives a poloidal current through the plasma (see figure 1.4), which creates a toroidal magnetic field.
4. The various diagnostics and the digitizers were triggered upon the neutral gas breakdown near the electrodes.

Figure 1.7, shows the typical stages in plasma evolution after the breakdown - eight “spider legs” linking the electrodes, a collimated plasma jet, and a kink unstable plasma column. The structure of the spider legs was investigated by You et al. [12]. The properties of the collimated jet are described in chapter 5 of this thesis. The kink instability of the plasma jets was studied by Hsu and Bellan [13].

1.3.1 Diagnostics

The following diagnostics were used in the experiment:

1. A Tektronix P6015 [14] high-voltage probe was used to measure the potential difference across the electrodes.

2. A Rogowski coil [3, Chapter 15] was used to measure the current flowing through the high voltage capacitor bank.

3. Imacon 200-a high speed imaging camera manufactured by DRS Technologies [15] - was used to take visible images of the plasma.

4. A He-Ne laser interferometer to measure the density of the plasma jets. Details of the interferometer are described in Chapter 4.

5. A 60-element magnetic probe array [16] was used to measure the magnetic field in the experiment (see figure 1.3). The probe measured magnetic field along $\{r, \phi, z\}$ directions at 20 different radial locations separated by 2 cm. The axial position (distance from the electrodes along the z direction) of the probe could be varied. Assuming toroidal symmetry, the Ampere's law can be used to calculate the poloidal current from the toroidal magnetic field measurements:

   $$I(r,z) = \frac{2\pi r B_\phi(r,z)}{\mu_\circ}.$$

   The poloidal current $I(r,z)$ is calculated only at discrete radii, corresponding to the location of the measurement coils in the magnetic probe.

   The poloidal flux can be calculated using

   $$\psi(r,z) = \int_0^r B_z(r',z) 2\pi r' \mathrm{d}r'. \tag{1.10}$$

   The integration over discrete radial locations in equation (1.10) may introduce substantial errors. Also, the calculation of poloidal current and flux assumes that the magnetic probe is oriented along the radial direction. However, there is no mechanism to ensure this accurately.

1.3.2 Experimental Parameters and Dimensionless Numbers

Table 1.1: Measured parameters for the plasma jets

Symbol (Parameter)	Value	Comment
τ timescale of the jet	$5 - 10\ \mu$s	Experimentally observed.
l length of the jet	~ 0.3 m	Inferred from visual plasma images. See figure 1.7(b).
r radius of the jet	~ 0.03 m	Inferred from visual plasma images. See figure 1.7(b).
n plasma density	$\sim 3 \times 10^{22}$ m^{-3}	Described in chapter 4.
B magnetic field	$0.1 - 0.2$ T	By magnetic probe measurements [16].
T_i ion temperature	~ 2 eV	By spectroscopic measurements [17, Page 79].
T_e electron temperature	~ 2 eV	The electron and ion temperatures are expected to equilibrate because the plasma is highly resistive. $\nu_{ei} \gg \tau^{-1}$ (Table 1.2).
u_z jet axial velocity	~ 40 km/s	Described in chapter 5.

Table 1.1 shows some of the experimentally measured parameters of the plasma jets. These parameters were used to derive the quantities listed in Table 1.2.[2]

---

[2] Rory Perkin's help in formulating this table is greatly acknowledged.

Table 1.2: Some derived quantities for the plasma jets

Symbol	Parameter	Formula	Value
v_{Ti}	ion thermal velocity	$\left(\frac{2kT_i}{m_i}\right)^{\frac{1}{2}}$	~ 20 km/s
v_{Te}	electron thermal velocity	$\left(\frac{2kT_e}{m_e}\right)^{\frac{1}{2}}$	~ 800 km/s
λ_D	Debye length	$\left(\frac{\varepsilon_\circ kT}{nq^2}\right)^{\frac{1}{2}}$	$\sim 0.1\ \mu$m
Λ	particles in a Debye sphere	$n\frac{4\pi}{3}\lambda_D^3$	~ 100
ν_{ei}	collision rate	$\frac{nq^4}{2\pi\varepsilon_\circ^2 m_e^{\frac{1}{2}}(2kT_e)^{\frac{3}{2}}}$	~ 300 GHz
η	plasma resistivity	$\frac{m_e\nu_{ei}}{nq^2}$	$\sim 3\times10^{-4}\ \Omega$m
ω_{ce}	electron cyclotron frequency	$\frac{qB}{m_e}$	$\sim 2\times10^{10}$ rad/s
ω_{ci}	ion cyclotron frequency	$\frac{qB}{m_e}$	$\sim 10^7$ rad/s
ω_{pe}	electron plasma frequency	$\left(\frac{nq^2}{m_e\varepsilon_\circ}\right)^{\frac{1}{2}}$	$\sim 10^{13}$ rad/s
ω_{pi}	ion plasma frequency	$\left(\frac{nq^2}{m_i\varepsilon_\circ}\right)^{\frac{1}{2}}$	$\sim 2\times10^{11}$ rad/s
r_e	electron gyroradius	$\frac{v_{Te}}{\omega_{ce}}$	$\sim 50\ \mu$m
r_i	ion gyroradius	$\frac{v_{Ti}}{\omega_{ci}}$	~ 0.2 cm
D_B	Bohm diffusion coefficient	$\frac{1}{16}\frac{kT_e}{qB}$	~ 1 m^2/s
τ_B	Bohm time	$\frac{r^2}{2D_B}$	$\sim 500\ \mu$s
δ_p	plasma skin depth	$\frac{c}{\omega_{pe}}$	$\sim 30\ \mu$m
R_m	magnetic Reynold's number	$\frac{u_z r}{\eta}$	$\sim 10^6$

Chapter 2

On Magnetic Helicity Injection in a Steady State Scenario

Many driven plasma experiments consist of closed flux surfaces maintained by externally linked currents along open field lines linking the electrodes. This chapter shows that it is not possible to sustain magnetic helicity in such configurations with static magnetic fields.

Consider an externally driven resistive MHD plasma in a simply connected volume $\mathcal{V}$ bounded by a perfect conductor with gaps (see figure 2.1). A driven configuration attempts to sustain magnetic helicity in the plasma by having open magnetic field lines linking boundary surfaces at different potentials (electrostatic helicity injection) or by generating time dependent surface potential and magnetic fields inductively (AC helicity injection). Such systems have been used in many sustained spheromak experiments for both electrostatic helicity injection [11, 18, 19] and AC helicity injection [20]. This chapter examines whether a truly static equilibrium is possible for such driven systems.

Consider the relative magnetic helicity conservation equation in a resistive plasma [3, Chapter 3]

$$\frac{\mathrm{d}K_{rel}}{\mathrm{d}t} + \int_{\partial\mathcal{V}} (2V\mathbf{B}) \cdot \mathrm{d}\mathbf{n} = -2\int_{\mathcal{V}} \eta \mathbf{J} \cdot \mathbf{B} \mathrm{d}^3 r. \tag{2.1}$$

For further analysis, the volume of plasma is divided into open and closed flux tubes as shown in figure 2.1. The open flux tube links electrodes having different potentials V_+ and V_- respectively. An external source drives a current $I_\circ$ through the open flux tube. The potential appearing at the electrodes is the cumulative effect of the resistive drop across the open flux tube and also inductive voltages from the self inductance of the open flux tube and

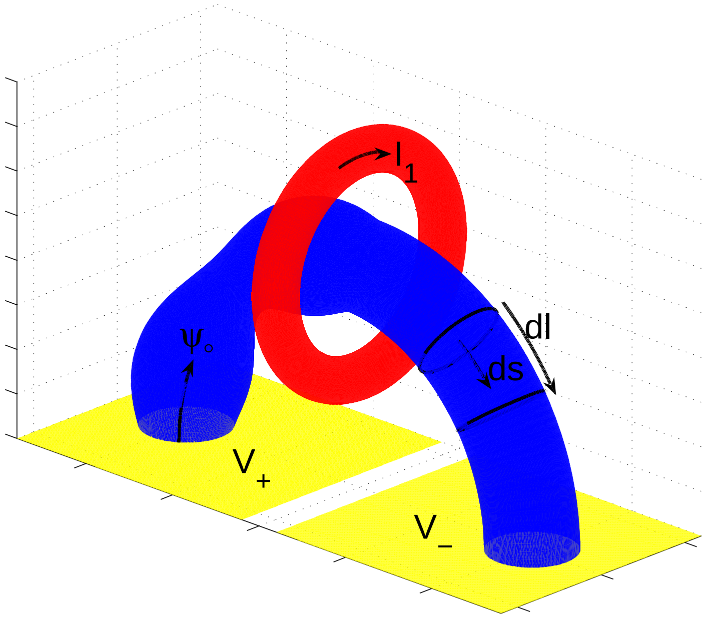

Figure 2.1: A cartoon showing an open flux tube (in blue) having a flux $\psi_\circ$ and an externally linked current $I_\circ$. The volume in red is a closed flux tube carrying a current I_1.

mutual inductance from the closed flux tube. For simplicity, we will consider just a single open flux tube with infinitesimally small cross section, but the arguments presented in this chapter can be extended to more than one open flux tube. Consider the right-hand-side term of equation (2.1) within the volume $\mathcal{V}_\circ$ of the open flux tube (blue region in figure 2.1):

$$\begin{aligned} -2\int_{\mathcal{V}_\circ} \eta \mathbf{J}\cdot\mathbf{B}\mathrm{d}^3r &= -2\int_{\mathcal{V}_\circ} (\mathbf{E}+\mathbf{U}\times\mathbf{B})\cdot\mathbf{B}\mathrm{d}^3r \\ &= -2\int_{\mathcal{V}_\circ} \mathbf{E}\cdot\mathbf{B}\mathrm{d}^3r \\ &= -2\int_{\mathcal{V}_\circ} (-\nabla V - \frac{\partial \mathbf{A}}{\partial t})\cdot\mathbf{B}\mathrm{d}^3r. \end{aligned} \tag{2.2}$$

The first term in equation (2.2) can be expressed as

$$2\int_{\mathcal{V}_\circ} \nabla V\cdot\mathbf{B}\mathrm{d}^3r = 2\int_{\mathcal{V}_\circ} \nabla\cdot(V\mathbf{B})\,\mathrm{d}^3r = 2\int_{\partial\mathcal{V}_\circ} V\mathbf{B}\cdot\mathrm{d}\mathbf{n},$$

which is exactly equal to the electrostatic helicity injection term in equation (2.1). The second term in equation (2.2) can be expressed as

$$2\int_{\mathcal{V}_\circ}\frac{\partial\mathbf{A}}{\partial t}\cdot\mathbf{B}\mathrm{d}^3r=2\int_{\mathcal{V}_\circ}\frac{\partial\mathbf{A}}{\partial t}\cdot\mathbf{B}\mathrm{d}\mathbf{l}\cdot\mathrm{d}\mathbf{s}=2\int_{\mathcal{V}_\circ}\frac{\partial\mathbf{A}}{\partial t}\cdot\mathrm{d}\mathbf{l}\mathbf{B}\cdot\mathrm{d}\mathbf{s}=2\psi_\circ\int_{\mathcal{V}_\circ}\frac{\partial\mathbf{A}}{\partial t}\cdot\mathrm{d}\mathbf{l},\tag{2.3}$$

where $\mathrm{d}\mathbf{l}$ and $\mathrm{d}\mathbf{s}$ are infinitesimal length and area elements along the open flux tube (refer to Fig. 2.1) and $\psi_\circ=\mathbf{B}\cdot\mathrm{d}\mathbf{s}$ is the flux, which is constant throughout the length of the flux tube. In deriving equation (2.3) we used the fact that $\mathrm{d}\mathbf{l}$, $\mathrm{d}\mathbf{s}$ and $\mathbf{B}$ are parallel to each other in the flux tube.

Thus equation (2.1) can be rewritten as

$$\frac{\mathrm{d}K_{rel}}{\mathrm{d}t}-2\psi_\circ\int_{\mathcal{V}_\circ}\frac{\partial\mathbf{A}}{\partial t}\cdot\mathrm{d}\mathbf{l}=-2\int_{\mathcal{V}-\mathcal{V}_\circ}\eta\mathbf{J}\cdot\mathbf{B}\mathrm{d}^3r.\tag{2.4}$$

Note that the helicity source terms in equation (2.4) depend on a time-dependent magnetic vector potential. This shows that helicity cannot be sustained in a driven plasma having closed flux surfaces ($\mathcal{V}-\mathcal{V}_\circ\neq 0$) with the plasma being in static equilibrium. Equation (2.4) also shows that a resistive MHD equilibrium is not possible in a plasma containing closed flux tubes (surfaces).

It is often considered that the rate of helicity injection into the plasma is proportional to the voltage appearing across the electrodes with open field lines. However, equation (2.4) clearly shows that meaningful helicity is injected only by the fluctuating voltage appearing at the electrodes and not by the voltage caused by the resistive drop across the plasma.

A time-changing magnetic vector potential implies a time changing current distribution in the plasma. Equivalently, it implies fluctuating topological changes in the plasma. High node number ($n\neq 0$) modes and turbulent fluctuations have been observed in sustained spheromak experiments during helicity sustainment [11, 18, 21].

At the SSPX experiment [21] it was found that once the gun current exceeded a soft threshold limit, detached flux and current channels were formed ($\mathcal{V}-\mathcal{V}_\circ\neq 0$). In this regime, oscillations ($10-100$ kHz) in gun voltage and measured poloidal magnetic field were observed. We argue that such oscillations are ubiquitous with helicity sustainment against resistive decay. In fact the SSPX experiment was able to achieve a quiescent state with higher electron temperatures T_e and consequently lower resistive decay rates by altering the bias magnetic field profile [19]. Since helicity injection was minimal during the quiescent stage, the mode activity was suppressed. However, after the quiescent stage, when the gun current started decaying, the mode activity increased.

The SPHEX experiment [18] found similar $n = 1$ oscillations at 20 kHz during the sustainment stage and no oscillations in the resistive decay stage. The sense of oscillations during the sustainment stage changed with the sign of total helicity being sustained.

Sustained spheromak configurations can be considered to be in a quasi-equilibrium with small fluctuations. A naive consideration of equation (2.4) suggests that zero mean fluctuations in magnetic vector potential cannot balance the mean loss of helicity by the resistive term on the right side. However, we now argue that this conclusion is false. Consider the case that a current $I_\circ$ flows along the open flux tube and does not leak outside the open flux tube. If so, then akin to Kirchoff's voltage law, $\int_{\mathcal{V}_\circ} \partial \mathbf{A}/\partial t \cdot \mathrm{d}\mathbf{l}$ can be expressed as a sum of voltages induced by self inductance and mutual inductance

$$\frac{\mathrm{d}K_{rel}}{\mathrm{d}t} - 2\psi_\circ \left(\frac{\partial (I_\circ L_\circ)}{\partial t} + \sum_{i=1}^{N} \frac{\partial (I_i M_i)}{\partial t} \right) = -2 \int_{\mathcal{V}-\mathcal{V}_\circ} \eta \mathbf{J} \cdot \mathbf{B} \mathrm{d}^3 r, \tag{2.5}$$

where $L_\circ$ is the self inductance of the current carrying open flux tube and M_i is the mutual inductance between the open flux tube and i^{th} closed current loop carrying a current I_i, where we have split the plasma volume into $i = 1, \ldots, N$ closed current loops. In order to inject helicity into the plasma volume electrostatically, either the self inductance of the current carrying open flux tube should change or the mutual inductance should change. Most magnetized gun driven pulsed spheromak experiments rely on an increasing self inductance $L_\circ$ to inject helicity (see section 2.1). Even sustained spheromak experiments [21] rely on increasing self inductance $L_\circ$ as a means of increasing helicity before plasma detachment.

Let us now examine a quasi equilibrium solution for equation (2.5) with fluctuating quantities-$L_\circ$, M_is and I_is. With only a fluctuating self inductance, DC helicity cannot be injected into the plasma against resistive decay as $\langle \partial (I_\circ L_\circ)/\partial t \rangle = 0$. Similarly, DC helicity cannot be injected with only fluctuating mutual inductances (M_is) and closed currents (I_is). However, a repetition of the following sequence of events can inject mean helicity through fluctuating quantities: The expansion of the open flux loop increases the self inductance $L_\circ$ thereby injecting helicity into the plasma. Meanwhile the mutual inductance or the closed currents in the plasma decay resistively. When the self inductance increases beyond a certain limit, reconnection converts open flux to closed flux. The dynamical reconnection process lowers the self inductance $L_\circ$ but increases the mutual inductance and closed currents. The cycle thus continues and mean helicity is injected by fluctuating quantities. Such a dynamo-like process is an essential requirement for sustained spheromaks. The essence of this chapter is showing that this dynamo process cannot be time independent.

2.1 Helicity Injection in Pulsed Spheromak Experiments

Pulsed spheromak experiments [13, 22] do not have closed flux tubes during the initial plasma ejection stage. For such systems, equation (2.5) can be expressed as

$$\frac{\mathrm{d}K_{rel}}{\mathrm{d}t} - 2\psi_\circ \frac{\partial (I_\circ L_\circ)}{\partial t} = 0. \tag{2.6}$$

Integrating equation (2.6) over time yields the injected helicity,

$$\Delta K_{rel} = 2\psi_\circ I_\circ L_\circ, \tag{2.7}$$

which is twice the product of the imposed bias flux $\psi_\circ$ and the flux generated by the electrode current $L_\circ I_\circ$. Thus, to comprehend the amount of helicity injected in pulsed spheromak experiments, it is paramount to understand the dynamics leading to a change in the self inductance $L_\circ$ of the open flux tubes. Chapter 5 focuses on understanding the mechanism causing the change in self inductance $L_\circ$ of the open flux tube in the Caltech spheromak experiment.

Chapter 3

Electrical Characterization of the Discharge Circuit of the Caltech Spheromak Experiment

Figure 3.1 shows the schematic of the discharge circuit of the Caltech Spheromak Experiment. It consists of two high voltage (HV) capacitors ($\sim 59\ \mu$F) each switched by a separate ignitron [23–25]. The Caltech Spheromak Experiment uses size A GL-7703 ignitrons [26]. The ignitrons are each connected to the discharge electrodes by four low inductance coaxial cables. A matched resistor ($\sim 2.3\ \Omega$) is connected across the electrodes. The purpose of the matched resistor is two-fold:

- It serves as a safety dump resistor for the capacitors in the event of a misfire.
- Its resistance matches the characteristic impedance of the cables and thus prevents reflections of the initial capacitor pulse when ignitron is switched.

This chapter describes methods for calculating the various internal resistances and inductances of the discharge circuit. These values are used to determine the temporal behavior

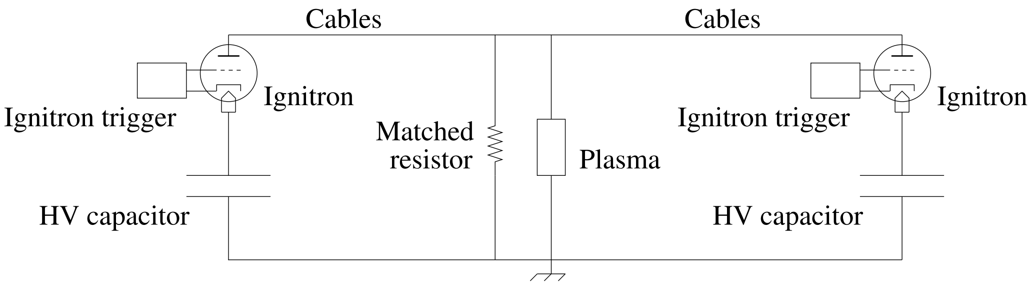

Figure 3.1: Schematic of the discharge circuit of the Caltech spheromak experiment.

of the discharge circuit and also to account for all the energy losses in the circuit. Unless otherwise mentioned, for the measurements and estimates reported in this chapter and in this thesis, only one capacitor and ignitron was used in the discharge circuit (see figure 3.1). This was done:

1. To remove jitter associated with triggering two ignitrons [27].
2. To prevent excessive currents from kinking the plasma jets studied in chapter 5.

However, as discussed in section 3.3, even with two capacitors being discharged, the characteristics of the discharge circuit were similar to that of a circuit with a single capacitor.

Section 3.1 describes various methods to calculate the plasma inductance and resistance. Section 3.2 estimates the electrical resistances and inductances of the cables and the ignitron in the discharge circuit. The results are interpreted in section 3.3 and the discharge circuit is modeled as an under-damped current source.

3.1 Plasma Parameters

3.1.1 Plasma Parameters from Traces

Figure 3.2 shows the typical voltage and current traces measured at the electrodes across the plasma. Note that the traces are almost out of phase, implying that the plasma is mostly inductive. The voltage measured across the electrodes and the current flowing through the electrodes are related by

$$\begin{aligned} V(t) &= I(t)R(t) + \frac{\mathrm{d}}{\mathrm{d}t}\left(I(t)L(t)\right) \\ &= I(t)\left(R(t) + \frac{\mathrm{d}L(t)}{\mathrm{d}t}\right) + L(t)\frac{\mathrm{d}I(t)}{\mathrm{d}t}, \end{aligned} \tag{3.1}$$

where V is the voltage measured across the electrodes, I is the current flowing through the electrodes and the plasma, L is the time-varying inductance of the plasma structure, and R is the time-varying resistance of the plasma. At the plasma breakdown (see figure 3.2) the inductance is due to the eight *"spider legs"* as shown in figure 1.7(a). As the plasma current increases and a jet is formed, the plasma inductance is due to an outward moving jet.

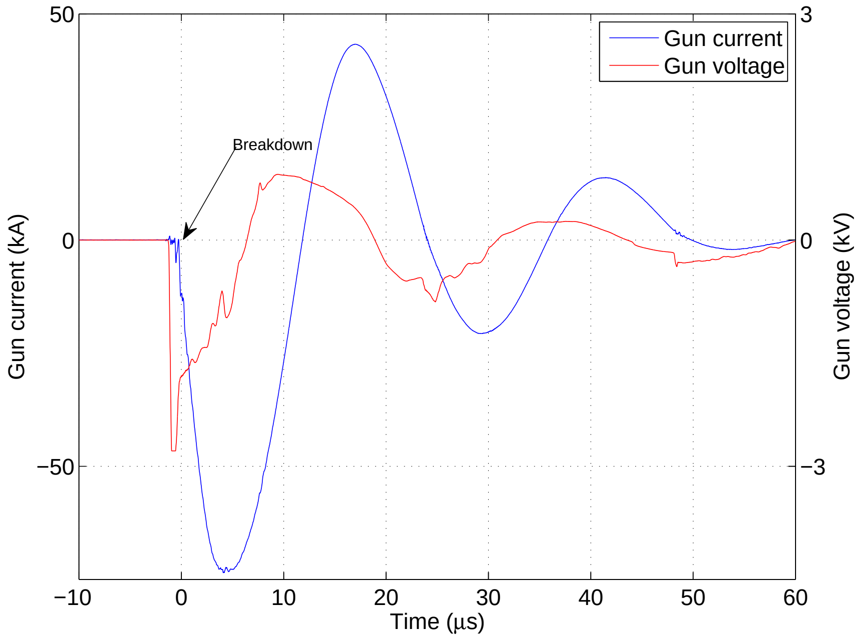

Figure 3.2: The current and voltage traces measured across the electrodes for shot #8500.

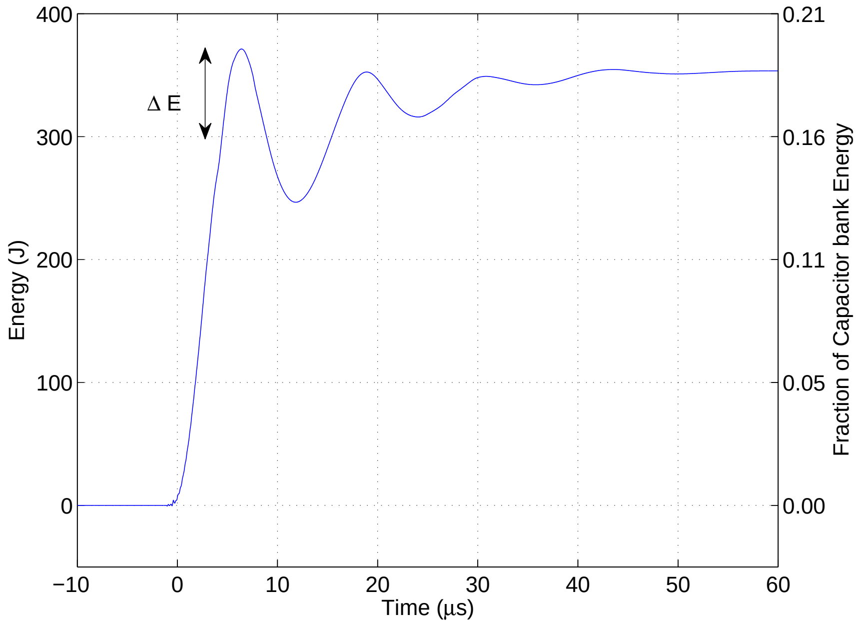

Figure 3.3: Energy ($= \int_0^t VI\mathrm{d}t$) flowing into the plasma in shot #8500. A 59 μF capacitor charged to 8 kV was discharged into a deuterium plasma. Total capacitor bank energy $= CV^2/2 \approx 1900$ J.

The following estimates of plasma impedance can be made from figures 3.2 and 3.3:

- Consider the voltage and current traces from a typical plasma discharge as shown in figure 3.2. A typical current waveform consists of approximately five half cycles. Equation (3.1) indicates that the inductance of the plasma structure can be estimated at successive zero crossings ($I \sim 0$) of the current traces by $L \sim V/\dot{I}$. Similar arguments have been used to estimate plasma inductances in other spheromak experiments [21, 28]. The plasma inductance at breakdown is estimated to be $\sim$ 50 nH. The inductance for a fully developed plasma jet will be different from this estimate. Note that the lifetime of the Caltech Spheromak is $\sim$ 10 μs, which corresponds to ramping up of the current in the first half of the cycle. Thus after the initial ramping of the current, each successive zero crossing corresponds to secondary breakdowns (or secondary spheromak formations).

- Figure 3.3 plots the energy flowing into the plasma as a function of time. The final steady state value of the energy is the total energy dissipated by the plasma by heating and radiation. The steady state value of the energy dissipated is proportional to the resistance of the plasma. However, the fluctuating part of the energy (ΔE) is the inductive energy sloshing back and forth between the plasma and the driving circuit. The inductance of the plasma jet can be estimated as $L \sim 2\Delta E/I^2$. From figure 3.3, $\Delta E \sim 70$ J when a current of $I \sim 70$ kA flows through the plasma (see figure 3.2). Thus the typical inductance of a plasma jet is $L \sim 30$ nH.

- Equation (3.1) also implies that $(R + \dot{L}) \sim V/I$ when $I(t)$ is at a local extrema. Thus, the sum of the plasma resistance and the rate of change of inductance can be estimated from figure 3.2 to be $(R+\dot{L}) \sim V/I \sim 12$ mΩ when $I(t)$ is at its minimum at $t \sim 4.3$ μs. Note that we previously estimated the plasma jet to develop an inductance of $\sim$ 30 nH in 4.3 μs, which implies $\dot{L} \sim 7$ mΩ. Thus the jet resistance R and its rate of change of inductance $\dot{L}$ are comparable to each other.

3.1.2 Plasma Parameters from Geometry

Figure 3.4 shows a simple model of the plasma jet outflow. From such a model, the plasma impedances can be estimated as shown below.

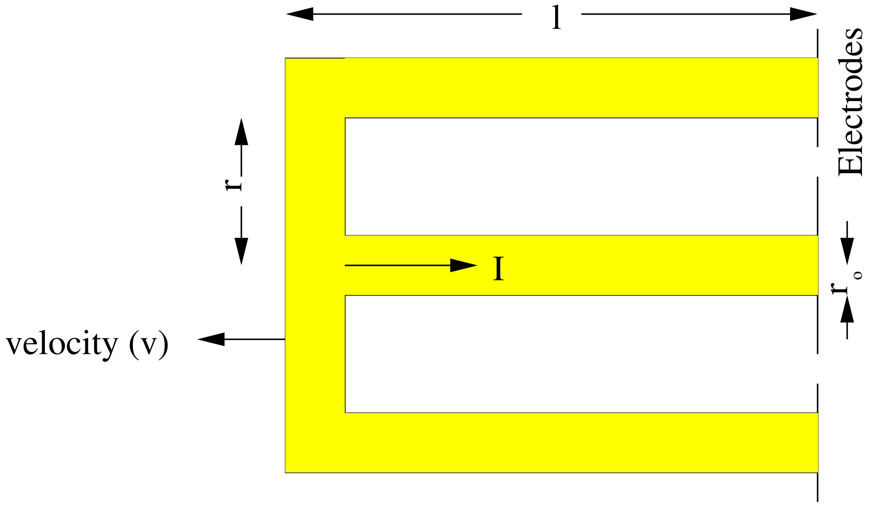

Figure 3.4: A simplistic model of plasma jet. A current I flows through a central column of radius $r_\circ$. The current returns at radius r. The length of the jet is l and it is moving outwards with velocity v.

The toroidal magnetic field for a typical plasma jet with $l \gg r_\circ$ shown in figure 3.4 is given by

$$B_\phi = \frac{\mu_\circ I}{2\pi r},$$

and is non-zero only between the inner and the outer current channels of the jet. The flux linked with the toroidal magnetic field is

$$\begin{aligned} \Phi &= \int_{r_\circ}^{r} \frac{\mu_\circ I}{2\pi r} l dr \\ &= \frac{\mu_\circ I l}{2\pi} \log(\frac{r}{r_\circ}). \end{aligned}$$

Thus the inductance is given by

$$\begin{aligned} L &= \frac{\Phi}{I} \\ &= \frac{\mu_\circ l}{2\pi} \log(\frac{r}{r_\circ}), \end{aligned} \tag{3.2}$$

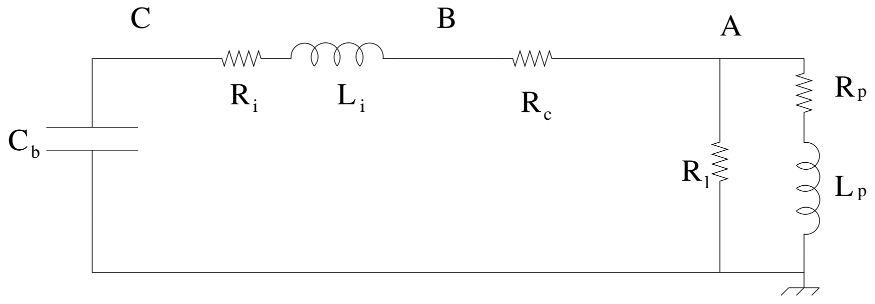

Figure 3.5: A lumped circuit model for the spheromak discharge circuit. The time dependent plasma resistance and inductance are denoted by $R_p(t)$ and $L_p(t)$ respectively. The resistor $R_l \sim 2.3\ \Omega$ is a large load resistance matched to the cable impedance. The lumped resistance of the cables is represented by R_c. The time dependent resistance and inductance of the ignitron is denoted as $R_i(t)$ and $L_i(t)$. The high voltage capacitor being discharged across the electrodes is represented by $C_b \sim 59\ \mu$F.

and the rate of change of inductance is given by

$$\dot{L} = \frac{\mu_\circ v}{2\pi} \log(\frac{r}{r_\circ}). \tag{3.3}$$

For typical D_2 plasma jets, $v \sim 30$ km/s, $l \sim 20$ cm, $r \sim 25$ cm, and $r_\circ \sim 10$ cm (see section 1.3.2). Using these values in equations (3.2) and (3.3) give, $L \sim 35$ nH and $\dot{L} \sim 5.5$ mΩ.

The plasma resistance can also be estimated by similar geometrical considerations. The plasma ion temperature T_i is $\sim$ 2 eV [17, Pg 53]. Since the plasma is extremely collisional (see section 1.3.2), the plasma electron temperature T_e should be equal to the ion temperature T_i. Assuming a Coulomb logarithm of 10 implies a Spitzer resistivity $\eta \sim 3.6 \times 10^{-4}$ Ωm. For a plasma structure shown in figure 3.4, the resistance can be estimated as $R \sim \eta l/\pi r_\circ^2 \sim 2.5$ mΩ. Due to the uncertainties involved with the Coulomb logarithm and the plasma geometry, the plasma resistance is an extremely crude estimate.

The plasma impedances estimated in this section compare well with the values calculated in section 3.1.1.

3.2 Circuit Model for Spheromak Experiment

Figure 3.5, shows the lumped circuit model for the spheromak discharge configuration. In section 3.1 we estimated $R_p(t) \sim 2.5 - 5$ mΩ and $L_p(t) \sim 30 - 50$ nH. In this section we describe how these parameters compare to the other impedances in the circuit.

To estimate the other impedances in the circuit, the following changes were made to the circuit shown in figure 3.5:

- R_l is large compared to the plasma impedance and hence was temporarily removed.
- The "plasma" was replaced by a fixed dummy load[1] of resistance 82 mΩ and inductance 1 μH.

A series of shots were done by charging the high voltage capacitor to 2 kV and discharging it across the dummy load. Voltages were measured at three different locations in the circuit:

- Voltage was measured at location A (see figure 3.5). The energy flowing into the dummy load is given by $E_{\text{load}} = \int V_A I \, \mathrm{d}t$.
- Voltage was measured at location B (see figure 3.5). The energy flowing into the dummy load and the cables is given by $E_{\text{cable+load}} = \int V_B I \, \mathrm{d}t$.
- Voltage was measured at location C (see figure 3.5). The energy flowing into the dummy load and the cables is given by $E_{\text{cable+load+ignitron}} = \int V_C I \, \mathrm{d}t$. Also, the voltage across the ignitron is $V_{\text{ignitron}} = V_B - V_C$.

Typical traces from the shots are shown in figure 3.6. The following parameters can be estimated from these traces:

- R_c*: Resistance of the cables.* The total energy dissipated across the cable and the load (see figure 3.6(c)) is $\int_0^\infty I^2(R_c + R_p)\mathrm{d}t$. Since the energy dissipated across the load is $\int_0^\infty I^2 R_p \mathrm{d}t$, we get $R_c = R_p \frac{E_{\text{cable+load}} - E_{\text{load}}}{E_{\text{load}}}$. Thus $R_c \sim 8$ mΩ.
- R_i*: Resistance of the ignitron.* The ignitron resistance is expected to be time and load dependent, but an average value can be estimated by a method similar to the

---

[1] The dummy load was built by Auna Moser.

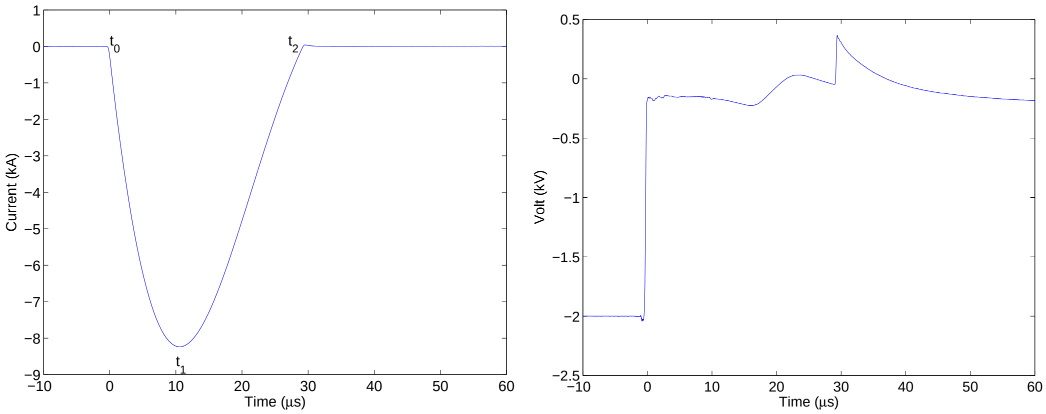

(a) Current flowing through the circuit. Average of shots #8510 and #8513

(b) Voltage across the ignitron.

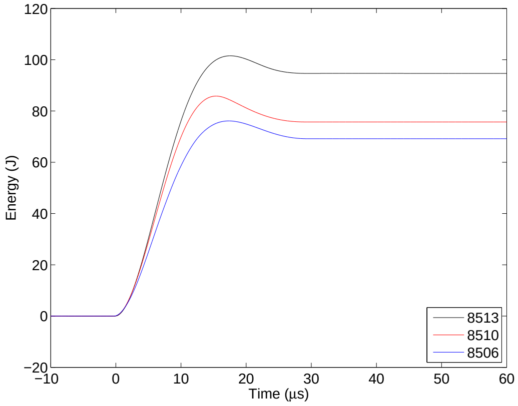

(c) Energy $E = \int_0^t V\,I\,\mathrm{d}t$ flowing into the dummy load (point A in figure 3.5; blue), into the dummy load and cables (point B in figure 3.5; red), and into the dummy load, cables and ignitron (point C in figure 3.5; black)

Figure 3.6: Measurements from discharging the high voltage capacitor charged to 2 kV across the dummy load.

method described for estimating R_c above. $R_i \sim R_p \frac{E_{\text{cable+load+ignitron}} - E_{\text{load}}}{E_{\text{load}}} - R_c$. It leads to a nominal estimate of $R_i \sim 22$ mΩ.

The ignitron resistance may also be estimated by $R_i \sim \frac{V_{\text{ignitron}}}{I_{\text{ignitron}}}$ evaluated at time t_1 from figures 3.6(a) and 3.6(b). This leads to an estimate $R_i \sim 21$ mΩ.

- L_i: *Inductance of the ignitron.* The ignitron inductance depends on the current flowing through it. An average value of the ignitron inductance can be estimated by $L_i = \frac{V_{\text{ignitron}}}{\dot{I}_{\text{ignitron}}}$, when $I_{\text{ignitron}} \sim 0$. From figure 3.6(a) $L_i \sim 170$ nH at time t_0. Similar estimates for L_i were found by discharging slightly larger currents through the dummy load. During normal operation of the spheromak experiment, there is almost a 10 fold increase in the current through the ignitron. Thus, it is plausible that the inductance of the ignitron may be slightly higher during normal operation because of the pinching effect associated with higher currents. Also, from figure 3.6(a), $L_i \sim 800$ nH at the turnoff time t_2.

3.3 Results and Interpretation

Table 3.1 summarizes the main estimates from this chapter. Note that L_p, R_p and $\dot{L}_p$ were estimated for deuterium jets. L_p and $\dot{L}_p$ may be lower for heavier gases, but as described later in this section, this will not change the characteristics of the discharge circuit. The following conclusions can be drawn from these estimates:

1. Low energy coupling efficiency: During a plasma discharge only $R_p/(R_p + R_c + R_i) \sim 15\%$ of the initial capacitor energy is dissipated into the plasma. This estimate is in agreement with figure 3.3. It should be noted, however, that the energy fraction being coupled into the plasma increases with an increase in plasma resistance or decrease in ignitron resistance. Typically, it is observed that even with varying parameters not more than $35\% - 40\%$ of the energy is coupled to the plasma at the Caltech spheromak experiment. The high resistance of the ignitron makes it a very inefficient technology to couple power into the plasma. This was observed in other experiments as well [29].

2. Under-damped discharge circuit: For the typical parameters shown in Table 3.1, the discharge circuit is under-damped [30, Chapter 9.6]. In an under-damped circuit the

Table 3.1: Typical parameters of the discharge circuit of the Caltech spheromak experiment.

Parameter	Approximate estimate	Reference
C_b capacitance of bank	59 μF	N/A
${\omega_d}^a$ damped frequency of discharge	2.7×10^5 rad/sec	Figure 3.2
R_p plasma resistance	5 mΩ (measured), 2.5 mΩ (Spitzer)	Section 3.1
L_p plasma inductance	30 nH (typical), 50 nH (at breakdown)	Section 3.1
$\omega_d L_p$ plasma inductive impedance	$8 - 13$ mΩ	N/A
$\dot{L}_p$ rate of change of plasma inductance	$6 - 7$ mΩ	Section 3.1
R_c cable resistance	8 mΩ	Section 3.2
R_i ignitron resistance	$21 - 22$ mΩ	Section 3.2
L_i ignitron inductance	170 nH (typical), 800 nH (at ignitron turnoff)	Section 3.2
$\omega_d L_i$ ignitron inductive impedance	45 mΩ (typical), 210 mΩ (at ignitron turnoff)	N/A

---

[a] $\omega_d = \pi/\tau$, where τ is the first zero crossing time in the current waveform.

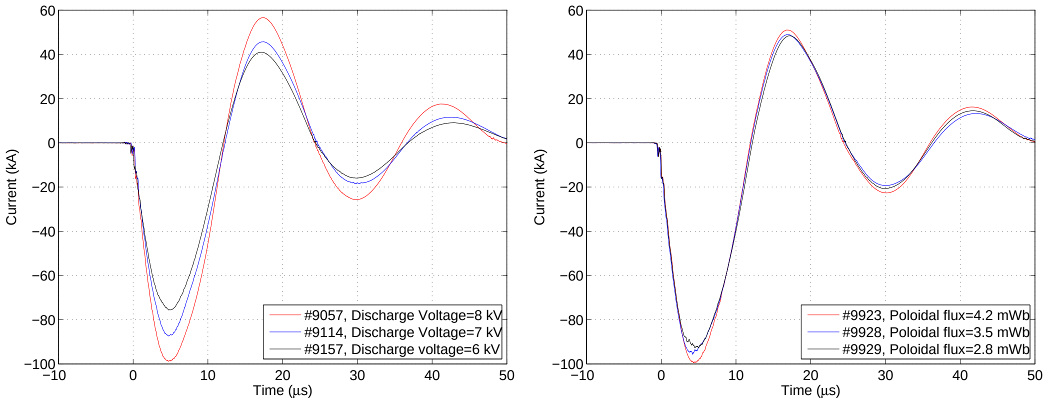

(a) Current traces from Hydrogen plasma shots with varying discharge voltages.

(b) Current traces from Hydrogen plasma shots with varying stuffing flux.

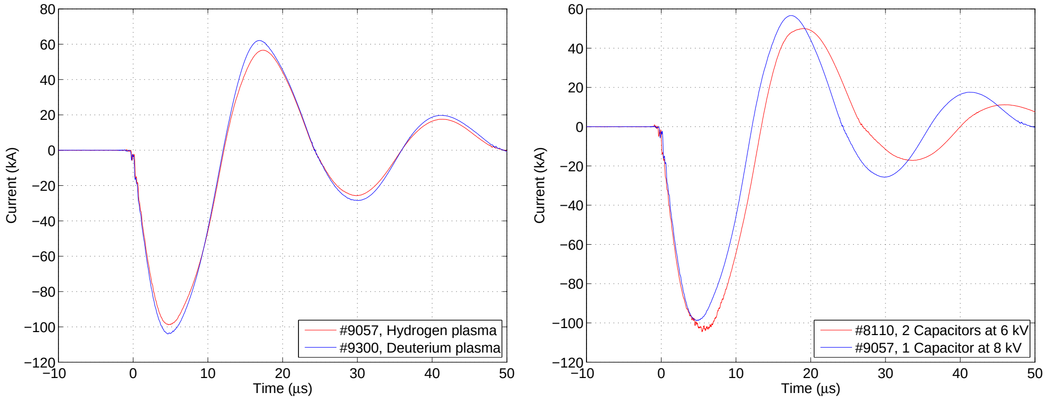

(c) Current traces from Hydrogen and Deuterium plasma shots.

(d) Current traces from Hydrogen plasma shots with one and two capacitors in the discharge circuit.

Figure 3.7: Current trace from various plasma shots. Figures 3.7(a), 3.7(b) and 3.7(c) traces show that even with varying plasma parameters, the temporal behavior of the discharge current trace changes insignificantly, thus confirming that the discharge circuit acts as a current source. Figure 3.7(d) shows that, even with two capacitors being discharged across the plasma, the circuit was under-damped with similar temporal behavior. This is because even though the capacitance in the circuit increased two-fold, the resistance and the inductance also increased almost two-fold due to the extra ignitron.

current trace oscillates and reverses sign. The frequency of these damped oscillations, ω_d, is given by $\omega_d = \sqrt{|\left(\frac{R}{2L}\right)^2 - \frac{1}{LC}|}$. Plugging in nominal values of $C = 59$ μF, $L = 200$ nH, and $R = 30$ mΩ, we get $\omega_d = 2.8 \times 10^5$ rad/sec, which is very close to the measured frequency mentioned in Table 3.1.

3. Discharge circuit is a current source: Table 3.1 shows that the combined impedance of the ignitron and the cables dominates the impedance of the plasma. Thus the plasma impedance plays a negligible role in determining the profile of the current trace in the circuit. It is observed that even when the parameters of plasma formation are varied, the frequency of damped oscillations remains close to 2.7×10^5 rad/sec (see figure 3.7). Thus, the Caltech spheromak discharge circuit can be modeled as a current source driving an inductive plasma load.

4. Ignitron cannot be used as a crowbar device: For many inductive loads, a crowbar device is placed across the inductive load to recycle the current through the load [31]. Switching devices like solid state diodes or ignitrons are used as crowbars to mantain a high uni-directional current through the load and thus prevent high reverse voltage on the main capacitors. However, an ignitron cannot be used as a crowbar for the Caltech spheromak experiment as the ignitron impedance is much greater than the plasma impedance. Previous attempts to use the ignitron as a crowbar device for the Caltech spheromak experiment have been unsuccessful.

The energy efficiency and other electrical characteristics of the Caltech Spheromak Experiment are close to parameters of other pulsed plasma experiments [32]. For pulsed experiments using spark gap switches instead of ignitrons, much higher energy coupling efficiencies ($\sim 90\%$) have been reported [33]. This is because spark gaps have a much lower resistance (~ 1 mΩ).

3.4 Ignitron Characterization

This section discusses a couple of characteristics of the ignitron GL-7703 [26] used in the Caltech spheromak experiment.

1. The GL-7703 is a commercially available low inductance ignitron. The product data

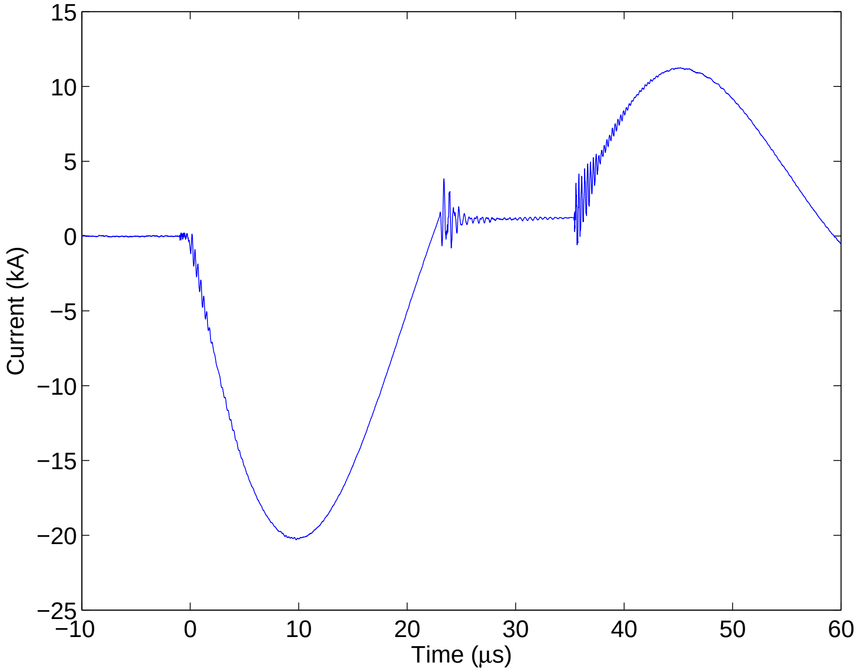

Figure 3.8: The current trace measured across the electrodes for shot #8553 when the HV capacitor was discharged across a dummy load. The ignitron stopped conducting briefly.

sheet [26] lists its approximate inductance to be 20 nH. However, our analysis estimates the inductance to be 170 − 800 nH. The inductance of the ignitron depends on the return path of the current outside the ignitron, but 20 nH is still an ultra optimistic estimate.

2. The GL-7703 can remain conducting even if the current reverses across its terminals. If the current does not reverse fast enough, the ignitron may turn off, as seen in figure 3.8. The ignitron turn off may depend on factors like external temperature, peak current flowing through the ignitron, and the reverse voltage across the ignitron as the current approaches zero [24]. One of the most important factors determining ignitron turn off is $\dot{I}$, the rate of current change as $I \sim 0$. Figure 3.8 may be used to estimate a nominal rate of current change $\dot{I} = 2$ kA/μs required to prevent the ignitron from turning off.[2] However, a much lower cut off limit of $\dot{I} \sim 5$ A/μs is often cited for larger, high inductance ignitrons [24].

---

[2] Note that the plasma experiments operated at much higher currents (> 60 kA), and so did not experience ignitron turn off.

Chapter 4

Interferometer for the Caltech Spheromak Experiment

Laser interferometry is an extensively used diagnostic for plasma experiments. Existing plasma interferometers [34–39] are designed on the presumption that the scene and reference beam path lengths have to be equal, a requirement that is costly in both the number of optical components and the alignment complexity. It is shown in this chapter that having equal path lengths is not necessary - instead what is required is that the path length difference be an even multiple of the laser cavity length. This fact was used in the design of a homodyne and a heterodyne laser interferometer for the Caltech spheromak experiment. These interferometers measured typical line-average densities of $\sim 10^{21}/\mathrm{m}^2$ with an error of $\sim 10^{19}/\mathrm{m}^2$.

The homodyne interferometer was the first interferometer developed for the Caltech spheromak experiment. It was later replaced by the heterodyne interferometer because of specific advantages describes in Section 4.5.6. However, the uniqueness of both the interferometers was that they operated at a large path length difference between the scene and the reference beams - a feature which is often not utilized on existing interferometers.

This chapter is organized as follows. Section 4.1 describes the relation between the density of the plasma and the induced phase change of an electromagnetic wave travelling through it. Section 4.2 describes the design criteria for the interferometers. Section 4.3 shows that the laser phase auto-correlation function, a measure of the coherence, is a quasi-periodic function of the path length difference between the two beams of an interferometer. Sections 4.4 and 4.5 describe the homodyne and heterodyne interferometers built for the

Caltech spheromak experiment. The alignment procedure for both the interferometers is described in Appendix A.

4.1 Electromagnetic Wave Dispersion Relation in a Plasma

The dispersion relation of an electromagnetic wave travelling through the plasma is[7, Chapter 4]

$$\omega^2 = \omega_{pe}^2 + k^2c^2,$$

where the electron plasma frequency, ω_{pe}, is given by

$$\omega_{pe}^2 = \frac{n_e e^2}{\epsilon_\circ m_e}.$$

If $\omega \gg \omega_{pe}$, then the wavenumber k can be approximated as

$$\begin{aligned} k &= \frac{\omega}{c}\left(1 - \frac{\omega_{pe}^2}{\omega^2}\right)^{\frac{1}{2}} \\ &\approx \frac{\omega}{c}\left(1 - \frac{\omega_{pe}^2}{2\omega^2}\right). \end{aligned}$$

Using the above relation, the phase shift in a beam traversing a length L through the plasma is given by

$$\begin{aligned} \phi_p &= \int_0^L k\,dx \\ &\approx \frac{\omega}{c}\int_0^L \left(1 - \frac{\omega_{pe}^2}{2\omega^2}\right) dx. \end{aligned}$$

The first term in the above integral is the phase shift experienced by a beam travelling through vacuum. Thus the change in the phase shift caused by the plasma (second term) is

$$\begin{aligned} \Delta\phi_p &= \frac{e^2\lambda}{4\pi c^2 \epsilon_\circ m_e}\int_0^L n(x)dx \\ &= 2.8 \times 10^{-15}\lambda \int_0^L n(x)dx, \end{aligned} \tag{4.1}$$

where the wavelength λ and the length L are expressed in m, and the density $n(x)$ in m^{-3}. Equation (4.1) can be used to calculate the line average plasma density from the measured phase shift

$$\bar{n}(x) = \frac{\Delta\phi_p}{2.8 \times 10^{-15}\lambda L}.$$

4.2 Design Considerations for the Interferometer for the Caltech Spheromak Experiment

As discussed in Section 1.3.2, the plasma density in the jets produced by the Caltech Spheromak Experiment is $n \sim 10^{22}$ m^{-3}. This corresponds to an electron plasma frequency of $\omega_{pe} \sim 5 \times 10^{12}$ rad/sec. The frequency of operation of a He-Ne laser is $\omega \sim 3 \times 10^{15}$ rad/s, so the condition $\omega \gg \omega_{pe}$ is satisfied. The laser beam passes through a typical length of $L \sim 0.1$ m of plasma. This will result in an expected phase shift caused by the plasma on the order of $\Delta\phi_p \sim 2$ rad, which is of the order of a fringe shift and should be measurable by the interferometer.

The interferometer for the Caltech Spheromak Experiment was designed as per the following considerations:

- Due to space limitations and safety considerations, the interferometer could not be placed close to the vacuum chamber.

- The large diameter of the vacuum chamber (~ 1.5 m) ensured that the scene beam had a long path length. The mirrors placed at the bottom and top of the chambers have limited access, so aligning an interferometer in Mach Zehnder geometry for such a setup would have been very costly and cumbersome. Thus the interferometer was set up in a double pass geometry with a layout similar to that of a Michelson interferometer (for the homodyne interferometer refer to section 4.4.2) or a hybrid of the Michelson and Mach-Zehnder interferometer (for the heterodyne interferometer refer to section 4.5.2).

- Many interferometers used on existing plasma experiments are two-color interferometers [34–40] that decouple the phase shift caused by the plasma and by mechanical vibrations. Because mechanical vibrations (kHz range) are unimportant for the fast timescale ($\sim 10\ \mu$s) of the Caltech plasma experiments, a single laser interferometer is adequate. As discussed in sections 4.4.3 and 4.5.3, the effects of the vibrations can be removed by low-pass filtering the detected phase. In fact, these vibrations were used to "self"-calibrate the homodyne interferometer (refer section 4.4.3).

- Refractive bending of light may cause a spurious change in signal intensity that can be incorrectly interpreted as a change in phase shift caused by the plasma. Interferometers for large plasma experiments have often used extra optics to counter refractive bending caused by plasma [38, 41, 42]. However, at the Caltech spheromak experiment, refractive bending is not a concern as:
    1. the spatial extent of the plasma is small.
    2. the plasma is approximately azimuthically symmetric. Thus, the proposed path of the beam will always be in the direction of ∇n_e, the beam will not bend.

4.3 Laser Phase Auto-correlation Function

4.3.1 Frequency Spectrum of the Laser

A gas laser contains an active medium within a resonating optical cavity bounded by mirrors on either end. The mirrors allow only those optical modes which traverse an integer number of half-wavelengths within the cavity. The frequencies of these optical modes are

$$\nu_q = q\frac{c}{2d} \qquad q = 0, 1, 2\ldots, \tag{4.2}$$

where c is the speed of light and d is the distance between the cavity mirrors. These discrete frequencies are separated by $\nu_M = c/2d$. For a typical He-Ne gas laser with a cavity length of $d \sim 25$ cm, the modes are separated by $\nu_M \sim 600$ MHz.

The active medium between the mirrors can be considered as a narrow-band optical amplifier. The gain curve for this amplifier is centered around the frequency $\nu_\circ$, such that $h\nu_\circ$ is the energy released by the atomic transition that emits the photon. Only a few of the discrete frequencies given by equation (4.2) appear in the laser beam. These are the amplified modes; the others are attenuated by the medium. For example, in a commercial

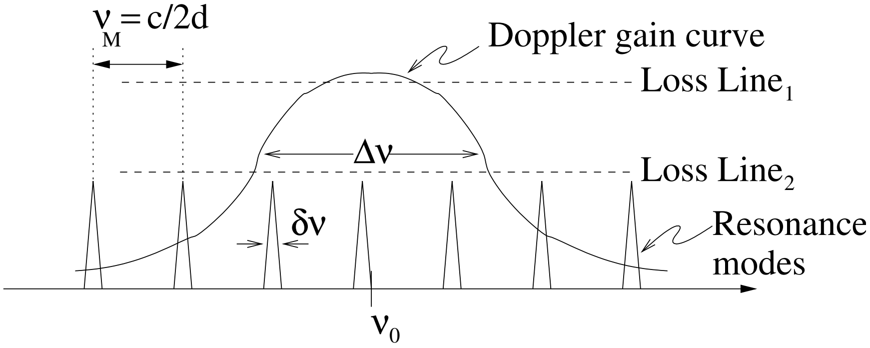

Figure 4.1: Power spectrum of a laser showing discrete frequency resonance modes. Also plotted are the Doppler gain curve and two possible levels of cavity loss.

red He-Ne laser, photons are emitted because of transition of Ne atoms from a $2p^5 5s$ state to $2p^5 3p$ state, which corresponds to a center frequency of $\nu_\circ \sim 473$ THz. The gain curve is primarily Doppler broadened [43] by an amount

$$\Delta\nu \sim \frac{\nu_\circ}{c}\sqrt{\frac{2kT}{M}},$$

where k is Boltzmann's constant, T is the gas temperature and M is the molecular mass of the radiating atom. For a collection of Ne atoms emitting light at the He-Ne wavelength of $\lambda_\circ = 632.8$ nm at room temperature, the Doppler width is ~ 2 GHz. Thus, an amplifier with gain width $\Delta\nu \sim 2$ GHz allows about 4 modes separated by $\nu_M \sim 600$ MHz, as sketched in figure 4.1 [44].

Power will build up from noise in modes for which the gain exceeds the losses. As the power in modes builds up, modes will saturate and equilibrate, so that the gain balances the losses. Modes for which the losses exceed the gain are severely attenuated. For example, if loss-line 1 in figure 4.1 represents the losses in the system, a monochromatic wave will exist, corresponding to the resonance mode closest to the peak of the amplifier gain function. On the other hand, if the losses are represented by loss line 2, there will be 3 distinct modes in the wave. Power in various modes is distributed according to the amplifier gain profile and losses in the system [45].

The wave's electric field in the polarization direction for an ideal laser can be represented as:

$$\begin{aligned} E(t) &= \frac{1}{2\pi}\sum_q \tilde{E}_q e^{\mathrm{i}\omega_q t} \\ &= \frac{1}{2\pi}\int_{-\infty}^{\infty}\sum_q \tilde{E}_q \delta(\omega-\omega_q)e^{\mathrm{i}\omega t}\mathrm{d}\omega, \end{aligned} \tag{4.3a}$$

where $\omega_q = 2\pi\nu_q$. Functions and variables in the frequency domain will be represented by a "tilde." Equation (4.3a) is just a Fourier transform relation. Thus the Fourier transform of the electric field for an ideal laser is a series of delta functions, with the non-zero Fourier coefficients $\tilde{E}_q$ corresponding to the non-attenuated modes.

The discrete resonant frequency modes of a laser are each broadened by a small amount $\delta\nu$, due to:

1. losses due to absorption and scattering within the medium [43]. These losses relate to the finite photon decay time via the uncertainty relation between time and frequency.
2. imperfect reflection at the mirrors [43].
3. vibration of mirrors [46]. If the mirrors vibrate by an amount δd, the corresponding broadening of the modes is given by, $\delta\nu \sim \nu_\circ \delta d/d$.

In most commercial lasers, the frequency broadening thus produced is of the order of $\delta\nu \sim 1$ MHz, as sketched in figure 4.1. Typically, $\delta\nu \ll \nu_M$, so the frequency broadened modes do not overlap each other.

The Fourier transform of the electric field will now consist of a series of broadened functions. Under the simplifying assumption that all the modes are broadened by the same amount, the electric field Fourier transform can be represented as

$$\tilde{E}(\omega) = \sum_q \tilde{E}_q \tilde{F}(\omega-\omega_q),$$

where $\tilde{F}(\omega)$ is a low-pass broadening function of width $2\pi\delta\nu$. Because the modes are well separated, the spectral power is

$$|\tilde{E}(\omega)|^2 = \sum_q |\tilde{E}_q|^2 |\tilde{F}(\omega-\omega_q)|^2. \tag{4.4}$$

4.3.2 Phase Auto-correlation Function Related to Power Spectrum

The auto-correlation function of a laser is defined as

$$G(\tau) = \frac{\langle E^*(t)E(t+\tau)\rangle}{\langle |E(t)|^2\rangle}, \tag{4.5}$$

where $\langle\cdot\rangle$ denotes time average. The coherence time of a laser is defined as the time τ at which the auto-correlation function $G(\tau)$ falls significantly below 1, and the coherence length of a laser is the coherence time scaled by c. It is traditionally assumed that if an interferometer is set up with a path length difference greater than the coherence length, the phases of the two waves will be uncorrelated, so no interference pattern will be observed. However, this standard concept of coherence length is misleading because the phase auto-correlation function is an almost periodic function; for the purpose of interferometry, it is sufficient to maintain a path length difference corresponding to a maximum of the auto-correlation function.

Using

$$E(t) = \frac{1}{2\pi}\int\limits_{-\infty}^{\infty} \tilde{E}(\omega)e^{\mathrm{i}\omega t}\mathrm{d}\omega,$$

equation (4.5) can be expressed as

$$G(\tau) = \frac{\int\limits_{-\infty}^{\infty}\int\limits_{-\infty}^{\infty} \mathrm{d}\omega\, \mathrm{d}\omega' \tilde{E}^*(\omega)\tilde{E}(\omega')e^{\mathrm{i}\omega'\tau}\langle e^{\mathrm{i}(\omega'-\omega)t}\rangle}{\int\limits_{-\infty}^{\infty}\int\limits_{-\infty}^{\infty} \mathrm{d}\omega\, \mathrm{d}\omega' \tilde{E}^*(\omega)\tilde{E}(\omega')\langle e^{\mathrm{i}(\omega'-\omega)t}\rangle}. \tag{4.6}$$

Using the relation

$$\langle e^{\mathrm{i}(\omega'-\omega)t}\rangle \sim \int\limits_{-\infty}^{\infty} e^{\mathrm{i}(\omega'-\omega)t}\mathrm{d}t \sim \delta(\omega'-\omega),$$

equation (4.6) reduces to

$$G(\tau) = \frac{\int\limits_{-\infty}^{\infty} \mathrm{d}\omega |\tilde{E}(\omega)|^2 e^{\mathrm{i}\omega\tau}}{\int\limits_{-\infty}^{\infty} \mathrm{d}\omega |\tilde{E}(\omega)|^2}, \tag{4.7}$$

so

$$G(\tau) = \frac{1}{2\pi} \int_{-\infty}^{\infty} \tilde{S}(\omega) e^{\mathrm{i}\omega\tau} \mathrm{d}\omega, \tag{4.8}$$

where $\tilde{S}(\omega)$ is the normalized spectral power defined by

$$\tilde{S}(\omega) = \frac{2\pi |\tilde{E}(\omega)|^2}{\int\limits_{-\infty}^{\infty} \mathrm{d}\omega |\tilde{E}(\omega)|^2}.$$

Equation (4.8) is the Wiener-Khinchin theorem [43] and shows that the auto-correlation function and the normalized spectral power are Fourier transform pairs.

Using equation (4.4), the auto-correlation function has the dependence

$$G(\tau) \sim \int_{-\infty}^{\infty} \mathrm{d}\omega \sum_q |\tilde{E}_q|^2 |\tilde{F}(\omega - \omega_q)|^2 e^{\mathrm{i}\omega\tau}. \tag{4.9}$$

Let

$$\tilde{\mathcal{F}}(\omega) = |\tilde{F}(\omega)|^2,$$

and let $\mathcal{F}(\tau)$ be the Fourier inverse of $\tilde{\mathcal{F}}(\omega)$ so

$$\tilde{\mathcal{F}}(\omega) = \int_{-\infty}^{\infty} \mathcal{F}(\tau) e^{-\mathrm{i}\omega\tau} \mathrm{d}\tau.$$

Since $\tilde{\mathcal{F}}(\omega)$ has a spread of $\sim 2\pi\delta\nu$, $\mathcal{F}(\tau)$ will have a spread of $\sim 1/\delta\nu$.

From equation (4.9),

$$\begin{aligned}
G(\tau) &\sim \int_{-\infty}^{\infty} \mathrm{d}\omega \sum_q |\tilde{E}_q|^2 \left(\int_{-\infty}^{\infty} \mathcal{F}(\tau') e^{-\mathrm{i}(\omega-\omega_q)\tau'} \mathrm{d}\tau' \right) e^{\mathrm{i}\omega\tau} \\
&= \int_{-\infty}^{\infty} \mathrm{d}\tau' \sum_q |\tilde{E}_q|^2 e^{+\mathrm{i}\omega_q\tau'} \mathcal{F}(\tau') \left(\int_{-\infty}^{\infty} e^{-\mathrm{i}\omega(\tau'-\tau)} \mathrm{d}\omega \right) \\
&\sim \int_{-\infty}^{\infty} \mathrm{d}\tau' \sum_q |\tilde{E}_q|^2 e^{\mathrm{i}\omega_q\tau'} \mathcal{F}(\tau') \delta(\tau'-\tau) \\
&= \sum_q |\tilde{E}_q|^2 e^{\mathrm{i}\omega_q\tau} \mathcal{F}(\tau) \\
&= \mathcal{P}(\tau)\mathcal{F}(\tau),
\end{aligned}$$

where

$$\begin{aligned}
\mathcal{P}(\tau) &= \sum_q |\tilde{E}_q|^2 e^{\mathrm{i}\omega_q\tau} \\
&= \sum_q |\tilde{E}_q|^2 e^{\mathrm{i}2\pi q\nu_M\tau}. \qquad (4.10)
\end{aligned}$$

Each of the complex exponentials in equation (4.10) is periodic in τ, with a period of $\frac{1}{\nu_M}$. Thus, $\mathcal{P}(\tau)$ is also periodic with the same period. For $\tau = 0, \frac{1}{\nu_M}, \frac{2}{\nu_M}, \frac{3}{\nu_M}, \cdots$, all the components add up constructively and so $\mathcal{P}(\tau)$ will be maximum at these values of τ. The exact shape of $\mathcal{P}(\tau)$ will depend on the value of the coefficients $|\tilde{E}_q|^2$. For a laser with a large number of modes (corresponding to many non-zero $|\tilde{E}_q|^2$'s), $\mathcal{P}(\tau)$ may have a steep decay away from its peaks.

For a typical laser with $d \sim 25$ cm and $\delta\nu \sim 1$ MHz, $\mathcal{P}(\tau)$ will be periodic with period 1.67 ns and $\mathcal{F}(\tau)$ will have a spread of 1 μs. It is convenient to scale time with c to express $\mathcal{P}$, $\mathcal{F}$ and G as functions of length. $\mathcal{P}(\delta L)$ is thus periodic with period $2d = 0.5$ m and $\mathcal{F}(\delta L)$ decreases with a 300 m scale length. $G(\delta L)$ is thus the product of a slowly decaying envelope function $\mathcal{F}(\delta L)$ and a periodic function $\mathcal{P}(\delta L)$. The interferometer at Caltech operates at $\delta L \sim 8$ m, corresponding to the 16^{th} maximum of $\mathcal{P}(\delta L)$. We assume $\mathcal{F}(\delta L)$ to be Gaussian $\sim e^{-(\delta L)^2/2l^2}$, where l, the width of $\mathcal{F}$, is approximately 300 m. If an interferometer is operated at a path length difference corresponding to a maximum of $\mathcal{P}(\delta L)$, the strength

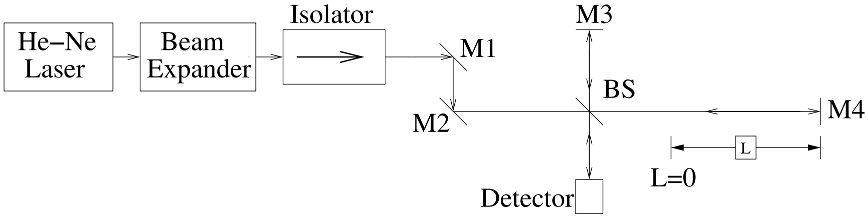

Figure 4.2: Michelson setup to measure phase auto correlation of laser. BS stands for beam splitter and M for mirror.

of interference signal will be proportional to $\mathcal{F}(\delta L)$. Thus for the Caltech interferometer, operating at a path length difference of 8 m causes attenuation of the signal amplitude by a factor $\mathcal{F}(\delta l = 8 \text{ m}) = 0.9996$. In other words, only 0.04% of power is lost due to unequal path length effects, and phase coherence is maintained since $\mathcal{P}(\delta l)$ has the same value at 8 m as at 0 m.

4.3.3 Measurement of Laser Phase Auto-correlation Function

To test if the laser being used in the Caltech interferometer indeed has a periodic auto-correlation function, the laser was used in the Michelson interferometer setup shown in figure 4.2. Mirror M4's location, L, was varied with a linear translation stage at a constant speed and the amplitude of the interference signal was plotted as a function of time, as shown in figure 4.3. Interference is caused by ambient noise vibrating the mirrors. At $t = 0$ s, L was 0, and thus the path lengths were approximately equal. The amplitude of the interference signal is directly proportional to the phase auto-correlation function. Since L was increased at a constant rate, the horizontal time axis in figure 4.3 is proportional to path length difference $2L$. As seen from figure 4.3, the phase auto-correlation function is periodic. The difference between successive maxima corresponded to $2L \sim 50$ cm. The amplitude decreased significantly beyond the third maximum because the interferometer became misaligned with large motions of the mirror. Thus a significant decrease in contrast ratio of the maximum and minimum of signal amplitude was observed beyond the third maximum. However, this was an effect of misalignment and not path length difference. The contrast ratio could be recovered by realigning the interferometer. The minima of the amplitude of the interference signal were of the order of the noise level of the detector.

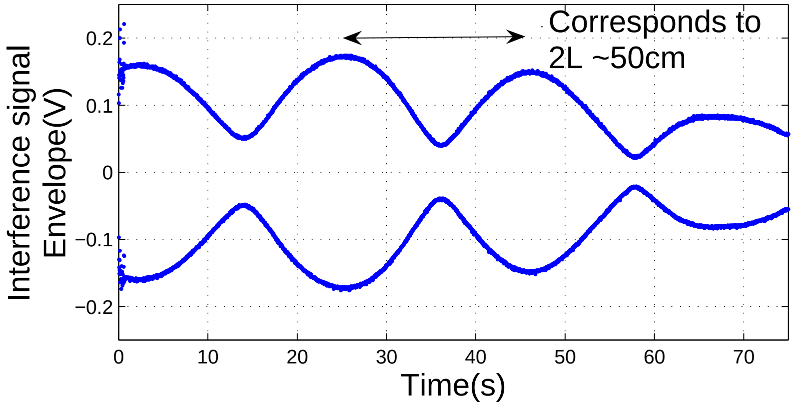

Figure 4.3: Envelope of the interference signal measured using the setup shown in figure 4.2. The path length difference $2L$ was varied at a constant rate. The envelope magnitude is directly proportional to the phase auto-correlation function.

4.4 Homodyne Interferometer

4.4.1 Theory

Quadrature phase information is generated in a homodyne interferometer by interfering a linearly polarized scene beam and a circularly polarized reference beam [41]. Consider a local coordinate system with the z-axis pointing towards the direction of the beam propagation and the y-axis pointing upwards from the optical table. The electric field for the linearly polarized scene beam is given by

$$\mathbf{E}_s = E_{0s}(\hat{\mathbf{x}} \cos\theta + \hat{\mathbf{y}} \sin\theta) \cos(kL_s - \Delta\phi_p - \omega t),$$

where θ is the polarization angle with respect to the x-axis, k is the vacuum wavenumber of the laser beam, L_s is the length of the scene beam, $\Delta\phi_p$ is the phase change caused by the plasma and ω is the lasing frequency. The electric field for the circularly polarized reference beam is given by

$$\mathbf{E}_r = E_{0r}(\hat{\mathbf{x}} \cos(kL_r - \omega t) + \hat{\mathbf{y}} \sin(kL_r - \omega t)),$$

where L_r is the length of the reference beam. As shown in section 4.4.2, a Wollaston prism is used to separately combine the $\hat{\mathbf{x}}$ and $\hat{\mathbf{y}}$ polarizations of the scene and reference beams. Output power of the detector receiving the $\hat{\mathbf{x}}$ components of the beams is

$$\begin{aligned}
S_x &\propto \langle (E_{rx} + E_{sx})^2 \rangle \\
&\propto \langle (E_{0r}\cos(kL_r - \omega t) + E_{0s}\cos\theta\cos(kL_s - \Delta\phi_p - \omega t))^2 \rangle \\
&\propto E_{0r}^2 \langle \cos^2(kL_r - \omega t)\rangle + E_{0s}^2 \cos^2\theta \langle \cos^2(kL_s - \Delta\phi_p - \omega t)\rangle \\
&\quad +2E_{0r}E_{0s}\cos\theta \langle \cos(kL_r - \omega t)\cos(kL_s - \Delta\phi_p - \omega t)\rangle \\
&\propto \frac{E_{0r}^2 + E_{0s}^2\cos^2\theta}{2} + E_{0r}E_{0s}\cos\theta\langle\cos(k\delta L - \Delta\phi_p)\rangle \\
&\quad +E_{0r}E_{0s}\langle\cos(k(L_s + L_r) - \Delta\phi_p - 2\omega t)\rangle \\
\tilde{S}_x &\propto E_{0r}E_{0s}\cos\theta\cos(k\delta L - \Delta\phi_p),
\end{aligned}$$

where $\delta L = L_s - L_r$ is the path length difference between the scene and the reference beams and $\tilde{S}_x$ is the AC component of the detector output power S_x. Similarly, the output of the detector receiving the $\hat{\mathbf{y}}$ component of the beams is given by

$$\tilde{S}_y \propto E_{0r}E_{0s}\sin\theta\cos(k\delta L - \Delta\phi_p).$$

Thus, the AC output of the detectors is proportional to the sine and cosine of the phase shift due to the plasma:

$$\begin{aligned}
\tilde{S}_x &= \alpha\cos(\Delta\phi_p - k\delta L), \\
\tilde{S}_y &= \beta\sin(\Delta\phi_p - k\delta L), \qquad (4.11)
\end{aligned}$$

and the phase can be reconstructed as

$$\Delta\phi_p = \tan^{-1}\left(\frac{\alpha}{\beta} \times \frac{\tilde{S}_y}{\tilde{S}_x}\right) + k\delta L + n\pi, \qquad (4.12)$$

where n is an integer. While performing the inverse tangent operation in equation (4.12), actual signs of $\tilde{S}_x$ and $\tilde{S}_y$ can be used to lower the phase ambiguity from $n\pi$ to $2n\pi$.

The ratio $\frac{\alpha}{\beta}$ will be close to unity if the following criteria are met:

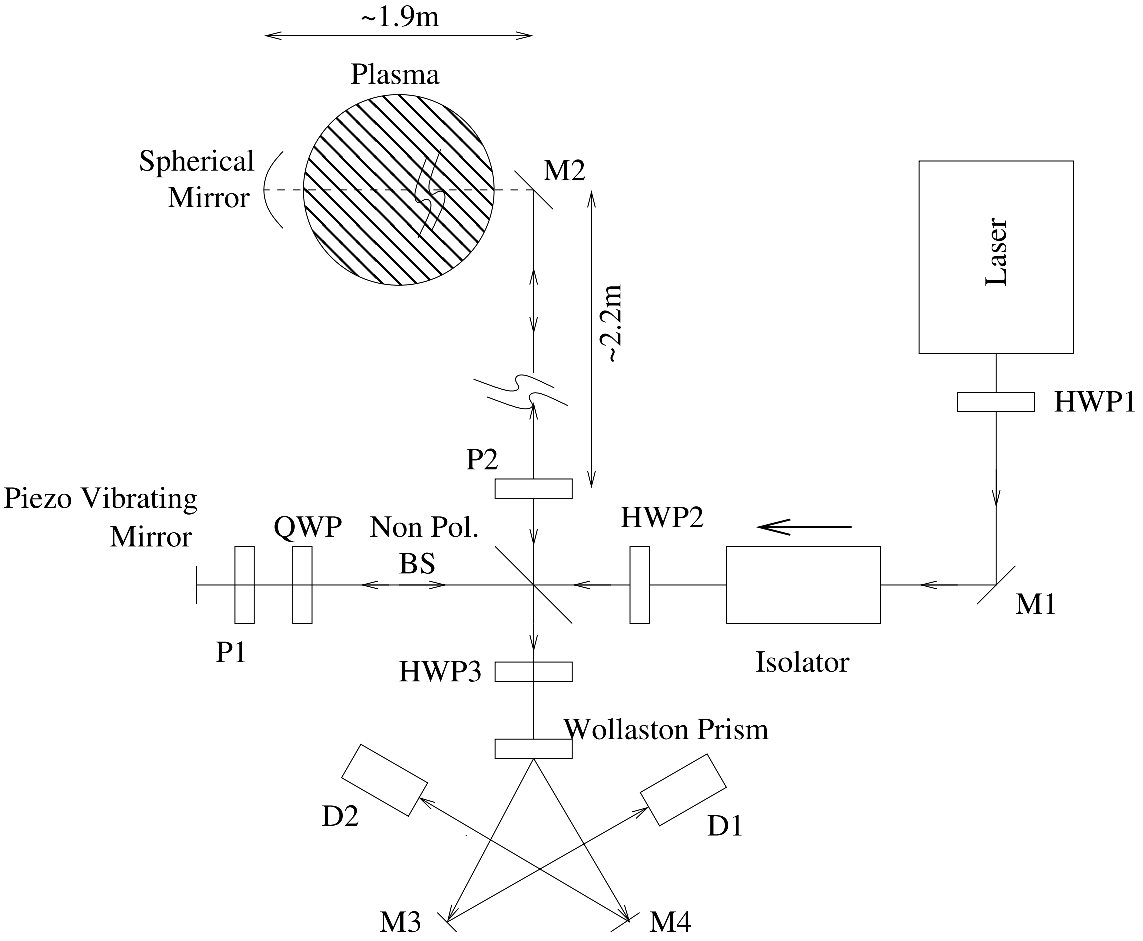

Figure 4.4: Setup of the homodyne interferometer for the Caltech spheromak experiment. The dotted beam signifies that the beam is coming out of the plane of the figure.

1. the angle of polarization, θ, of the linearly polarized scene beam is 45°;
2. the sensitivities of both of the detectors are equal;
3. and the beams are properly aligned so that almost equal power is coupled to each of the detectors.

4.4.2 Setup

Table 4.1: Description of some of the components used in the design of homodyne interferometer (refer to figure 4.4).

Component	Description
Laser	A 4 mW linearly polarized He-Ne laser with a cavity length of 25 cm. It produces a coherent beam of ~ 2 mm diameter at ~ 633 nm.
HWP1	Zero order half wave plate. It is used to rotate the polarization vector of the incoming beam to be vertical or horizontal.
Isolator	Manufactured by Optics for Research [47] (part number IO-5-660-LP). It prevents any reflected light from entering the laser.
HWP2	Zero order half wave plate. It transforms the beam coming out of the isolator into a vertically polarized beam. The polarization of the vertically polarized reference beam is unaltered upon reflection from mirrors or transmission through the beam splitter.
BS	A non-polarizing plate beam splitter was used to both split the beams and then recombine them.
QWP	Zero order quarter wave plate used to make the reference beam circularly polarized.
Piezo mirror	A mirror mounted on a piezo actuator. It could be vibrated with frequencies ranging from ~ 1 Hz to ~ 1 kHz.
P1 and P2	Dichroic polarizers in the reference and scene beam paths respectively. P2 was used to make the scene beam vertically polarized. P1 was used along with QWP to make the reference beam circularly polarized.

Continued on next page

Table 4.1: continued from previous page

Component	Description
SM	The radius of curvature of the spherical mirror (SM) is 4 m, the approximate distance the beam travels from the optical table to the spherical mirror, so the spherical mirror focuses the beam back to almost its original size. The spherical mirror's position can be adjusted to ensure that the path length difference between the scene and reference beams is approximately an even multiple of the laser cavity length.
HWP3	Zero order half wave plate, used to rotate the polarization angle of scene beam to 45°.
Wollaston prism	Used to split the scene and reference beams into $\hat{\mathbf{x}}$ and $\hat{\mathbf{y}}$ polarization components.
Mirrors	Plane mirrors are labeled by the letter M followed by a number. These are $1''$ diameter mirrors manufactured by Newport optics [48] (part number 10D10ER.1) and are used to steer the beams. Mirrors M2 is mounted on a damped rod attached to the vacuum chamber. It is used to direct the beam into the vacuum chamber through sapphire windows.
Detectors	The low noise, high gain detector amplifiers (Model 712A-2, from Analog Modules [49]) have a bandwidth of 200 Hz to 25 MHz.[1] The detector amplifier modules were housed in a RF shielded box and had a He-Ne filter in front.

A quadrature homodyne interferometer to measure plasma density was suggested by Buchenauer and Jacobson [41]. However, the optical arrangement they suggested is difficult to align over long distances. Hence the interferometer for the Caltech experiment was set up in Michelson double pass geometry as shown in figure 4.4. By interfering beams with

---

[1] Model 712A-2, being currently manufactured has a bandwidth of 250 Hz to 60 MHz.

a large path length difference, it was possible to locate most of the optical components on a small and accessible optical bench ($18'' \times 18''$). Table 4.1 describes the components used in the homodyne interferometer. The process for aligning the homodyne interferometer is describes in section A.2.

4.4.3 Results

Typical results from the homodyne interferometer are shown in figure 4.5.[2] The two quadrature signals from the detectors shown in blue and red are plotted in figure 4.5(a). Note that when one of the signals is at its maximum (or minimum), the other is passing through zero - a consequence of being in quadrature. Plasma causes the sudden change in the signals near 0 s.

The two signals in figure 4.5(a) are plotted as a Lissajous plot in figure 4.5(b). The data set corresponding to plasma is plotted as a solid red line while the non-plasma times are plotted in blue dots. The extent to which the signals are in quadrature can be estimated from the extent to which the plot resembles a circle. Note that refractive bending diminished the signal amplitude when the plasma intercepted the beam. The signal amplitude changed by different amounts on different detectors and hence may have caused a slightly erroneous measurement of density. Also note that the phase due to background vibrations changes by around 40° during the time in which the phase due to plasma has changed by $> 500°$.

Figure 4.5(c) plots the interpreted line average density from the interferometer. The slight drift in the signal is caused by mechanical vibrations of the mirrors and can be accounted for by a polynomial fit (of 4^{th} degree) to the phase corresponding to non-plasma times. The polynomial fit is shown in green in figure 4.5(c). The plasma density after subtracting the polynomial fit is shown in figure 4.5(d).

The mechanical vibrations of the mirror were used to calibrate the interferometer. Due to the combined effect of the piezo vibrating mirror and the mechanical vibrations in other mirrors, an interference signal with a bandwidth of a few kHz was observed in both the detectors, as shown in figure 4.5(a). This kHz scale signal was used to estimate the signal strengths α and β as described by equations (4.11). The ratio $\frac{\alpha}{\beta}$, thus estimated was used in equation (4.12). In other words, vibrations were used to calibrate the interferometer.

---

[2] This particular shot had two capacitors (59 μF each) being discharged across the plasma.

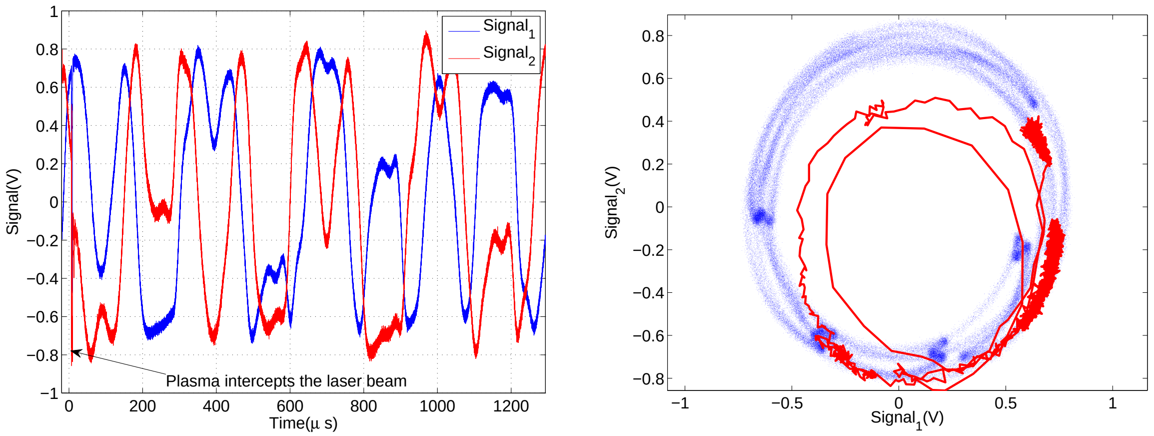

(a) Quadrature signals from the detectors.

(b) Lissajous plot of the quadrature signals. The data set corresponding to plasma intercepting the laser beam is plotted as a solid red line while the data corresponding to times with no plasma is plotted in blue dots.

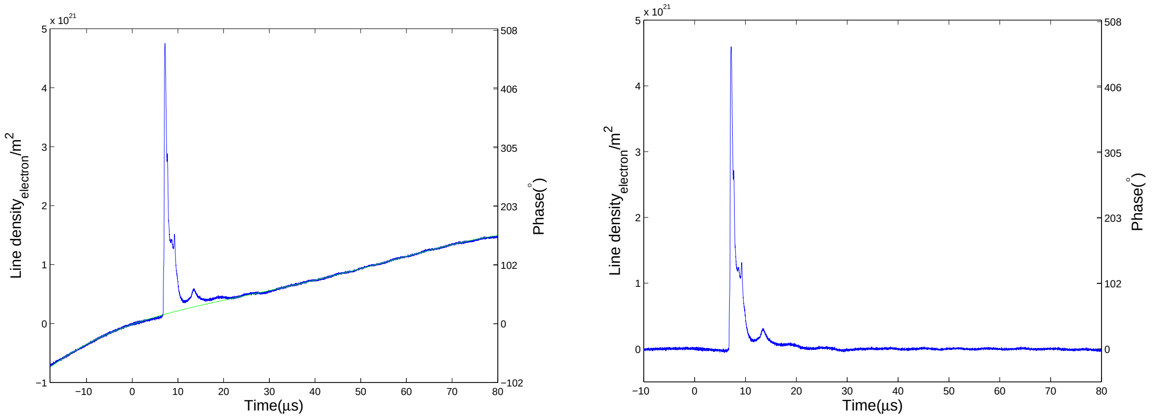

(c) Line averaged density interpreted from the signals. A polynomial fit to model the noise vibrations is shown in green.

(d) Line average density with the effect of mechanical vibrations compensated for.

Figure 4.5: Results from the homodyne interferometer for shot #7092.

When inferring the phase from the two detector signals, the relative amplitude, not the individual amplitude, of the signals is important. Quite often, refractive effects of plasma caused the amplitudes of the signals to vary (when the overlap of the beams was altered, or when beams fell on different parts of the detectors). These effects may increase or decrease the signal amplitudes and may produce errors in the phase detection. As seen by the red curve in figure 4.5(b), plasma effects caused the signal amplitude to change unequally in the two detectors. Buchenauer and Jacobson [41] countered the effects of refractive bending by focusing the scene beam at the center of plasma column.

4.4.4 Procedural Details

This section discusses certain procedural details for the homodyne interferometer.

1. The VME system introduced a fixed DC bias to the received signals. The bias was estimated by recording a temporary data set with no inputs or by looking at the mean of the maximum and the minimum of the quadrature signals.

2. The detectors were sensitive only to signals with frequencies greater than 200 Hz. Consequently, any signal that varied asymmetrically about zero would become “wavy” as the detectors filtered out its DC mean. In figure 4.5(a) the maxima (or minima) of a particular signal had slightly varying values. This is a consequence of a filtered DC mean. A changing DC mean corresponds to a changing position of the “center of the circle” in the Lissajous plot of figure 4.5(b). This caused the signal data to form more than one “circle.” The effect is usually more prominent than observed in figure 4.5. The varying DC mean makes it tricky to estimate the signal amplitude to get the ratio $\frac{\alpha}{\beta}$. The corresponding phase error, however, is minimal especially because the phase change caused by the plasma is about 2π. It is difficult to get high-gain photo-detector modules with bandwidth up to DC.

3. In a previous version of the interferometer, the mirror on top of the chamber was attached to the ceiling via a mount. Unfortunately, the ceiling is prone to vibrations, so the interferometer would misalign very frequently. Mounting the mirror on the chamber diminished the effects of these vibrations. However, quite often, the signal amplitude is seen to fluctuate with a period of about ~ 1 s. This may be caused by

a fluctuating overlap of the scene and the reference beam or by a fluctuating overlap of the beams on the detector.

4. After a few hours of interferometer operation, the signals were observed to fall out of quadrature by a few degrees ($< 5^\circ$). The quarter wave plate QWP had to be adjusted to bring the signals back into quadrature.

5. The laser had a switching power supply which operated at $\sim$ 18 kHz. If the piezo mirror was set to vibrate at this frequency, strange resonances were introduced, and the detector signals did not remain in quadrature. Thus the piezo vibrations were maintained between 1 and 4 kHz.

6. If a non-polarizing plate beam splitter was used, fringes were observed from just one beam due to reflections from the two surfaces. These were avoided by slightly misaligning the beam splitter. Cube beam splitters do not suffer from this drawback of self-interference, as they have just one surface for transmitting and reflecting.

7. Previously, $\gtrsim 50\%$ power was lost by the scene beam due to multiple reflections while passing through the sapphire windows. This power loss was minimized by an anti-reflection coating on the windows for the HeNe wavelength.

8. The data analysis relied heavily on the fact that the detector signals were in quadrature. Signal quadrature depended on the extent to which the beams were linearly or circularly polarized. Since good polarization was of critical importance, dichroic polarizers were used in the interferometer. These polarizers have a high extinction ratio of $1 : 10^4$ and a low transmittance of 36%. Consequently, substantial power was lost in these polarizers.

9. The polarizer P2 ensures that the scene beam is vertically polarized before interfering with the reference beam. Power loss in the scene beam is minimized if the optical axis of the sapphire windows is oriented along the polarization direction.

10. Zero order wave plates were used in the interferometer, as their properties are relatively insensitive to ambient temperature variations.

11. The interferometer alignment was “relatively” simple as the beams traced back the same path. This back reflection would have caused resonance modes in the laser if not for the isolator next to the laser.

4.4.5 Error Analysis

As described by Buchenauer and Jacobson [41], the phase error of the interferometer is $\sim \frac{\sigma}{\alpha}$, where σ is the standard deviation of the measured signal. This does not take into account the phase error due to a varying DC mean. The standard deviation can be easily estimated by smoothing the detector signal and taking its difference from the original measured signal. Typically this phase error is on the order of 2°.

4.4.6 Advantages

As compared to the original design by Buchenauer and Jacobson [41], the design of the interferometer for the Caltech Spheromak Experiment had the following advantages

1. Separate control of the phase quadrature and the relative amplitudes of two signals: The error performance of the interferometer is better if the two signals have equal amplitude. Their respective amplitude was adjusted by HWP3. Quadrature mismatch between the signals was improved by adjusting P1.

2. Only one mirror to adjust at long distances: The interferometer was aligned in an iterative scheme by first aligning all of its components alone on a small optical table and then by just adjusting the spherical mirror so that the scene beam traced back its path. Thus, as compared to the Mach-Zehnder geometry, only one mirror which was not on the table required alignment.

4.4.7 Disadvantages

1. Poor signal to noise ratio (SNR): As compared to the heterodyne interferometer, the homodyne interferometer has poor SNR performance.

2. Power inefficient: Due to stringent polarization requirements, significant amount of power ($\gtrsim 75\%$) is lost in the polarizers.

4.5 Heterodyne Interferometer

Heterodyne interferometers are usually simpler in design and alignment than homodyne interferometers. They also have better Signal to Noise Ratio (SNR). Thus the homodyne interferometer at the Caltech experiment was replaced by a heterodyne interferometer. The design for the interferometer was motivated by an interferometer built by Golingo [50].

4.5.1 Theory

Consider a vertically polarized reference beam with a frequency offset by an amount $\Delta\omega$ from the He-Ne frequency ω. The electric field of such a wave can be represented as:

$$\mathbf{E}_r = E_{0ry}\hat{\mathbf{y}}\cos(kL_r - (\omega - \Delta\omega)t).$$

The scene beam can have an arbitrary polarization, as it passes through birefringent material like the sapphire windows. The electric field of the scene beam may be represented as:

$$\mathbf{E}_s = E_{0sy}\hat{\mathbf{y}}\cos(kL_s - \Delta\phi_p - \omega t) + E_{0sx}\hat{\mathbf{x}}\cos(kL_s - \delta\phi - \Delta\phi_p - \omega t).$$

The phase difference $\delta\phi$ between the 2 polarizations may be caused by birefringent materials. If the scene and the reference beams interfere on a detector, the signal from the detector will be proportional to

$$\begin{aligned}
S &\propto \langle (E_{ry} + E_{sy})^2 + E_{sx}^2 \rangle \\
&\propto \langle (E_{0ry}\cos(kL_r - (\omega - \Delta\omega)t) + E_{0sy}\cos(kL_s - \Delta\phi_p - \omega t))^2 \\
&\quad + (E_{0sx}\mathrm{c\hat{o}s}(kL_s - \delta\phi - \Delta\phi_p - \omega t))^2 \rangle \\
&\propto E_{0ry}^2\langle \cos^2(kL_r - (\omega - \Delta\omega)t)\rangle + E_{0sy}^2\langle \cos^2(kL_s - \Delta\phi_p - \omega t)\rangle \\
&\quad + 2E_{0ry}E_{0sy}\langle \cos(kL_r - (\omega - \Delta\omega)t)\cos(kL_s - \Delta\phi_p - \omega t)\rangle \\
&\quad + E_{0sx}^2\langle \cos^2(kL_s - \delta\phi - \Delta\phi_p\omega t)\rangle \\
&\propto \frac{E_{0ry}^2 + E_{0sy}^2 + E_{0sx}^2}{2} + E_{0ry}E_{0sy}\langle \cos(\Delta\omega t - k\delta L - \Delta\phi_p)\rangle \\
&\quad + E_{0ry}E_{0sy}\langle \cos(k(L_s + L_r) - \Delta\phi_p - (2\omega - \Delta\omega)t)\rangle \\
\tilde{S} &\propto E_{0ry}E_{0sy}\cos(\Delta\omega t - k\delta L - \Delta\phi_p),
\end{aligned} \tag{4.13}$$

where $\tilde{S}$ represents the AC component of the signal. $\delta L = L_r - L_s$ is the fluctuating change in path lengths caused by mechanical vibrations. The detector is fast enough to track changes occurring at frequency $\Delta\omega \sim 80$ MHz but averages out any changes occurring at He-Ne frequencies or higher. Refractive bending may cause the signal amplitude of the detector to change as a function of time, so the detector signal can be expressed as

$$\tilde{S} = F(t)\cos\left(\Delta\omega t - k\delta L - \Delta\phi_p\right), \tag{4.14}$$

where the rate of change of $F(t)$ is slow compared to $\Delta\omega$. Next, the signal from the detector described by equation (4.14) is demodulated to recover the phase information. To do so, the coupled signal from the radio frequency (RF) source at $\Delta\omega = 80$ MHz is split into quadrature components: $A\cos(\Delta\omega t + \varphi)$ and $B\sin(\Delta\omega t + \varphi)$, where φ is the phase shift caused by the transmission cables. The detector signal from equation (4.14) is split into two equal parts and mixed (multiplied) by the quadrature signals. The resulting signals coming out of the mixers are given by:

$$\begin{aligned}
S_1 &= \frac{F(t)A}{2}\cos\left(\Delta\omega t - k\delta L - \Delta\phi_p\right)\cos(\Delta\omega t + \varphi) \\
&= \frac{F(t)A}{4}\left(\cos\left(k\delta L + \Delta\phi_p + \varphi\right) + \cos\left(2\Delta\omega t + \varphi - k\delta L - \Delta\phi_p\right)\right) \\
S_2 &= \frac{F(t)B}{2}\cos\left(\Delta\omega t - k\delta L - \Delta\phi_p\right)\sin(\Delta\omega t + \varphi) \\
&= \frac{F(t)B}{4}\left(\sin\left(k\delta L + \Delta\phi_p + \varphi\right) + \sin\left(2\Delta\omega t + \varphi - k\delta L - \Delta\phi_p\right)\right) \qquad (4.15)
\end{aligned}$$

On low-pass filtering the above signals, we get quadrature signals:

$$\begin{aligned}
S_1 &= \frac{F(t)A}{4}\cos(\Delta\phi_p + \varphi'), \\
S_2 &= \frac{F(t)B}{4}\sin(\Delta\phi_p + \varphi'),
\end{aligned}$$

where $\varphi' = \varphi + k\delta L$ is constant for the scale of the experiment. The phase shift caused by the plasma can be calculated by taking the inverse tangent of the ratio of the two signals. Note that taking the ratio of the signals eliminates the time dependence caused by refractive

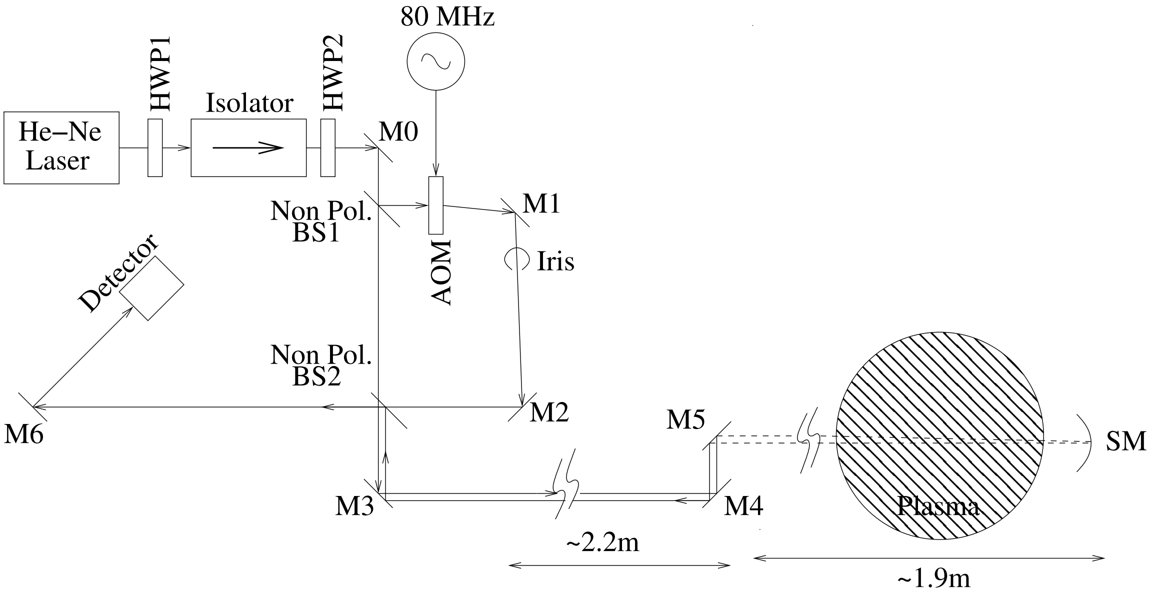

Figure 4.6: Setup of the heterodyne interferometer for the Caltech spheromak experiment. The dotted beam signifies that the beam is coming out of the plane of the figure.

bending $F(t)$. The plasma phase shift can be estimated as

$$\Delta\phi_p = \tan^{-1}(\frac{S_2}{S_1}\frac{A}{B}) - \varphi' + n\pi. \tag{4.16}$$

4.5.2 Setup

Table 4.2: Description of some of the components used in the design of the heterodyne interferometer (refer to figure 4.6).

Component	Description
Laser	A 4 mW linearly polarized He-Ne laser with a cavity length of 25 cm. It produces a coherent beam of $\sim$ 2 mm diameter at $\sim$ 633 nm.
HWP1	Zero order half-wave plate. It is used to rotate the polarization vector of the laser beam so that it aligns with the direction of the polarizer at the input of the isolator.
	Continued on next page

Table 4.2: continued from previous page

Component	Description
Isolator	Manufactured by Optics for Research [47] (part number IO-5-660-LP). It prevents any reflected light from entering the laser.
HWP2	Zero order half-wave plate. It transforms the beam coming out of the isolator into a vertically polarized beam. The polarization of the vertically polarized reference beam is unaltered upon reflection from mirrors, beam splitter or from transmission through the acousto-optic modulator (AOM).
Non pol. BS1	Non-polarizing plate beam splitter is used to split the beam into a scene and a reference beam.
AOM	The acousto-optic modulator (AOM). Up to 86% of the input power to the AOM can be coupled into its first harmonic output. The iris obstructs all other beams except for the first harmonic.
Mirrors	Plane mirrors are labeled by the letter M followed by a number. These are 1″ diameter mirrors manufactured by Newport optics [48] (part number 10D10ER.1) and are used to steer the beams. Mirrors M4 and M5 are mounted on a damped rod attached to the vacuum chamber. They are used to direct the beam into the vacuum chamber through sapphire windows.
Non pol. BS2	Non polarizing cube beam splitter used to recombine the scene and reference beams.

Continued on next page

Table 4.2: continued from previous page

Component	Description
SM	The radius of curvature of the spherical mirror (SM) is 4 m, the approximate distance the beam travels from the optical table to the spherical mirror, so the spherical mirror focuses the beam back to almost its original size. The spherical mirror position can be adjusted to ensure that the path length difference between the scene and reference beams is approximately an even multiple of the laser cavity length.
Detector	UDT Sensors part number HR040L [51] with bandwidth $\sim$ 500 MHz used in a reverse biased mode.
RF electronics	All the components shown in figure 4.7 were off-the-shelf components from Mini Circuits. The components were selected based on their power ratings.

Figure 4.6 shows the schematic for the interferometer. The RF electronics for demodulating the signal are shown in figure 4.7. The interferometer described in figure 4.6 is set up in a double pass geometry. By interfering beams with a large path length difference, it was possible to locate most of the optical components on a small and accessible optical bench ($18'' \times 18''$). Mirror M4 and the spherical mirror SM are mounted on the vacuum chamber. They direct the laser beam through the plasma (via sapphire windows) and back to the optical bench. Sapphire is a birefringent material, and the windows are oriented to minimize the change in the polarization of the scene beam. Note that equation (4.13) implies that the interference signal strength is maximized if the polarization of the interfering beams is the same.

A major advantage of the design shown in figure 4.6 is the ease of alignment. The two beams are arranged to overlap each other simply by adjusting the cube beam splitter BS2, and the mirror M2. Both these components are located on the optical bench and are easily accessible. A cube beam splitter was used for combining the beams instead of a plate beam splitter since a cube beam splitter does not introduce any lateral shift in the position of the

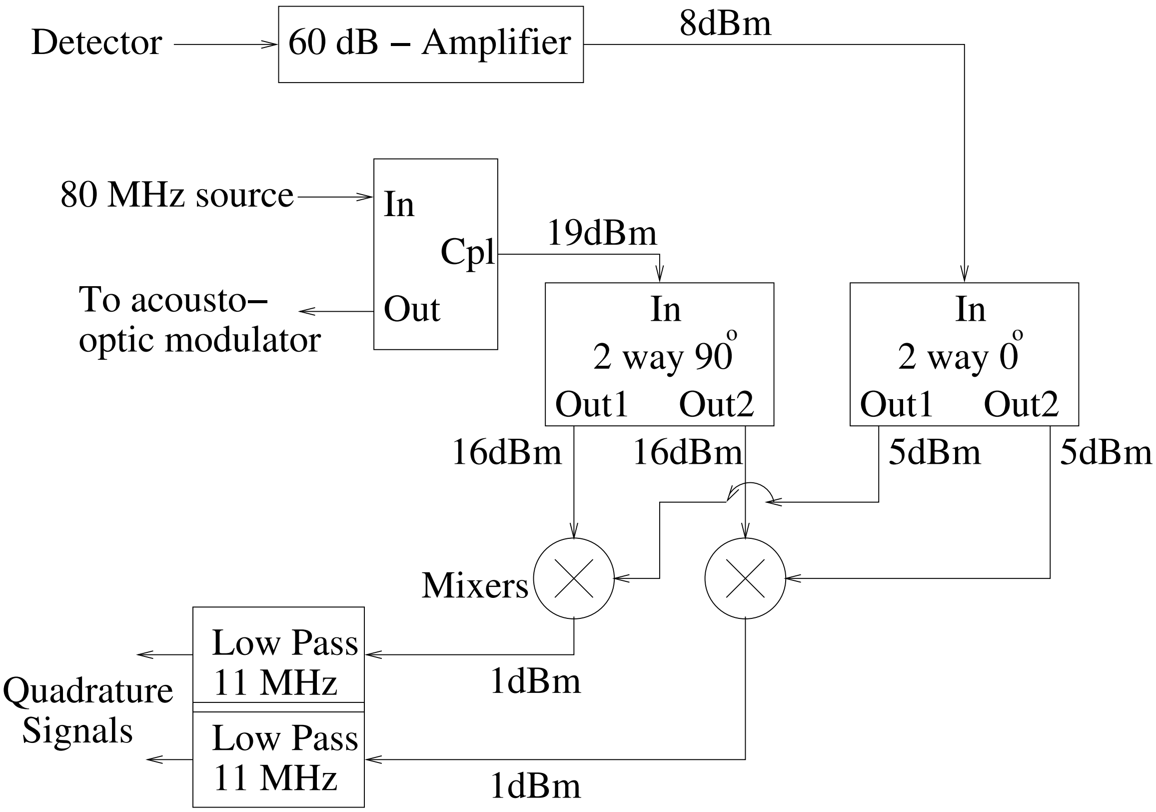

Figure 4.7: RF circuit for the heterodyne interferometer. Typical signal power in dBm is mentioned for each connection.

passing beam. The process for aligning the homodyne interferometer is describes in section A.2.

4.5.3 Results

Typical results from the heterodyne interferometer are shown in figure 4.8. The two quadrature signals after demodulation are shown in blue and red in figure 4.8(a). Note that when one of the signals is at its maximum (or minimum), the other is passing through zero - a consequence of being in quadrature. Plasma causes the sudden change in the signals near 0 s.

The two signals plotted in figure 4.8(a) are plotted as a Lissajous plot in figure 4.8(b). The data set corresponding to the beam passing through the plasma is plotted as a solid red line while the non plasma times are plotted in blue dots. The extent to which the signals are in quadrature can be estimated from the extent to which the plot resembles a circle. Note that refractive bending intensified the signal amplitude when the plasma intercepted the beam. Provided that the beams undergo only a “small” displacement because of refractive bending, taking the ratio of the two signals removes the effects of refractive bending on the phase inferred [42]. Also note that the phase due to background vibrations changes by around 40° during the time in which the phase due to plasma changes by $> 200^\circ$.

Figure 4.8(c) plots the interpreted line average density from the interferometer. The slight drift in the signal is caused by mechanical vibrations of the mirrors, and can be accounted for by a polynomial fit (of 4^{th} degree) to the phase corresponding to non plasma times. The polynomial fit is shown in green in figure 4.8(c). The plasma density after subtracting the polynomial fit is shown in figure 4.8(d).

4.5.4 Procedural Details

In this section certain procedural details for the heterodyne interferometer are discussed.

1. The interferometer was aligned in a hybrid geometry motivated by the Michelson and Mach-Zehnder designs. The beams did not trace back their paths, so did not come back to the laser. Yet, the isolator was placed in front of the laser to remove any possibility of light coming back to the laser and effecting its stability.

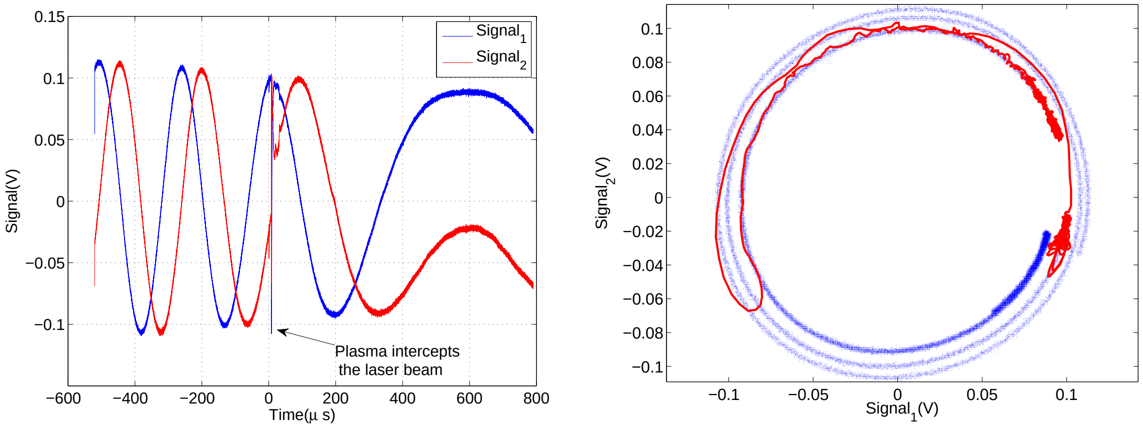

(a) Quadrature signals after demodulation.

(b) Lissajous plot of the quadrature signals. The data set corresponding to plasma intercepting the laser beam is plotted as a solid red line while the data corresponding to the times with no plasma is plotted in blue dots.

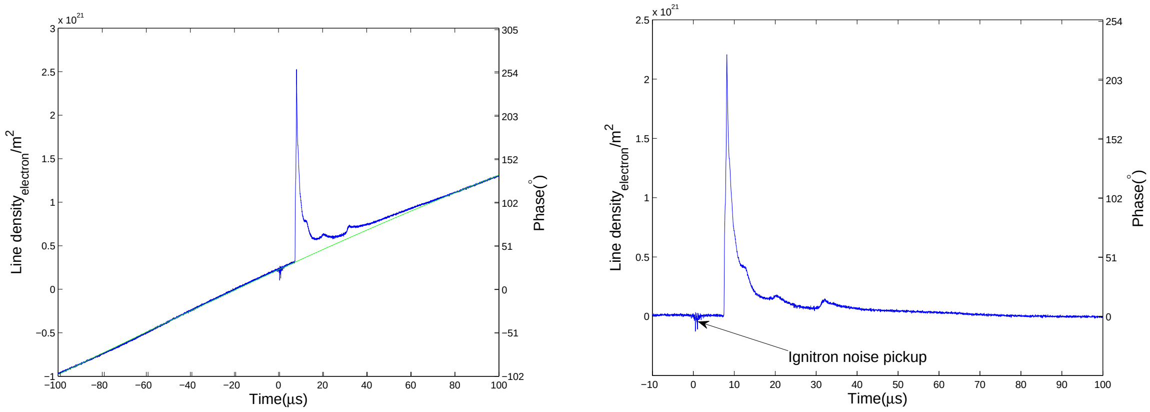

(c) Line average density interpreted from the signals. Polynomial fit to model the noise vibrations is shown in green.

(d) Line averaged density with the effect of mechanical vibrations compensated for.

Figure 4.8: Results from the heterodyne interferometer for shot #9114.

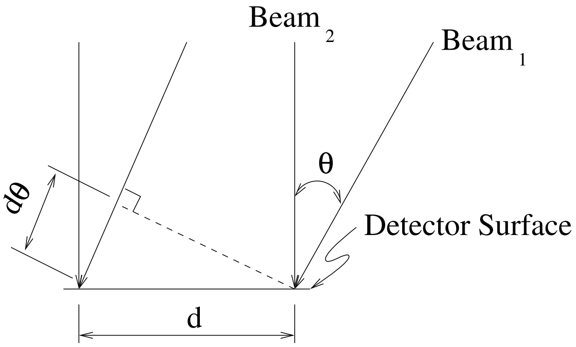

Figure 4.9: Effect of misalignment on detector signal.

2. As noted in section 4.4.4, the VME system introduced a DC bias to the measured signals.

3. When aligning the homodyne interferometer, fringe patterns were observed when the scene and reference beams overlapped reasonably well. This provided a visual feedback on the degree of alignment. However, because of the 80 MHz modulation, fringe patterns could not be observed for the heterodyne interferometer.

   Let θ be the angle of misalignment of the beams on a detector with diameter d (see figure 4.9). To ensure that the beams remain sufficiently coherent on the surface of the detector, it is required that $d\theta \ll \lambda$. For a detector of diameter $\sim 1000\ \mu$m, this implies that the beams have to be aligned up to $\theta \ll 0.03°$. Thus, while a smaller detector has better frequency response, it is undesirable when considering beam alignment. The process for aligning the beams is described in section A.1.3.

4. In many heterodyne interferometers, the scene and the reference beams are the 0^{th} and the 1^{st} harmonics coming out of the AOM [34, 36, 37, 39, 52, 53]. This approach requires many mirrors to steer the beams long enough before the scene beam can be directed to the vacuum chamber. Instead, as suggested by Kawano et al. [38, 40], a beam splitter (BS1 in figure 4.6) was used to split the beams. However this approach was slightly power inefficient as only $\sim 86\%$ of the input beam power can be coupled to the first harmonic by the AOM.

5. The 90° splitter in the demodulation circuit (figure 4.7) has slightly different gains for each of its output channels. This resulted in a slight difference ($\sim 3\%$) in the

signal amplitudes of the quadrature signals of the interferometer. Since the gain was constant over time, it was compensated for in the software written to interpret the phase from the quadrature signals.

4.5.5 Error Analysis

The phase ambiguity of the signals is given by σ/A [41], where σ is the rms error in the signal and A is the strength of the signal. For typical data this was $\sim 1^\circ$, corresponding to a density error of $\sim 10^{19}/\mathrm{m}^2$.

4.5.6 Advantages

As compared to the homodyne interferometer described in section 4.4, the heterodyne interferometer had the following advantages:

1. Bandwidth extending to DC: The bandwidth of the RF mixers shown in figure 4.7 extends to DC. Thus, unlike the homodyne interferometer, the heterodyne interferometer can measure a steady phase difference. This also prevented a spurious introduction in the mean value of the signal, as occurred for the homodyne interferometer (see section 4.4.4, point 1).

2. High SNR: The heterodyne interferometer had about a factor of two better noise performance than the homodyne interferometer.

3. No drift in quadrature: As mentioned in point 4 of section 4.4.4, the homodyne signals would drift out of quadrature with time. For the heterodyne interferometer, the phase quadrature was generated by RF electronics, so no drift was observed.

4. Simpler alignment: Aligning the homodyne interferometer required adjusting the spherical mirror SM (see figure 4.4), which was very inaccessible. However, aligning the heterodyne interferometer only involved adjusting the beam splitter BS2 and the mirror M2, both of which were on the optical table and hence extremely accessible.

5. Unaffected by refractive bending of light: As explained in the discussion just prior to equation (4.16), the phase detection of a heterodyne interferometer is unaffected by refractive bending of light.

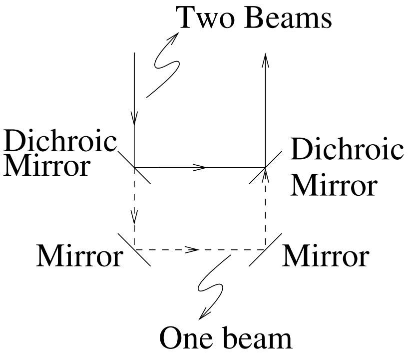

Figure 4.10: A plausible setup to alter the path length of the reference beam of a two-color interferometer. The dichroic mirrors reflect one beam and transmit the other.

4.5.7 Disadvantages

An extra mirror M4 was used in the heterodyne interferometer to steer the beam through the vacuum chamber. The extra mirror lowered the alignment complexity of the interferometer. However, it also increased the mechanical vibrations in the beam's path.

4.6 Conclusion

He-Ne homodyne and heterodyne interferometers were developed for the Caltech spheromak formation experiment. The designs were especially suited for fast plasma experiments with time scales much smaller than the time scales of mechanical vibrations of the mirrors. The interferometers operated well even though there is a path length difference of ~ 8 m between the scene and the reference beams. Operating at such a large path length difference considerably reduced the number of optical components and also made alignment much easier.

Line densities of the order of $5 \times 10^{21}/\mathrm{m}^2$ were observed in the experiment. Assuming a double pass plasma length $L \sim 12$ cm, as shown in the figure 1.7(b), corresponds to average densities of $\sim 4 \times 10^{22}/\mathrm{m}^3$. These results are in good agreement with the densities inferred from Stark broadened spectral lines [54].

The idea of operating at a large path length difference could in principle be applied to two-color interferometers as well. The beams in a two color interferometer might have different periods for their phase auto correlation function. A plausible way of altering the path length of reference beam is suggested in figure 4.10. For a two-color interferometer with lasers with the same cavity length, or with a single laser [37], only a single normal mirror would be needed to adjust the length of the reference beam.

4.7 Future Extension

The interferometer setup for the Caltech experiment could probe only one spatial location corresponding to the first available view ports. To overcome this limitation, a future designs of the interferometer should use fiber optics to couple light into and out of the vacuum chamber [55, 56].

Chapter 5

Non-equilibrium Alfvénic Plasma Jets Associated with Spheromak Formation

Strong MHD-driven flows have been observed over a wide range of scales from terrestrial experiments (coaxial gun accelerators [57–59], plasma thrusters [60, 61], high-current arcs [62], Z-pinch formation [63], spheromak formation [22] and sustainment [64]) to extra-terrestrial phenomenon (solar coronal mass ejections [65] and astrophysical jets [66]).

One of the earliest experimental observation of flows during spheromak formation was done by Uyama et al. [67] using Doppler shift measurements. Strong flows have also been observed during the helicity injection stage in the Caltech spheromak experiment. These flows are not predicted by Taylor's relaxation theory [10], and so during this stage, the plasma should not be considered to be evolving through a series of equilibrium stages, as has been previously assumed [22].

It is shown in this chapter that MHD driven flows are generated because of the flaring of the poloidal current channel profile, i.e., $\partial I/\partial z \neq 0$. Reed [62] argued that the flow velocities, u, should scale as $I^{\frac{1}{2}}$ in flared high current arcs, where I is the current in the arc. This is in contrast to the $u \sim I$ scaling found for the jets in Caltech spheromak experiment. Barnes et al. [64] also developed a model to predict plasma flow from the electrodes in a steady state driven spheromak, but did not take into account the plasma pressure. They argued that the plasma flows should be Alfvénic leading to a gun voltage which scales as I^3. Their experiments showed gun voltage scaling as I^2, but no measurements of plasma velocity were reported.

This chapter consists of five sections. Section 5.1 describes the sequence of plasma dynamics leading to jet formation. Section 5.2 describes the experimental results showing the magnetic field structure in the jet, the velocity scaling of the jet and also its pressure scaling. A MHD model for these jets is presented in section 5.3. Section 5.4 presents an energy balance argument for the jets and also justifies the observed small radial extent of the plasma in these jets. Finally, section 5.5 concludes the chapter by summarizing its main results.

5.1 Introduction

As shown in section 3.3, the plasma jet can be considered an inductive load. Figure 5.1 shows a series of plasma images which elucidate the sequence of plasma evolution leading to a changing inductance. Initially ($\sim 0.5\ \mu$s after breakdown) *eight spider legs* are formed linking the gas nozzles on the two electrodes. The collimation and flow of plasma in the spider legs was studied by You et al. [12]. As the current ramps up, the spider legs expand due to hoop force and then merge to form a central column jet because of the pinch force ($\sim 3\ \mu$s after breakdown). This results in a slightly flaring plasma jet which drives plasma from near the electrodes to the vacuum. The jet is extremely dense ($\beta \sim 1$) and expands at Alfvénic velocities [54]. As the jet evolves outward, it increases the plasma inductance and thus acts as a helicity injection mechanism (see section 2.1). This chapter shows that MHD driven flows act as the mechanism to drive the change in the inductance of the plasma jet. As the jet expands towards vacuum, it eventually overcomes the Kruskal-Shafranov kink instability [7, equation 10.190] condition (due to an increased axial length), and can detach to form a spheromak like configuration. Kinking of the plasma jet, detachment from the electrodes and spheromak formation has been studied earlier [13, 68].

5.2 Results

5.2.1 Magnetic Field Structure in the Jets

The magnetic probe described in section 1.3.1 was used to measure the magnetic field and current distribution in the plasma jets. Figure 5.2 shows the typical poloidal current and flux profiles in the jet. As discussed in section 1.3.1, the poloidal flux profile may not

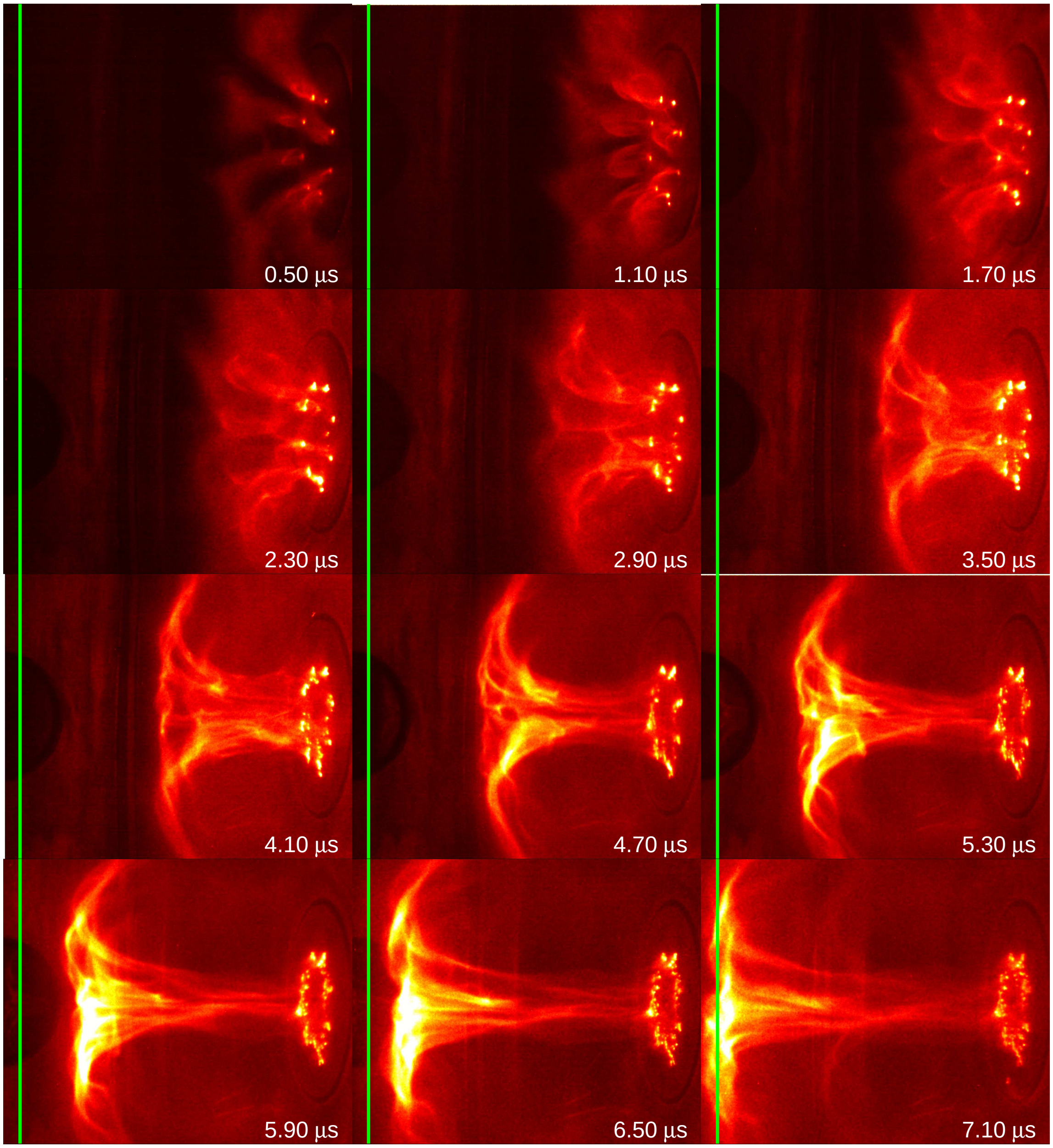

Figure 5.1: False colored visible images depicting the formation of hydrogen plasma jet from shot #9920 and #9923. The green vertical lines represent the path of the laser beam used to measure plasma density.

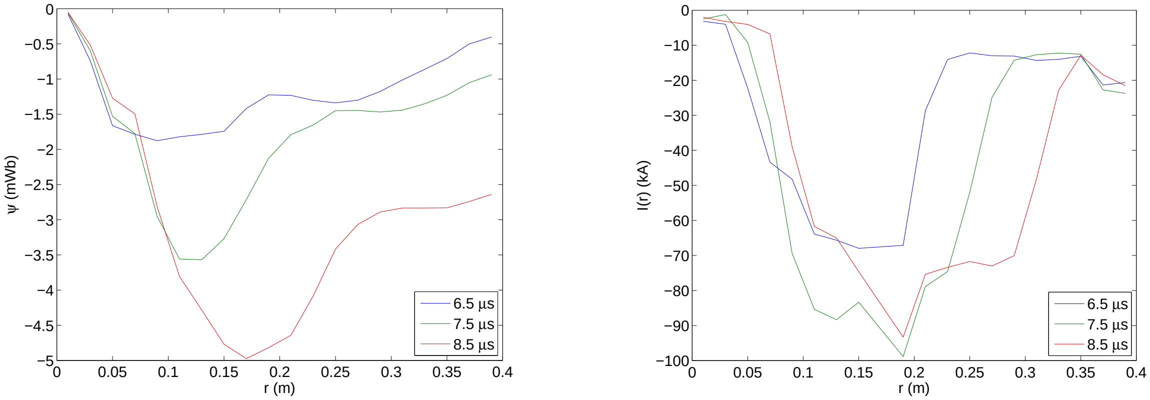

(a) Poloidal flux surface observed in the plasma jet from shot #9957 at $z = 20$ cm.

(b) Axial current contours observed in the plasma jet from shot #9957 at $z = 20$ cm.

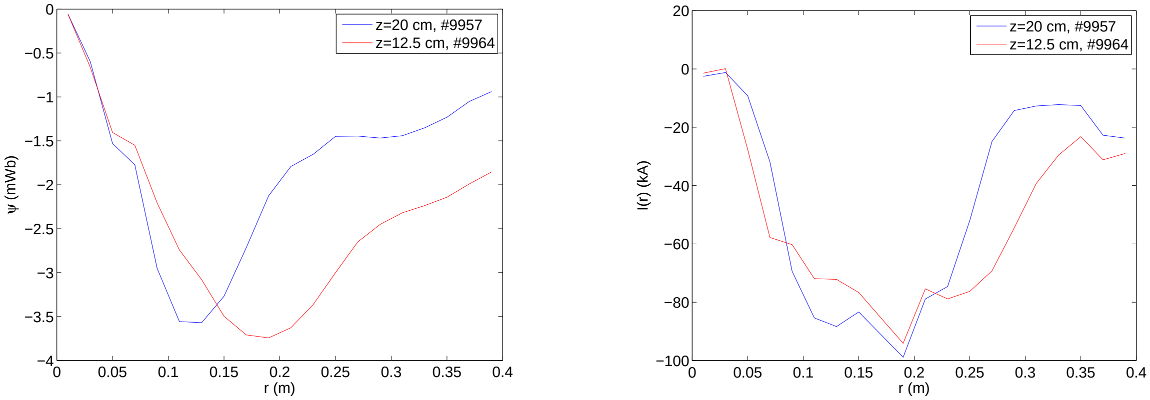

(c) Poloidal flux contour at two different locations $z = 12.5$ cm and $z = 20$ cm measured at $t = 7.5$ μs after breakdown.

(d) Axial current contour at two different locations $z = 12.5$ cm and $z = 20$ cm measured at $t = 7.5$ μs after breakdown.

Figure 5.2: Poloidal current and flux surfaces of hydrogen plasma jets.

be accurate because of integration and alignment errors. The poloidal flux profile is still expected to give an intuitive understanding.

Figure 5.2(a) shows the poloidal flux profile at different time instances for a single plasma jet at a distance $z = 20$ cm from the electrode. The axial magnetic field B_z is strong where the flux contours are steep, i.e., B_z has a radial extent of about 10 cm. Also, note that the poloidal flux surfaces flare outward with time.

Figure 5.2(b) shows the poloidal current profile at different time instances for a single plasma jet at a distance $z = 20$ cm from the electrode. From the figure it is noted that J_z has a radial extent of about 10 cm and that that the axial current contours flare outward with time (similar to the poloidal flux contours in figure 5.2(a)).

The poloidal flux in the jet at two different axial positions is shown in figure 5.2(c). The figure is inconclusive regarding the flaring of the poloidal flux contours.

The poloidal current in the jet at two different axial positions is shown in figure 5.2(d). It is clear from the data that the current channel flares and hence toroidal magnetic field pressure decreases with increasing axial distance from the electrode. The radial extent of the current channel increases from about 7 cm at $z = 12.5$ cm to about 9 cm at $z = 20$ cm. Thus if the radius of the flaring current channel is modeled as $a(z) = a_\circ e^{\kappa z}$, then $\kappa \sim 2\ \mathrm{m}^{-1}$.

5.2.2 Speed of the Jets

The He-Ne interferometer [69] described in section 4.5 was used to measure the density of the plasma jets. The interferometer beam (shown as a vertical green line in figure 5.1) intercepted the plasma jet at a distance of 29 cm from the planar electrodes.

Figure 5.3 shows typical line-averaged density traces from the interferometer, for hydrogen and deuterium plasma jets. From visible images, the radius of the jet is estimated to be about 3 cm (see figure 5.1) and so the nominal density of the jets is $\sim 3 \times 10^{22}/\mathrm{m}^3$.

An obvious characteristic of the density traces shown in figure 5.3 is the extremely sharp rise time in the observed density as the apex of the plasma jet traverses the path intercepted by the laser beam. This sharp rise time gives a time of flight measurement and can be used to estimate the average velocity of the plasma as $v = \frac{\mathrm{L{=}29cm}}{\text{time of flight}}$.

Figure 5.4 plots the time of flight velocity of hydrogen plasma jets as a function of the maximum gun current flowing through the jet. Plasma experiments were done with fast gas

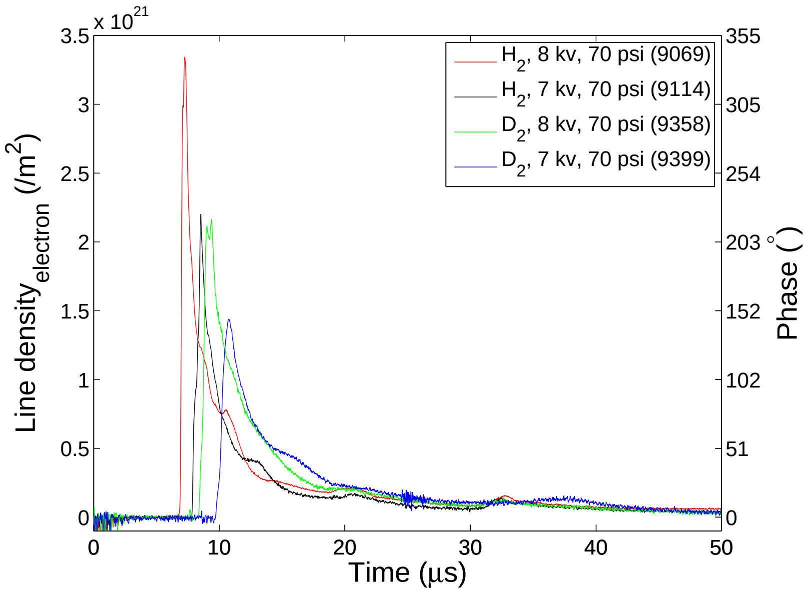

Figure 5.3: Typical interferometer density traces from the plasma jets.

puff valves pressurized with H_2 at either 70 or 100 psi. It is seen from figure 5.4 that plasma jets with 70 psi gas valve pressure are faster. This demonstrates that the dominant flow mechanism in the jet cannot be hydrodynamic, i.e., cannot be driven by pressure gradient ∇P, since if the jet were driven by ∇P, a 100 psi jet should move faster than a 70 psi jet. Also, if the dominant flow mechanism were hydrodynamic, then the characteristic velocity would be $c_s \sim 2$ km/s, which is much smaller than the velocity of the jets shown in figure 5.4.

Figure 5.5 plots the average velocity of hydrogen and deuterium plasma jets as a function of the maximum gun current flowing through the plasma. This shows that the velocity of a plasma jet is proportional to the current flowing through the plasma and that the hydrogen plasma jets are faster than the deuterium ones. The high flow speed and its dependence on mass and current indicate that the plasma jet's behavior is in sharp contrast to a previously considered model for astrophysical jets that describes their evolution as series of Grad-Shafranov equilibria [7, Chapter 9.8.3] with boundary conditions determined by the twist of poloidal field lines [70, 71]. Note also that in such models, a low density magnetically dominated quasi-equilibrium jet expands against an external plasma with higher pressure, whereas the laboratory jets in our experiment expand into a vacuum.

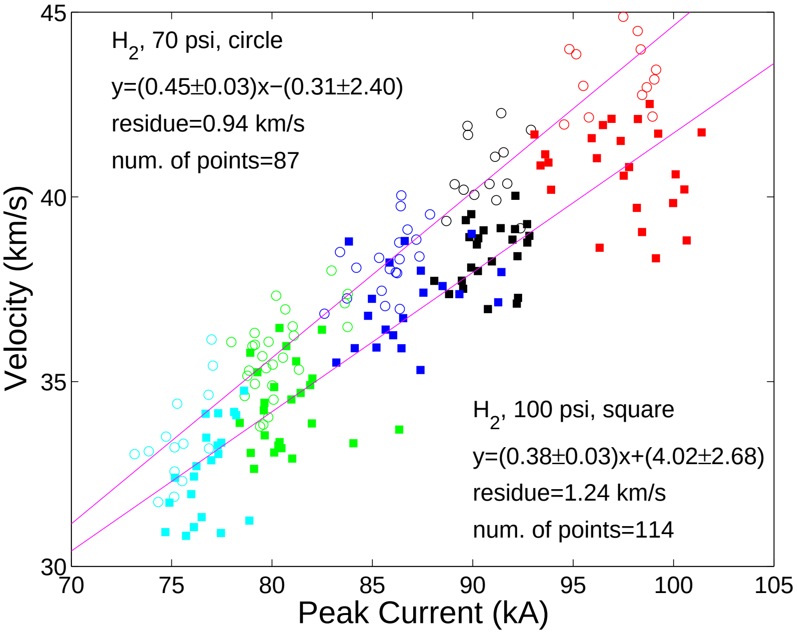

Figure 5.4: Velocity of hydrogen plasma jets as a function of the maximum gun current. Measurements from shots when the fast gas valves were pressurized to 70 and 100 psi are plotted as circles and squares respectively. Here, and in subsequent figures, the cyan, green, blue, black, and red data points refer to the gun discharge voltage of 6, 6.5, 7, 7.5 and 8 kV respectively. Also, the linear fit to the respective data points is plotted in magenta, and the equation for the linear fit and corresponding error is shown next to the lines. For the linear fit, y represents the velocity in km/s, and x represents the peak current in kA.

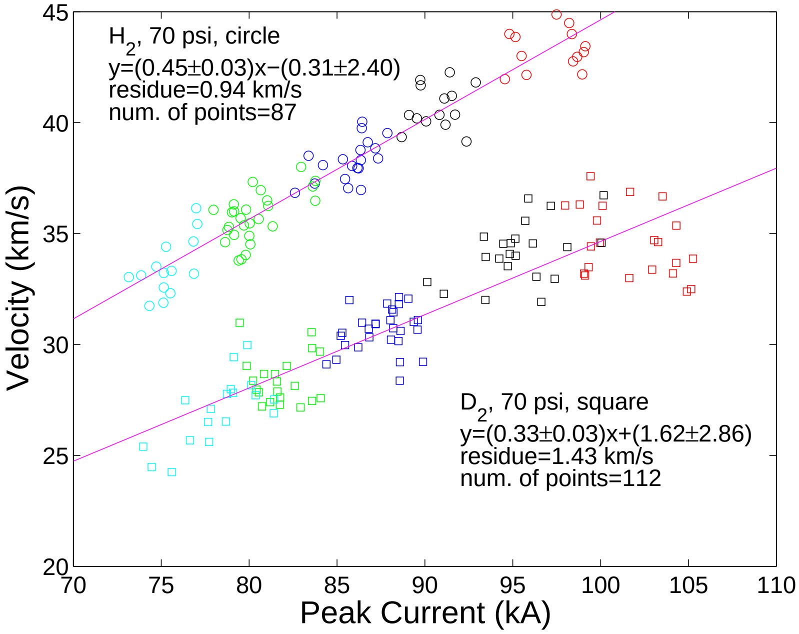

Figure 5.5: Velocity of plasma jets as a function of the maximum gun current for H_2 and D_2 plasmas plotted in circles and squares respectively. The fast gas valves were pressurized to 70 psi.

5.2.3 Density of the Jets

Figure 5.6 shows that plasma pressure is proportional to the toroidal magnetic field energy density and that the plasma jets have $\beta_\phi := \frac{nkT_i}{B_\phi^2/2\mu_\circ} \sim 0.5$. For thermal energy density nkT_i in figure 5.6, ion temperature was assumed to be 2 eV [17] for all the shots, and density was inferred from the peak of density traces (see figure 5.3) assuming a plasma radius of 10 cm. Toroidal field energy density $(B_\phi^2/(2\mu_\circ))$ was calculated using $B_\phi = \mu_\circ I/(2\pi a)$, where I is the instantaneous current flowing through the plasma when the density was measured, and a, the radius of current channel, was assumed to be 10 cm. Also the typical axial field in the experiment was $B_z \sim 0.2$ T, which corresponds to $\beta_z := \frac{nkT_i}{B_z^2/2\mu_\circ} \sim 0.1 - 0.2$. Plasma density was observed to scale directly with B_ϕ and inversely with B_z.

Figure 5.7 plots the plasma pressure as a function of toroidal magnetic field energy density for D_2 plasma jets. While the data has more scatter compared to figure 5.6, it is seen that $\beta_\phi \sim 1$ for shots involving higher poloidal current (the red and black squares).

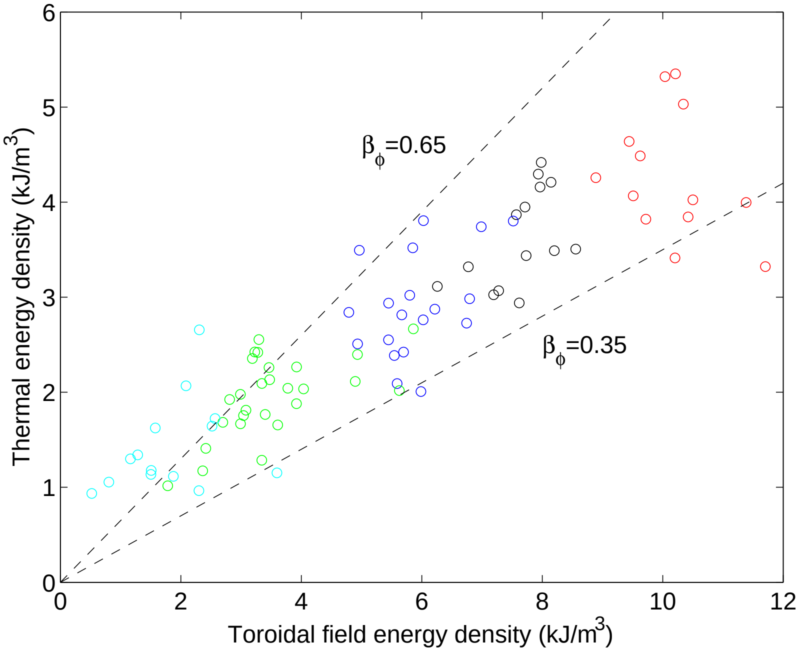

Figure 5.6: Thermal energy density as a function of toroidal magnetic field energy density for hydrogen plasma jets.

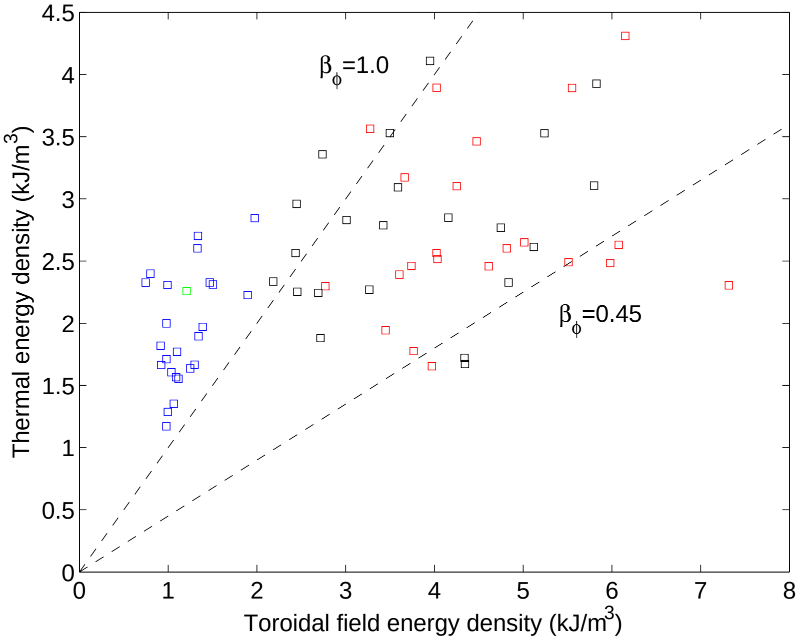

Figure 5.7: Thermal energy density as a function of toroidal magnetic field energy density for deuterium plasma jets.

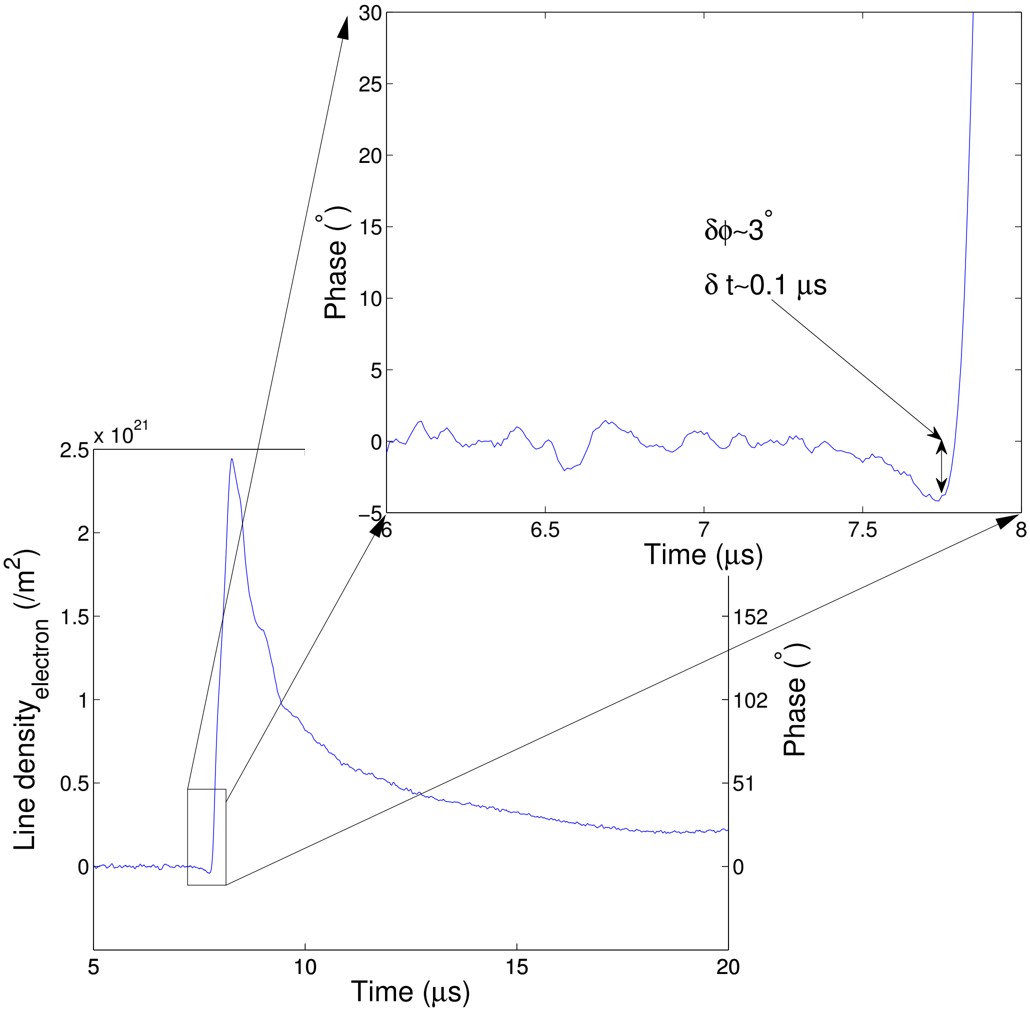

Figure 5.8: Density of the hydrogen plasma jet produced by gas valve pressurized to 100 psi. Shot #9205.

5.2.4 Distribution of Neutrals in the Jet

It is seen from figure 5.4 that plasma jets produced when the fast gas valves were pressurized to 100 psi are slower. A typical density trace from such plasma shots is shown in figure 5.8. The inset shows that just before the plasma intercepts the laser beam, there is a "negative dip" in density. The negative dip corresponds to a phase change of $\delta\phi \sim 3^\circ$, and has a duration of $\delta t \sim 0.1$ μs. The negative dip is from refractive index of neutrals in front of the jet being pushed along. The refractive index of a dense neutral gas is given by the

Gladstone-Dale relation [72, Chapter 2]:

$$\rho = K(\mathfrak{n} - 1) = K\delta\mathfrak{n},$$

where ρ is the mass density, K is the proportionality constant, $\mathfrak{n}$ is the refractive index of the gas, and $\delta\mathfrak{n} := \mathfrak{n} - 1$ is the difference between the refractive index of the gas and the refractive index of vacuum.

The phase difference measured by the interferometer because of neutral gas is

$$\delta\phi = \int \delta k \ \mathrm{d}x = \int \frac{2\pi}{\lambda}\delta\mathfrak{n} \ \mathrm{d}x \sim \frac{2\pi L}{\lambda}\delta\mathfrak{n},$$

where λ is the free space wavelength of He-Ne laser and $L \sim 20$ cm is the length of the path of the laser beam within the dense neutral gas. Thus a phase change of $\delta\phi \sim 3^\circ$ corresponds to $\delta\mathfrak{n} \sim 10^{-7}$.

For hydrogen, $\delta\mathfrak{n} \sim 10^{-4}$ at NTP(normal temperature and pressure) [73, Page E-224]. Thus the number density of neutrals in front of the jet, $n_{\text{experiment}}$, is given by

$$\frac{n_{\text{experiment}}}{n_{\text{NTP}}} \sim \frac{\delta\mathfrak{n}_{\text{experiment}}}{\delta\mathfrak{n}_{\text{NTP}}} \sim \frac{10^{-7}}{10^{-4}}.$$

Thus the number density of neutrals in front of the jets produced by gas valves pressurized to 100 psi is $10^{22} - 10^{23}/\text{m}^3$. Since the jet is travelling at ~ 40 km/s and the duration of the negative dip is $\delta t \sim 0.1$ μs, the thickness of the layer of neutral molecules is ~ 0.4 cm.

The presence of a cloud of neutrals in front of the jets (for shots done with gas valves pressurized to 100 psi), implies incomplete ionization of the neutrals at breakdown. The Bohm time [74, section 5.10] for the plasma is ~ 500 μs, which is much larger than the lifetime of the plasma jets. Thus the ions in the plasma jet are unable to diffuse into the neutral cloud in front of the jet.

5.3 Model

This section describes a model showing that the flow is driven by axial gradient in B_ϕ^2 associated with the slight flaring of the jet. This model is a generalization of the model presented by Bellan [75].

Consider a cylindrical coordinate system $\{r, \phi, z\}$ with the origin at the center of the electrodes and z axis along the direction of the jet flow. The jet is assumed to be axisymmetric and slightly flared. Furthermore, the poloidal flux inside the jet is assumed to have the simplest non-trivial physically relevant form

$$\psi(r,z) = \psi_\circ \frac{r^2}{a(z)^2}, \tag{5.1}$$

where

$$a(z) = a_\circ e^{\kappa z}$$

describes the flaring of the jet of radius $a(z)$. Here $a_\circ$ is the jet radius at the electrodes (refer to figure 5.1) and the constant κ is determined from flaring in figure 5.1. We assume that the pressure $P(r,z)$ vanishes at $r = a(z)$ which corresponds to assuming that B_z is nearly uniform in the jet or equivalently that the radial scale length of B_z exceeds the radial scale length for pressure. Plasma jets with a large aspect ratio (length $\gg$ radius) are assumed to be well described by equation (5.1).

Let

$$I(r,z) = I(\psi) = \frac{\lambda\psi}{\mu_\circ} = \frac{\lambda\psi_\circ}{\mu_\circ}\frac{r^2}{a(z)^2} = I_\circ \frac{r^2}{a(z)^2}, \tag{5.2}$$

where λ is a constant with dimension (length)$^{-1}$. The assumption $I = I(\psi)$ implies that current flows along flux surfaces so there is no torque ($\hat{\phi} \cdot (\mathbf{J} \times \mathbf{B})$) causing acceleration in the ϕ direction [75]. Poloidal current described by equation (5.2) implies that the axial current density J_z is independent of r.

The associated toroidal/poloidal magnetic fields and current densities are:

$$\begin{aligned}
\mathbf{B}_{\text{tor}} &= \frac{\mu_\circ I}{2\pi}\nabla\phi, \\
\mathbf{B}_{\text{pol}} &= \frac{1}{2\pi}\nabla\psi \times \nabla\phi, \\
\mathbf{J}_{\text{tor}} &= -\frac{r^2}{2\pi\mu_\circ}\nabla\cdot\left(\frac{1}{r^2}\nabla\psi\right)\nabla\phi, \\
\mathbf{J}_{\text{pol}} &= \frac{1}{2\pi}\nabla I \times \nabla\phi,
\end{aligned} \tag{5.3}$$

where $\nabla\phi = \hat{\phi}/r$. Note that a toroidal current density, $\mathbf{J}_{\text{tor}}$, will only exist if the poloidal flux function deviates from a vacuum field solution.

Due to the jet's large aspect ratio, radial equilibrium is achieved much faster than the axial equilibrium. This is evident from figure 5.1, where the radial profile of the jet hardly changes as it evolves. MHD radial pressure balance (refer to equation (1.3)) then implies

$$\begin{aligned}\frac{\partial P}{\partial r} &= \left(\mathbf{J}_{\mathrm{pol}} \times \mathbf{B}_{\mathrm{tor}}\right)_r + \left(\mathbf{J}_{\mathrm{tor}} \times \mathbf{B}_{\mathrm{pol}}\right)_r \\ &= -\frac{\mu_\circ}{(2\pi r)^2}\frac{\partial}{\partial r}\left(\frac{I^2}{2}\right) \\ &\quad -\frac{1}{(2\pi r)^2\mu_\circ}\left[r\frac{\partial}{\partial r}\left(\frac{1}{r}\frac{\partial\psi}{\partial r}\right)+\frac{\partial^2\psi}{\partial z^2}\right]\frac{\partial\psi}{\partial r}.\end{aligned}$$

Note that $\frac{1}{r}\frac{\partial\psi}{\partial r}$ = constant because of the $\psi \sim r^2$ dependence assumed in equation (5.1). This implies

$$\begin{aligned}\frac{\partial P}{\partial r} &= -\frac{\lambda^2}{(2\pi r)^2\mu_\circ}\psi\frac{\partial\psi}{\partial r} - \frac{1}{(2\pi r)^2\mu_\circ}\frac{\partial^2\psi}{\partial z^2}\frac{\partial\psi}{\partial r} \\ &= -\frac{\left(\lambda^2+4\kappa^2\right)}{(2\pi r)^2\mu_\circ}\psi\frac{\partial\psi}{\partial r}.\end{aligned} \tag{5.4}$$

Equation (5.4) can be integrated radially to give

$$P(r,z) = \frac{\left(\lambda^2+4\kappa^2\right)\psi_\circ^2}{(2\pi a)^2\mu_\circ}\left(1-\frac{r^2}{a^2}\right), \tag{5.5}$$

where the boundary condition is $P(r,z) = 0$ at $r = a(z)$.

Current and hence λ are time dependent in the experiment (see figure 3.2). However, using an average value of current $I \sim 75$ kA and applied poloidal flux $\psi_\circ \sim 4$ mWb yields a nominal value of $\lambda \sim 20\ \mathrm{m}^{-1}$. From the visual images (see figure 5.1) the flaring of the jet corresponds to $\kappa \sim 2\ \mathrm{m}^{-1}$. Thus $\lambda^2 \gg 4\kappa^2$ and hence $4\kappa^2$ can be neglected in equation (5.5). Thus, $P(r,z)$ is predominantly determined by the axial current (or equivalently the toroidal magnetic field). For such a jet, the plasma toroidal beta β_ϕ should be of order unity, as shown in figure 5.6.

The jet is in radial force balance, but there is no such balance along the z-axis. Consider the z component of the MHD equation of motion (refer to equation (1.4)) in steady-state

$$[\nabla \cdot (\rho \mathbf{u}\mathbf{u})]_z = \left(\mathbf{J}_{\text{pol}} \times \mathbf{B}_{\text{tor}}\right)_z + \left(\mathbf{J}_{\text{tor}} \times \mathbf{B}_{\text{pol}}\right)_z - \frac{\partial P}{\partial z}. \tag{5.6}$$

Using equations (5.1)-(5.3) and (5.5), equation (5.6) becomes

$$[\nabla \cdot (\rho \mathbf{u}\mathbf{u})]_z = -\frac{\partial}{\partial z}\left[\frac{\left(\lambda^2 + 4\kappa^2\right)\psi_\circ^2}{(2\pi a)^2 \mu_\circ}\left(1 - \frac{r^2}{2a^2}\right)\right]. \tag{5.7}$$

Using $\lambda^2 \gg 4\kappa^2$, equation (5.7) can be rewritten as

$$\begin{aligned}
[\nabla \cdot (\rho \mathbf{u}\mathbf{u})]_z &= -\frac{\partial}{\partial z}\left[\frac{\lambda^2 \psi_\circ^2}{(2\pi a)^2 \mu_\circ}\left(1 - \frac{r^2}{2a^2}\right)\right] \\
&= -\frac{\partial}{\partial z}\left[\frac{\mu_\circ I_\circ^2}{4\pi^2 a^2}\left(1 - \frac{r^2}{2a^2}\right)\right] \\
&= -\frac{\partial}{\partial z}\left[\frac{B_{\phi,a}^2}{\mu_\circ}\left(1 - \frac{r^2}{2a^2}\right)\right],
\end{aligned} \tag{5.8}$$

where $B_{\phi,a} = \mu_\circ I_\circ / 2\pi a$ is the toroidal magnetic field evaluated at $r = a(z)$. The plasma velocity is predominantly oriented along the z direction. So equation (5.8) can be simplified as

$$\frac{\partial}{\partial z}\left[\rho u_z^2\right] \simeq -\frac{\partial}{\partial z}\left[\frac{B_{\phi,a}^2}{\mu_\circ}\left(1 - \frac{r^2}{2a^2}\right)\right]. \tag{5.9}$$

Evaluating it at $r = 0$ gives

$$\frac{\partial}{\partial z}\left(\rho u_z^2 + \frac{B_{\phi,a}^2}{\mu_\circ}\right)_{r=0} = 0, \tag{5.10}$$

which is similar to the Bernoulli equation. Integrating equation (5.10) along the length of the jet gives

$$\left(\rho u_z^2 + \frac{B_{\phi,a}^2}{\mu_\circ}\right)_{r=0,z=0} = \left(\rho u_z^2 + \frac{B_{\phi,a}^2}{\mu_\circ}\right)_{r=0,z=L}. \tag{5.11}$$

At the electrodes ($z = 0$), $u_z \sim 0$, and $B_{\phi,a} = \mu_\circ I_\circ / 2\pi a_\circ$. Far from the electrodes ($z = L$) of the jet, $B_{\phi,a}$ is small and can be neglected. Thus the flow velocity at the jet tip can be estimated as

$$\begin{aligned} u_{r=0,z=L} &\sim \sqrt{\frac{B^2_{\phi,a_\circ}}{\rho\mu_\circ}} \\ u_{r=0,z=L} &\sim \frac{1}{2\pi a_\circ}\sqrt{\frac{\mu_\circ}{\rho}}I_\circ. \end{aligned} \tag{5.12}$$

Equation (5.6) assumed the plasma jet to be in steady-state. If the time dependent inertial term $\partial\left(\rho\mathbf{u}\right)/\partial t$ was included in the analysis, the final result of equation (5.12) could still be derived by considering dimensionless scaling of the equations. In such a case, the equations can be cast in a dimensionless form with a characteristic velocity given by equation (5.12). Also, the steady-state assumption is justified for the bulk of the plasma jet, except for the dynamic apex.

5.3.1 Comparison of the Model with Experimental Results

We now compare the experimental results to the quantitative predictions of the theory. Using the typical parameters of a hydrogen plasma jet ($n_e \sim 3\times 10^{22}/\mathrm{m}^3$, $a_\circ \sim 3-10$ cm), equation (5.12) predicts that the slope of the u vs I linear fit for hydrogen plasmas in figure 5.5 should be $0.25-0.84$ m/sA^{-1}. The experimentally observed linear dependence has a slope of 0.45 m/sA^{-1}. Equation (5.12) also suggests that the slope for the linear fits in figure 5.5 should scale inversely with the square root of the mass of ions. Thus it predicts that the ratio of slopes of the linear fits in figure 5.5 for hydrogen and deuterium plasmas should be $\sqrt{\frac{1}{2}} = 0.707$. From the experiments the ratio of slopes is measured as $\frac{0.33\pm0.03}{0.45\pm0.03} = 0.73\pm0.08$. Thus the experimentally measured value agrees reasonably well with the predicted ion mass dependence. The results clearly show that the phenomenon causing bulk plasma motion is non-equilibrium dynamics as the response of the plasma is inversely related to the square root of the ion mass.

5.4 Energy Balance for Plasma Jets

An energy balance argument for the plasma jets is presented in this section. A coaxial gun expanding against a restraining spring (see figure 5.9) is a simple analogue to the Caltech spheromak experiment. The current flowing between the outer (brown) and the

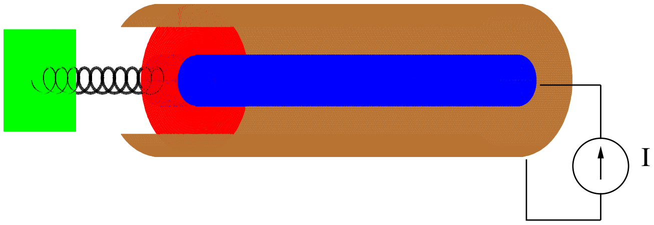

Figure 5.9: Cut out of a coaxial gun expanding against a spring.

inner (blue) conductor in figure 5.9 produces a toroidal magnetic field. The toroidal field pressure accelerates the conducting red disk outwards, thus increasing the inductance of the rail gun. Thus the toroidal field pressure acts in increasing the inductance in both the rail gun and in the Caltech spheromak experiment. As the rail gun moves outward, it deforms the spring and thus stores potential energy in the compressed spring. In the Caltech spheromak experiment, as the jet expands, it deforms the applied poloidal magnetic field there by storing energy in the stretched poloidal field $W_{\mathrm{pol}} = \int \frac{B_{\mathrm{pol}}^2}{2\mu_\circ} \mathrm{d}^3 r$.

We now consider the energy balance in the coaxial rail gun. Neglecting the resistance of the rail gun, the input energy is given by the integral of Poynting flux at the electrodes

$$W_{\mathrm{input}} = \int_0^t V I \mathrm{d}t = \int_0^t \frac{\mathrm{d}}{\mathrm{d}t} (LI)\, I \mathrm{d}t,$$

where V is the voltage appearing across the electrodes, I is the current linked by the electrodes and L is the inductance of the jet. Since the current is assumed to be constant, the input energy can be approximated as

$$W_{\mathrm{input}} = \int_0^t I^2 \frac{\mathrm{d}L}{\mathrm{d}t} \mathrm{d}t = LI^2.$$

The input energy is split into the the energy in the toroidal field, the potential energy in the spring and the kinetic energy of the disk.

$$W_{\text{input}} = \underbrace{W_{\text{tor}}}_{=\frac{1}{2}LI^2} + \underbrace{W_{\text{pot}}}_{=\frac{1}{2}kx^2} + \underbrace{W_{\text{kin}}}_{=\frac{1}{2}mv^2}\,, \tag{5.13}$$

where k is the spring constant, x is the deformation of the spring, m is the mass of the disk, and v is the velocity of the disk.

Note that the energy in the toroidal field is half of the input energy. Thus, in the absence of a restraining spring, the energy input from the current source is distributed equally into the disk's kinetic energy and the toroidal magnetic field energy in the rail gun.

However, a more physically relevant situation is when the kinetic energy term in equation (5.13) can be neglected. When the kinetic energy of the disk is negligible, the input energy is split evenly between the toroidal field energy and the spring potential energy. The kinetic energy of the rail gun can be neglected if:

1. The restraining force from the spring is almost equal to the outward force from the toroidal magnetic field pressure. The velocity gained by the disk will be negligible and the rail gun can be considered to be almost in equilibrium. The analog of this situation for the Caltech spheromak experiment is if the plasma jet were to evolve in force-free equilibrium states, thereby having equal amounts of toroidal and poloidal field energies (see [3, section 4.4.1]).

2. The mass, m, of the disk is small, and hence the kinetic energy is negligible.

We will now extend these ideas developed for the energy balance in the rail gun to the energy balance in the plasma jet. Consider an ideal plasma jet that is driven by an electrode with constant current. The energy flowing into the plasma is the time integral of the Poynting flux at the electrodes

$$W_{\text{input}} = \int_0^t VI\mathrm{d}t = \int_0^t \frac{\mathrm{d}}{\mathrm{d}t}\left(LI\right)I\mathrm{d}t + \int_0^t I^2R\mathrm{d}t,$$

where V is the voltage appearing across the electrodes, I is the current linked by the electrodes, L is the inductance of the jet, and R is the resistance of the jet. Since the current is assumed to be constant, the input energy can be approximated as

$$W_{\text{input}} = \int_0^t I^2 \frac{\mathrm{d}L}{\mathrm{d}t}\mathrm{d}t + \int_0^t I^2 R\mathrm{d}t = LI^2 + \int_0^t I^2 R\mathrm{d}t. \tag{5.14}$$

According to the definitions introduced in section 1.1.1, let W_{tor}, W_{pol}, W_{th} and W_{kin} be the energy in the toroidal magnetic field, the energy in the poloidal magnetic field, the thermal energy of the jet and the kinetic energy of the jet. The corresponding energy densities are represented by w and the appropriate subscript. Thus

$$W_{\text{tor}} = \int w_{\text{tor}}\mathrm{d}^3r, \qquad W_{\text{pol}} = \int w_{\text{pol}}\mathrm{d}^3r, \qquad W_{\text{th}} = \int w_{\text{th}}\mathrm{d}^3r, \qquad W_{\text{kin}} = \int w_{\text{kin}}\mathrm{d}^3r.$$

By conservation of energy (see equation (1.7))

$$W_{\text{input}} = W_{\text{tor}} + W_{\text{pol}} + W_{\text{th}} + W_{\text{kin}} + W_{\text{radiation-loss}}.$$

In low temperature plasmas the energy input from the resistive term in equation (5.14) is expected to be almost completely lost in line emission ($W_{\text{radiation-loss}}$) [76]. Thus, the plasma jets are expected to gain minimal thermal energy from Ohmic heating. This gives

$$LI^2 \sim W_{\text{tor}} + W_{\text{pol}} + W_{\text{th}} + W_{\text{kin}}.$$

Since, $W_{\text{tor}} = LI^2/2$, we get

$$W_{\text{pol}} + W_{\text{th}} + W_{\text{kin}} \sim W_{\text{tor}}. \tag{5.15}$$

Had the jet been force free, then $W_{\text{th}} = W_{\text{kin}} = 0$ and the energies in the toroidal and poloidal fields would have been equal [3, section 4.4.1]. However, with the non-equilibrium jets at the Caltech spheromak experiment all the quantities in equation (5.15) are positive definite. At the Caltech spheromak experiment, a strong poloidal field is applied for substantial helicity injection and also for ensuring kink stability. Thus the energies in the toroidal and poloidal magnetic fields are comparable to each other. Using equation (5.15), this implies $W_{\text{pol}} \lesssim W_{\text{tor}}$, and also that the thermal and kinetic energy content of the jet is

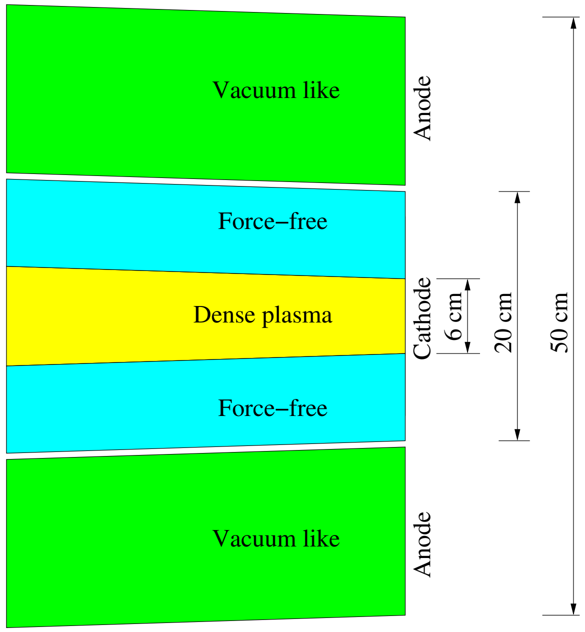

Figure 5.10: A cartoon of the jet showing three different regions of the plasma jet.

significantly less than the toroidal field energy. Equivalently

$$\begin{aligned} W_{\text{kin}} &\ll W_{\text{tor}}, \\ W_{\text{th}} &\ll W_{\text{tor}}. \end{aligned} \tag{5.16}$$

The results in sections 5.3 and 5.2 indicate that

$$w_{\text{th}} \sim w_{\text{kin}} \sim w_{\text{tor}}. \tag{5.17}$$

Equations (5.16) and (5.17) can be simultaneously satisfied only if the spatial extent of the plasma is small compared to the spatial extent of the toroidal magnetic field. This fact is validated by observation of the plasma jet radius of ∼ 3 cm in figure 5.1 and a radius of ∼ 10 cm of the toroidal field densities in figure 5.2. Even equation (5.5) predicts that the radial extent of plasma is smaller than the radius of the current channel.

These inferences can be summarized as follows:

1. The center of the jet (represented by the yellow in figure 5.10) consists of dense plasma. It has a radial extent of ∼ 3 cm.

2. Outside the central region (represented by the cyan region in figure 5.10), the plasma density is negligible. Hence this region is expected to be in a force free state described by $\mathbf{J} \times \mathbf{B} \sim 0$. The radial extent of the force free region is ~ 10 cm. The toroidal magnetic pressure in this region is comparable to the plasma thermal energy density and kinetic energy density in the plasma central region.

3. Outside the force free region, the magnetic fields are vacuum fields until the return currents to the anode are encountered. this region is represented by green in figure 5.10. The return currents are located after a radius of ~ 25 cm.

5.5 Conclusion

Alfvénic flows based on toroidal magnetic field pressure have been observed in earlier coaxial gun experiments [58]. However, this chapter shows that even in the presence of a substantial external poloidal magnetic field required for helicity injection, the plasma flow is predominantly Alfvénic with respect to the toroidal magnetic field, provided there is only a slight flare in the poloidal current channel of the plasma jet.

The following are the main results from this chapter:

1. MHD based non-equilibrium slightly flaring plasma jets are observed during helicity injection.

2. These jets emanate outwards from the electrodes towards the vacuum with Alfvénic velocities. The speeds of these jets are not based on neutral pressure gradients, but on the axial gradient in the toroidal magnetic field energy density.

3. The pressure in the jets is balanced by the toroidal magnetic field. Hence these jets have $\beta_\phi \sim 1$.

4. The radial scale for pressure in these jets is smaller than the radial extent of poloidal current or poloidal flux.

5. When the jets are formed by neutral gas fed from fast gas valves pressurized at 100 psi, then there is a layer of neutrals of density $10^{22} - 10^{23}/\mathrm{m}^3$ and thickness ~ 0.5 cm in front of the jet.

Chapter 6

X-ray Imaging System for the Caltech Solar Coronal Loop Simulation Experiment

Energetic particles and radiation have been observed in reconnecting plasmas in both laboratory [77] and extra-terrestrial plasmas [78]. The Caltech solar coronal loop simulation experiment [79] is designed to study reconnecting magnetic flux tubes and the relevant physics of solar prominences [5, 80]. This chapter focuses on characterizing the soft X-ray (SXR) and Vacuum Ultra Violet (VUV) radiation observed from the experiment.

The chapter is organized as follows. Section 6.1 describes the Caltech solar coronal loop simulation experiment. It also explains the three different modes of operation of the experiment. Section 6.2 describes the diagnostics used in the experiment. The X-ray diodes and the X-ray imaging system are described in detail in sections 6.2.1 and 6.2.2 respectively. Section 6.3 compares the various modes of operating the experiment (single prominence, co-helicity and counter-helicity merging), focusing on the production of X-ray photons. Finally, section 6.4 suggests some ideas for future research on the experiment.

6.1 Overview of the Experiment

The Caltech solar prominence simulation experiment uses the "Mark IV" electrode design, described in detail by Hansen [79], Chapter 5. The setup consists of four electrodes each with a gas injection orifice (see figure 6.1). The upper electrodes are the cathode and the lower electrodes are the anode. The electrode polarity is fixed and is usually not changed. During a plasma discharge, the electrodes are floating with respect to the chamber ground.

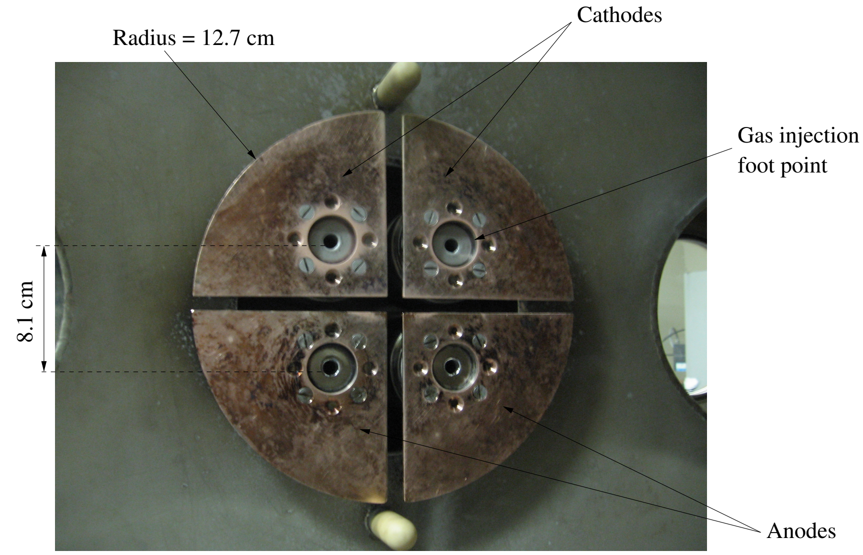

Figure 6.1: Electrodes for the dual prominence experiment.

A 59 μF capacitor bank is switched by a size A GL-7703 ignitron to achieve the plasma discharge. For all the results presented in this chapter, the capacitor was charged to 6 kV.

Four magnetic field coils of inductance $\sim 280\ \mu$H each are located behind each of the gas injection points. Each coil creates a bias magnetic field either out of the plane of the picture in figure 6.1 (represented by "North - N" in subsequent figures) or into the plane of the picture (represented by "South - S" in subsequent figures). The polarity of each magnetic field bias coil can be controlled independently. The applied magnetic field (referred to as the toroidal bias field in this chapter) is constant for the duration of experiment. The magnetic coils behind the cathode foot points are powered by an electrically isolated 9.9 mF capacitor bank and the magnetic coils behind the anode foot points are powered by another electrically isolated 9.6 mF capacitor bank. For all the measurements reported in this chapter, the magnetic field coils were discharged at 200 V, thereby creating a toroidal flux of ~ 0.2 mWb at each foot point.[1]

Neutral gas was puffed into the chamber at the gas injection foot points shown in the picture. The two orifices in the cathode were fed by a fast gas puff valve [3, chapter 14]. The two orifices behind the anode were fed by a similar gas puff valve.

The following sequence of events was followed to create a plasma discharge:

---

[1] Calibration of the toroidal flux was performed by Rory Perkins and Eve Stenson.

1. The toroidal field power supplies were triggered 4.5 ms before the plasma discharge. It takes 4.5 ms for the magnetic field to reach its maximum and link adjacent foot points on the cathode and the anode.
2. Fast gas valves were triggered 2 ms before the plasma discharge. It takes about 2 ms for neutral gas to travel from the fast gas puff valves to the orifices at the foot points. The fast gas valves were pressurized with deuterium at 100 psi for all the experiments reported in this chapter.
3. The 59 μF capacitor was discharged across the electrodes to create a plasma.
4. The various diagnostics and the digitizers were triggered upon the neutral gas breakdown near the electrodes.

The experiment can be run in the following modes:

1. Single prominence: The setup for the single prominence experiment is shown in figure 6.2. Only the left electrodes are used to create the plasma discharge. The bias toroidal field is not created at the right electrodes. Neutral gas is also not injected at the orifices in the right electrodes. As the plasma flux tube expands due to the hoop force, it kinks. The shape of the flux tube resembles the shape of a typical helical field line shown in the figure i.e., a dip is observed from the side view and a reversed "S" shape from the top view.
2. Co-helicity merging: The setup for the co-helicity merging experiment is shown in figure 6.3. Two similar magnetic flux tubes are created by each of the electrodes. Since the same amount of helicity is injected into both the flux tubes, they behave in an identical manner. For example, they have identical shapes when looked at from the top view. The plasma flux tubes expand due to the hoop force and also merge with each other due to the attraction between parallel currents.
3. Counter-helicity merging: The setup for the counter-helicity merging experiment is shown in figure 6.4. Two magnetic flux tubes are created by each of the electrodes. The toroidal bias field is in opposite direction in the flux tubes. Thus, equal but opposite amounts of helicity are injected into each of the flux tubes. Since the handedness of

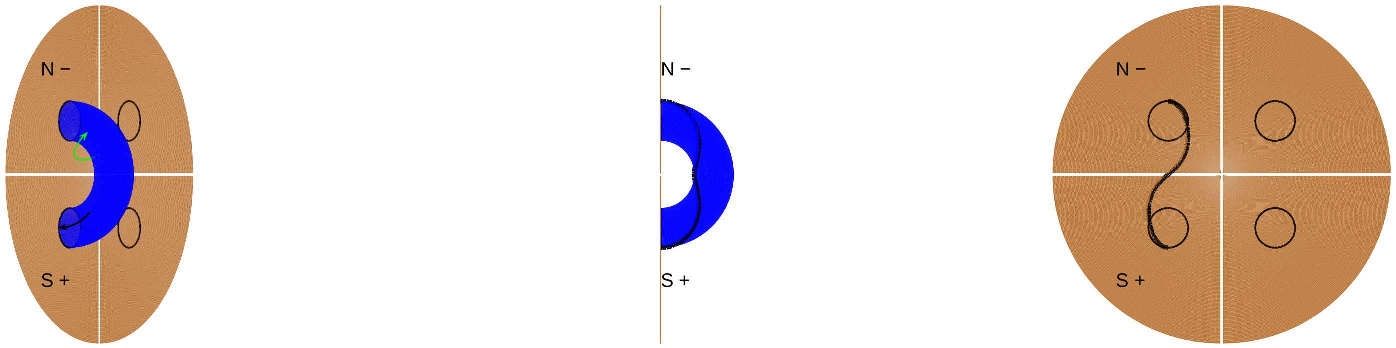

(a) Setup for single prominence.

(b) Side view.

(c) Top view.

Figure 6.2: Cartoon showing the setup of the single prominence experiment. The applied toroidal field is represented by the black arrow and the field generated by the gun current is represented by the green arrow. A representative magnetic field line is plotted in black showing the characteristic “dip” in the side view and the reversed “S” shape in the top view.

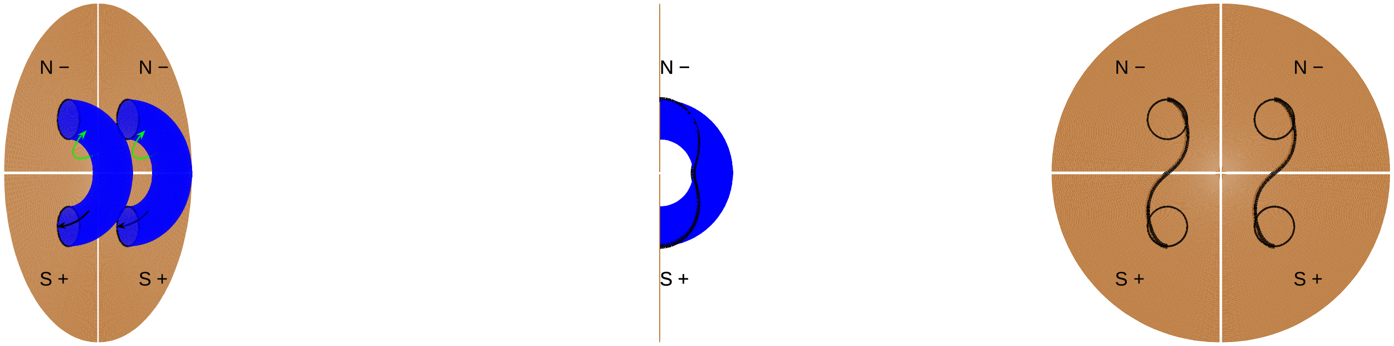

(a) Setup for co-helicity merging.

(b) Side view.

(c) Top view.

Figure 6.3: Cartoon showing the setup of the co-helicity merging experiment. The applied toroidal field is represented by the black arrow and the field generated by the gun current is represented by the green arrow. Representative magnetic field lines are plotted in black showing the characteristic “dip” in the side view and the reversed “S” shapes in the top view.

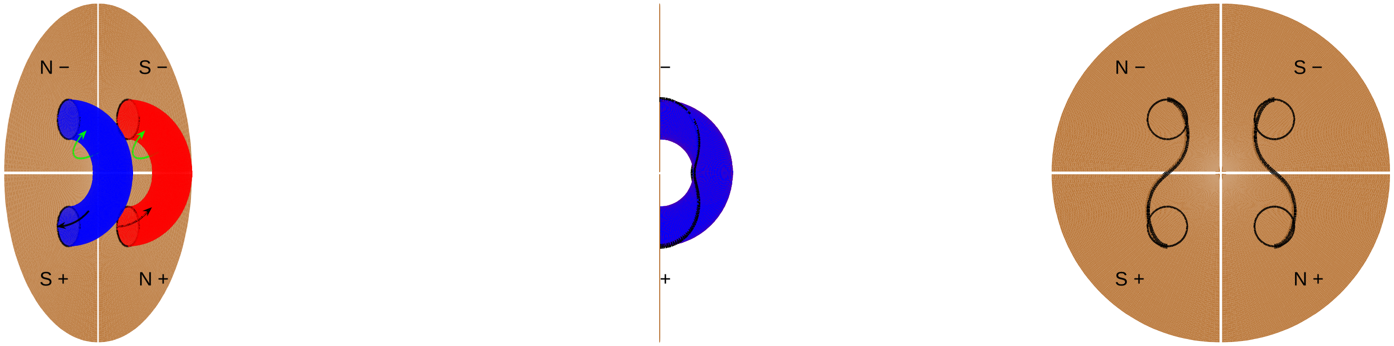

(a) Setup for counter-helicity merging.

(b) Side view.

(c) Top view.

Figure 6.4: Cartoon showing the setup of the counter-helicity merging experiment. The applied toroidal field is represented by the black arrow and the field generated by the gun current is represented by the green arrow. Representative magnetic field lines are plotted in black showing the characteristic “dip” in the side view and the “S” and reversed ”S” shapes in the top view.

the magnetic field is opposite in each of the flux tubes, an “S” and a reversed “S” shaped flux tube is observed from the top view.

The origin of the “S” and the reversed “S” shape of the plasma in the experiments can be explained in terms of a kink in the flux tube (as shown in figures 6.2, 6.3, 6.4 and explained by Rust and Kumar [81]) or by considering plasma in a Taylor state equilibrium [5].

6.2 Diagnostics

The following commercially available diagnostics were used in the experiment:

1. A Tektronix P6015 [14] high voltage probe was used to measure the potential difference across the electrodes.
2. A Rogowski coil [3, chapter 15] was used to measure the current flowing through the high voltage capacitor bank.
3. Imacon 200 - a high speed imaging camera manufactured by DRS Technologies [15] - was used to take visible images of the plasma.

In addition to the diagnostics mentioned above, two more diagnostics were upgraded for the experiment. These are described below.

6.2.1 X-ray Diodes

Four high speed X-ray sensitive diodes (Part number AXUV-HS5) manufactured by International Radiation Detectors [82] were used to diagnose the evolution of plasma-filled flux tubes in the experiment.[2] The diodes were reverse biased to 45 V, to achieve maximal efficiency and the best rise time performance (< 1 ns). The diodes are sensitive to photons with energies $\gtrsim 10$ eV, and their gain increases by $\sim 17\%$ per eV increase in photon energy.

Three out of the four diodes were covered with thin metal foil filters manufactured by Lebow Company[83]. The filters placed in front of the diodes were Ti 50 nm, Al 200 nm and Ti 500 nm. The transmission properties of the filters is plotted in figure 6.5 [84, 85].

---

[2] The mechanical assembly of the diodes and the electronics were designed by Paul Bellan.

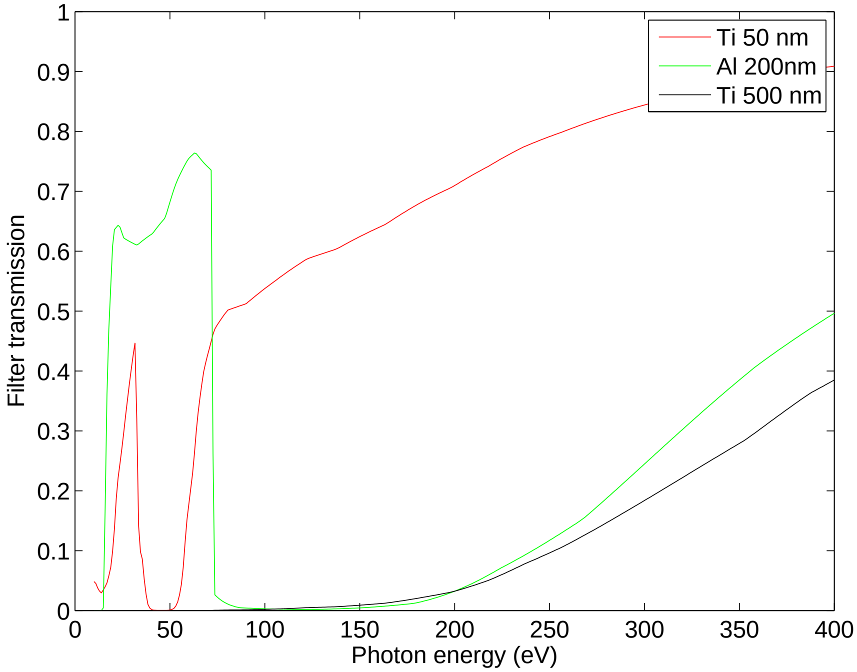

Figure 6.5: Transmission characteristics of X-ray foil filters.

It is shown in section 6.3 that no output was detected by the diode behind the Ti 500 nm filter. This shows that X-ray photons produced by the experiments have energies $\lesssim 200$ eV. To understand the energy spectrum of the photons produced in the experiment, the Ti 500 nm filter should be replaced by a filter whose bandwidth is limited to $75 - 200$ eV.

6.2.2 X-ray Imaging System

Photons in the VUV (Vacuum Ultra Violet) to SXR (Soft X-ray) band are severely attenuated by glass. Thus X-ray scintillators are usually placed so that they share the same vacuum as the main experiment, or special windows are used to ensure transmission of the photons. The X-ray diode array built by Snider et al. [86] used Beryllium vacuum windows to prevent X-ray attenuation. They also used pressurized neutral gas as an X-ray energy filter.

The VUV/SXR imaging system built for the Caltech solar coronal loop experiment was installed in vacuum. figure 6.6 shows the setup of the imaging system. A pin hole of diameter 200 μm was used in the setup. The pin hole was placed ~ 5 cm in front of the Micro Channel Plate (MCP). The position of the pinhole can be adjusted to change the

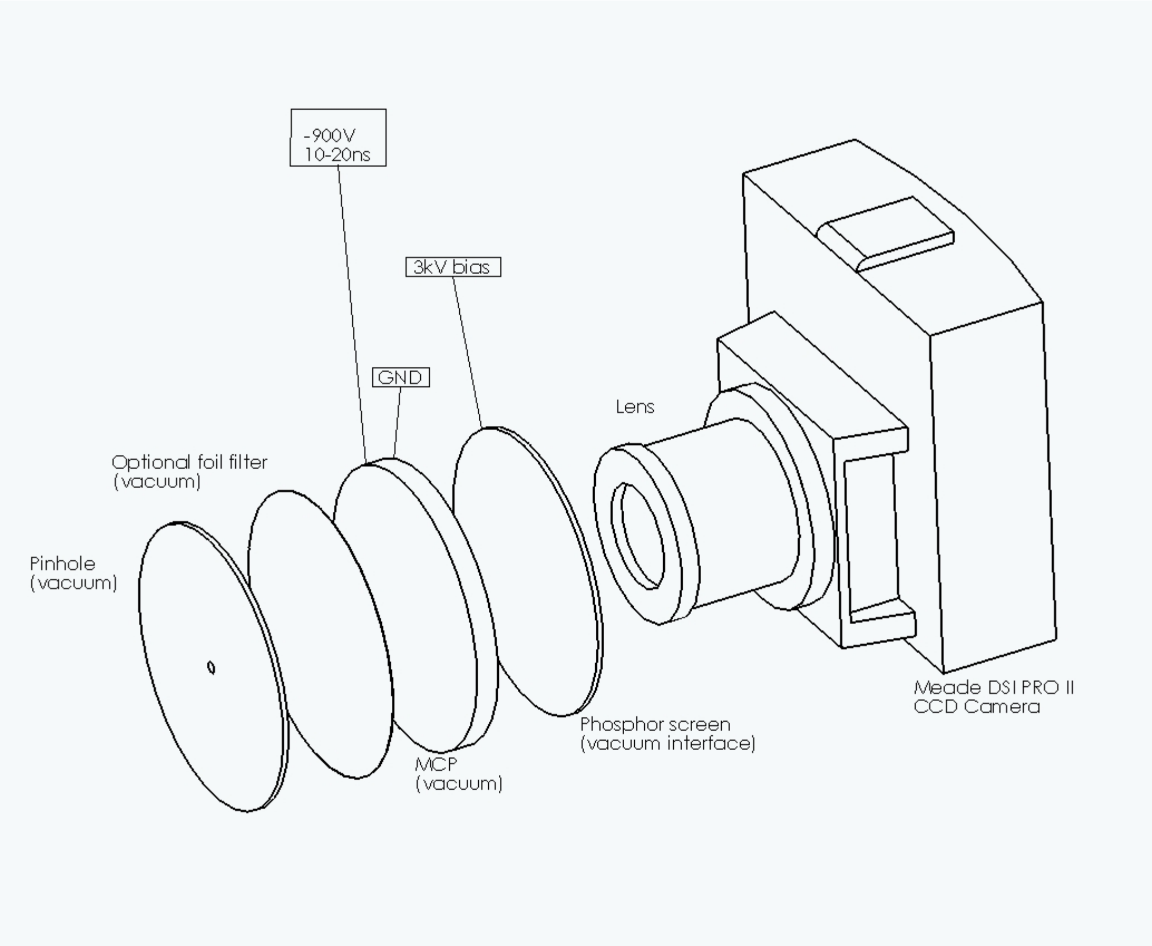

Figure 6.6: Schematic of the X-ray imaging setup.

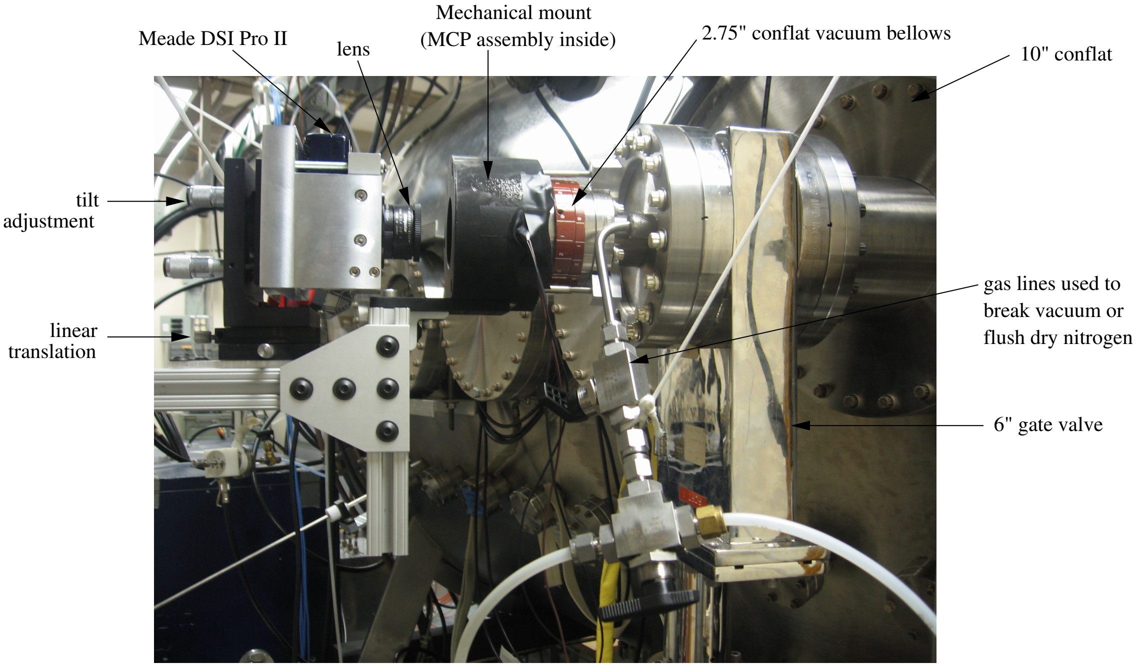

(a) Setup of the X-ray imaging camera showing parts outside the vacuum.

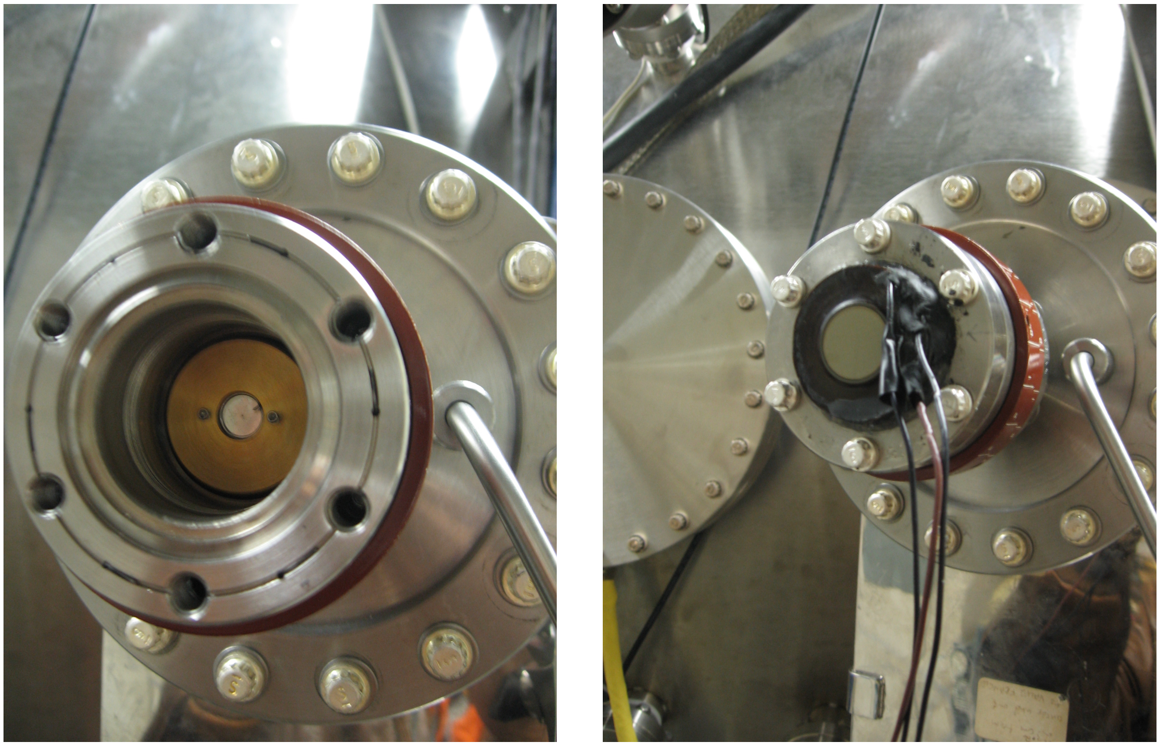

(b) Pin hole used for X-ray imaging

(c) Vacuum interface of the MCP (phosphor screen).

Figure 6.7: Setup of the X-ray imaging setup.

zoom level of the imaging system. There was no foil filter used for the images presented in this chapter. The MCP and phosphor screen assembly (Part number XUV-2018) was manufactured by X-ray and Speciality Instruments [87]. The MCP had a diameter ~ 1 inch and was coated with CsI. It was sensitive to radiation with energies $\gtrsim 6$ eV. The MCP assembly was mounted on a 2.75" conflat vacuum flange. The MCP assembly was attached to the main vacuum chamber with flexible vacuum bellows which could be tilted to change the region under view. However, the tilt was not adjusted for the results presented in this chapter.

A -900 V pulse generated by a Berkeley Nucleonics high voltage pulse generator Model 310H [88] was connected to the front end of the MCP. The pulse allowed the creation of secondary electrons by the MCP when X-ray photons were incident on it. Thus the pulse acted as an effective shutter mechanism for the imaging system. The camera was sensitive with 10 ns pulse duration, but sharper images were obtained by pulses of duration 20 ns. The pulse duration was maintained at 20 ns for all the X-ray images presented in this chapter. The electrons from the MCP were accelerated by a 3 kV DC bias applied between the phosphor screen and the MCP (see figure 6.6). The electrons caused the phosphor screen to fluorescence. The image on the phosphor screen lasted for several milliseconds (~ 50 ms) and was imaged by a Meade DSI Pro II CCD camera [89]. Data from the Meade camera was communicated to a desktop PC with a USB 2.0 cable. The Meade camera was mounted on an optical mount with tilt and linear translation capability (see figure 6.7(a)).[3]

Sample images from the X-ray imaging system are shown in section 6.3. However, the following changes may improve the X-ray imaging system:

1. The DC voltage bias to the phosphor screen was limited to 3 kV by the existing power supply. Increasing it to 5 kV will improve the contrast of the images.

2. The high voltage pulse from Berkley Nucleonics 310H was relayed to the MCP via a ~ 10 m long coaxial cable. The cable was terminated by its characteristic impedance of 50 Ω, yet the long length of the cable caused a slight resistive loss of the pulse amplitude and also altered the shape of the pulse. Moving the 310H module closer to the MCP and using a shorter cable will remove these problems and may improve the

---

[3] The mount for the Meade camera was modified from an initial design by Hyungmin Park.

contrast of the images.

3. For the images shown in this chapter, no foil filter was used in the setup (see figure 6.6). Using a foil filter may help localize the high energy radiation observed only in the counter-helicity merging experiment.

4. Different pin holes may be used in the setup of the camera. The effect of changing the pin holes on the intensity and sharpness of the images has not been investigated.

6.3 Results

The X-ray production and other differences between the three modes of the experiment have been previously studied semi-quantitatively by Hansen et al. [90]. In their work, they found:

1. Counter-helicity experiments produced significantly more X-rays than the co-helicity and single prominence experiments.

2. A bright region (the dip) at the apex of the flux tubes was observed in counter-helicity merging experiment.

The results presented in this section confirm the above observations and also offer more specific insights. The results and the dynamics of the plasma filled flux tubes for each of the three modes are described below:

1. Single prominence: It is seen from figure 6.8 that the plasma-filled flux tube expands due to the hoop force and starts writhing at ~ 1 μs. As the flux tube expands further, the plasma becomes extremely diffuse and detaches from the electrodes at ~ 2.8 μs. The voltage and current traces (figure 6.9) across the electrodes show discrete voltage jumps and current fluctuations at $\sim 3-4$ μs after breakdown. This is a characteristic of the plasma flux tube detaching from the electrodes, thereby causing a change in plasma inductance. The X-ray diode signals from the single prominence simulation experiment (figure 6.10) indicate that almost no signal is measured by the diodes with foil filters in front. Thus the radiation from the single prominence experiment is limited to $\lesssim 10$ eV. The measured radiation has a distinct temporal behavior. It

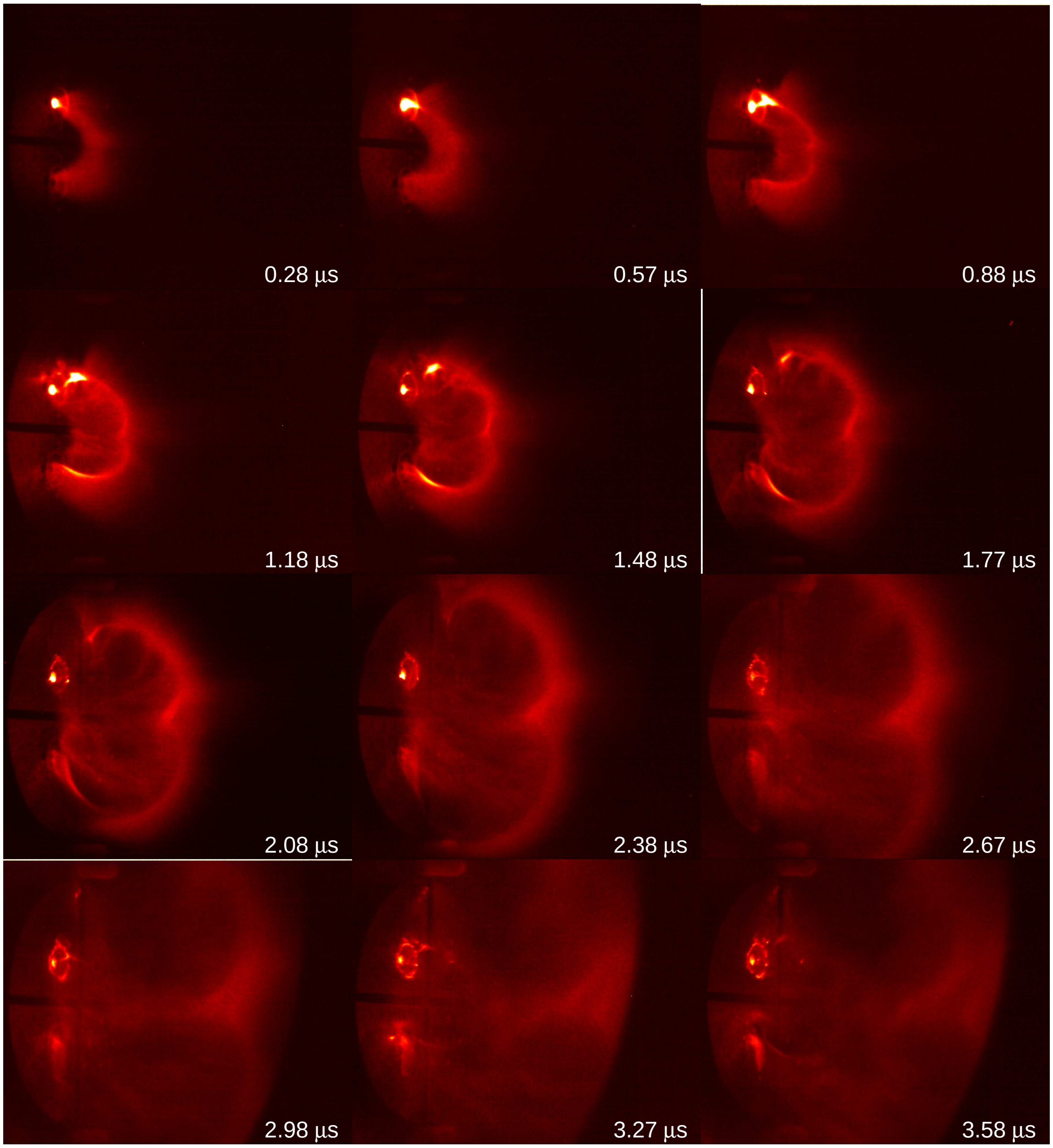

Figure 6.8: Fast camera images from single prominence simulation experiment. Visible band. Shot #6343.

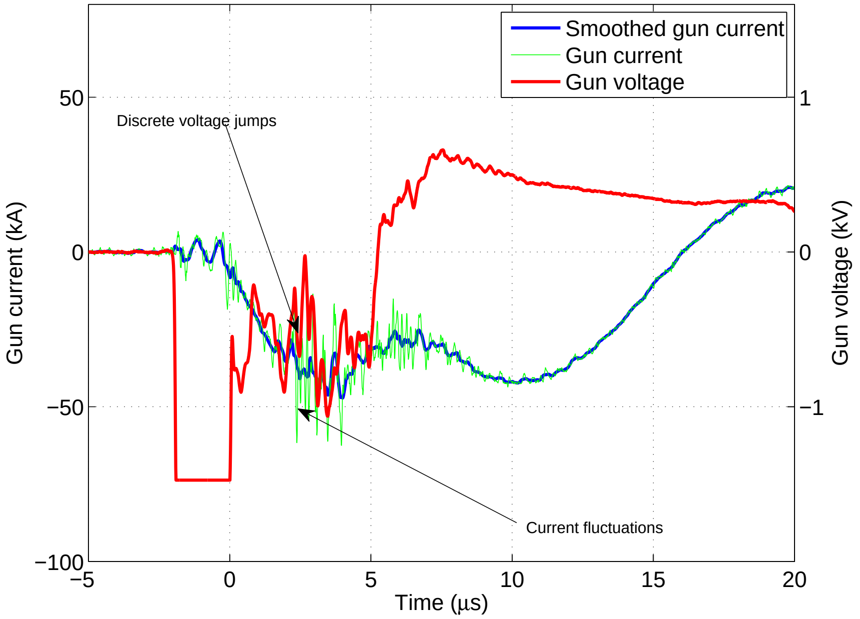

Figure 6.9: Current and voltage traces from single prominence simulation experiment. Shot # 6343.

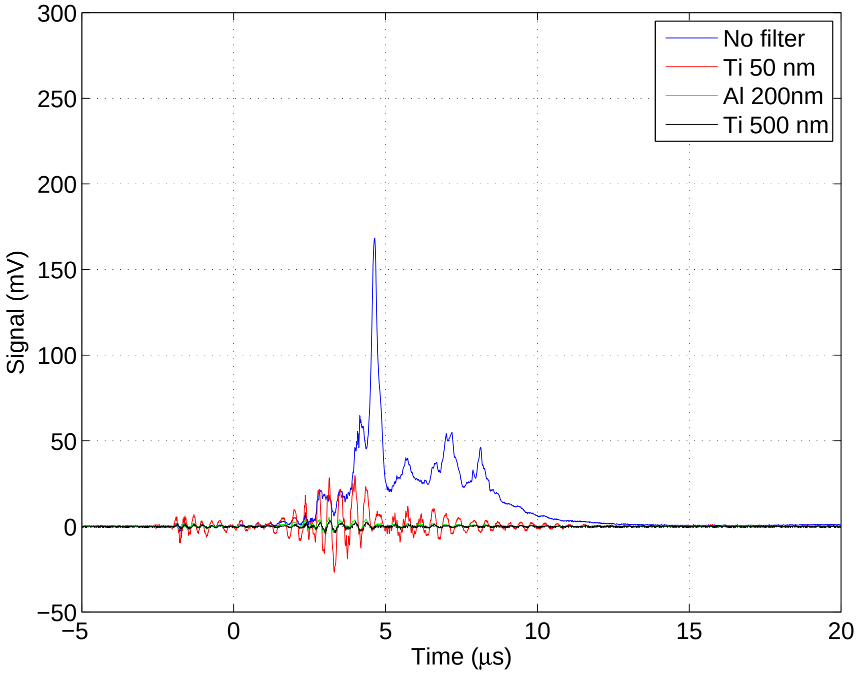

Figure 6.10: X-ray diode signals from single prominence simulation experiment. Shot #6343.

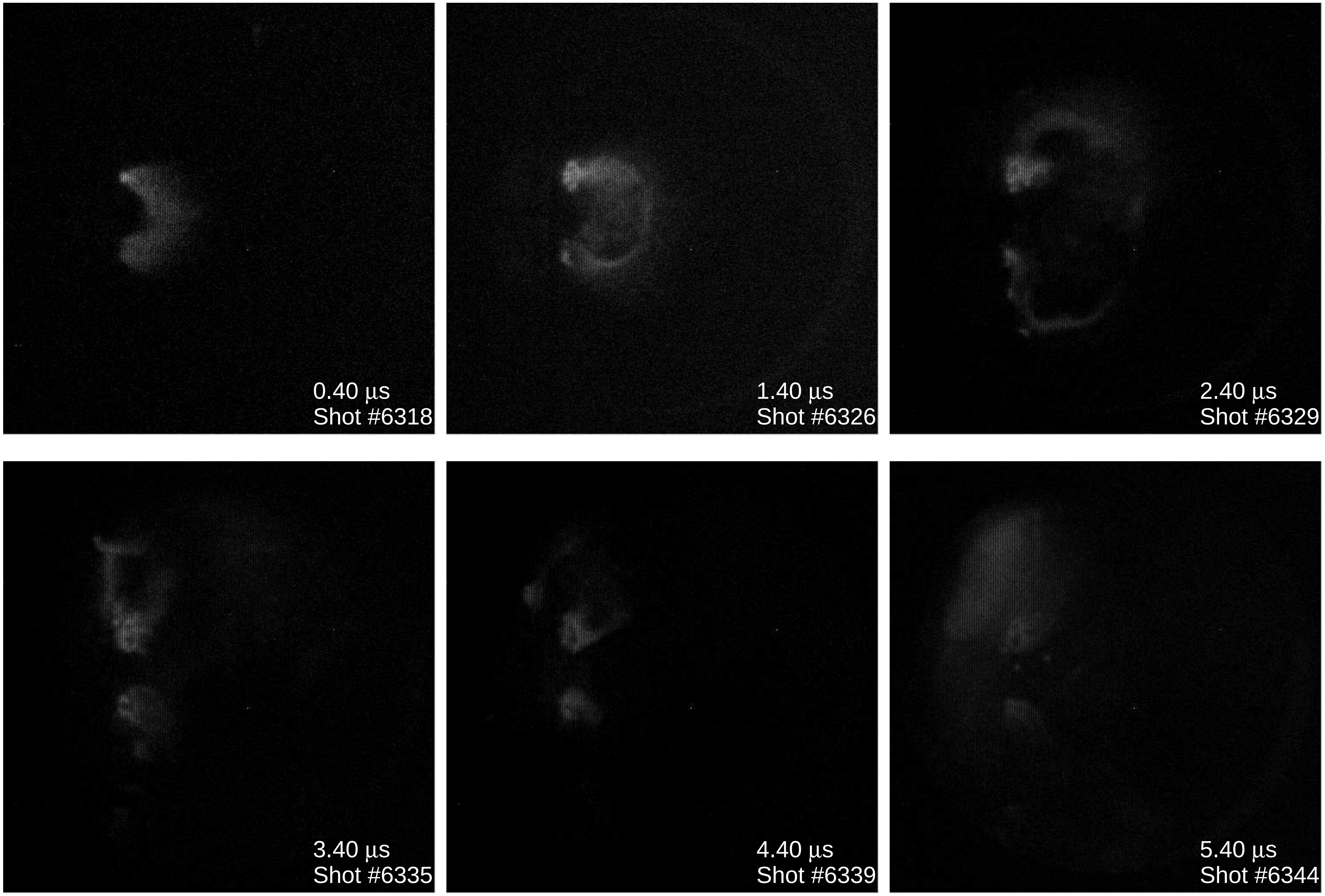

Figure 6.11: VUV/Soft X-ray images from single prominence simulation experiment.

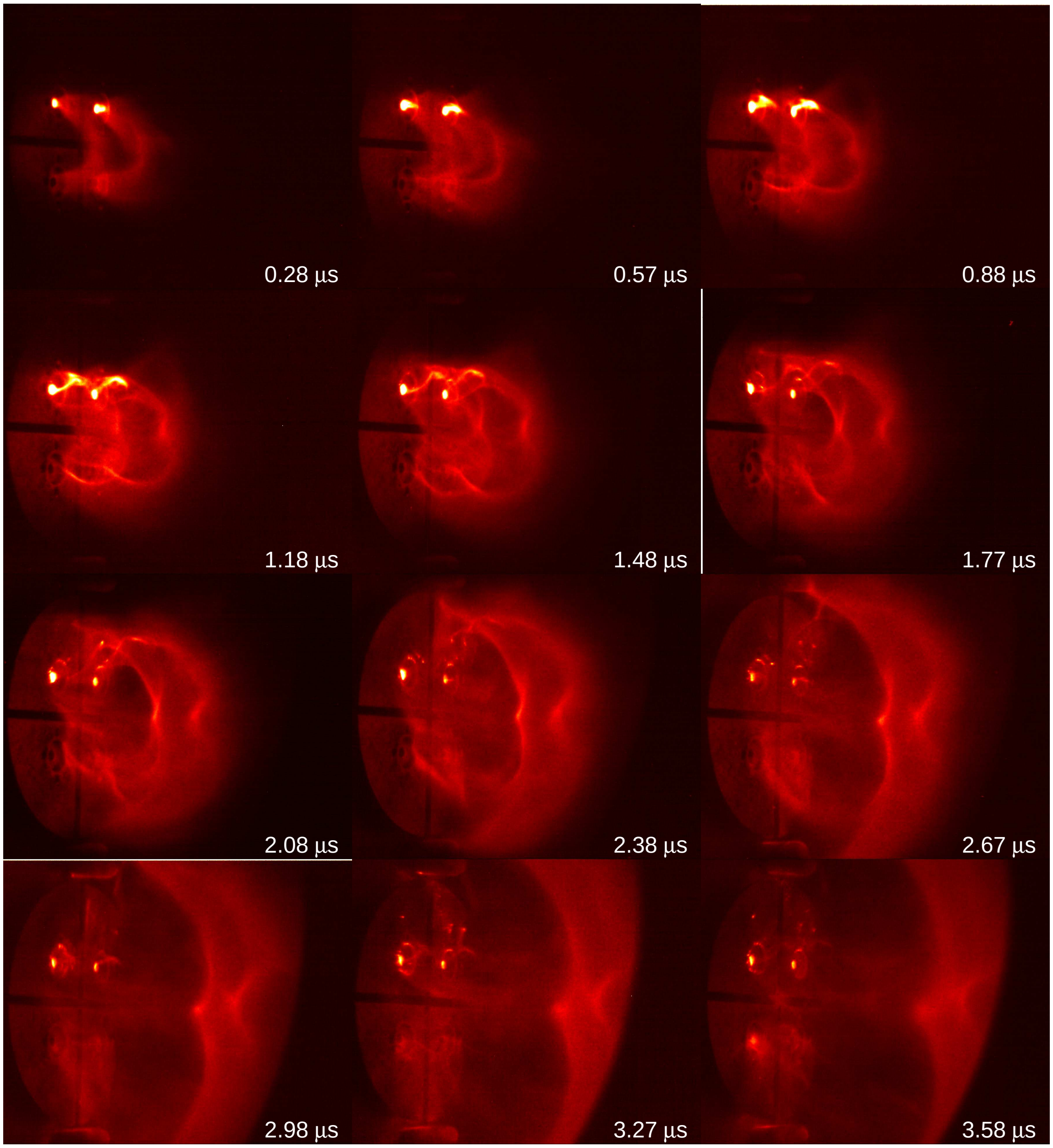

Figure 6.12: Fast camera images from co-helicity merging experiment. Visible band. Shot #6296.

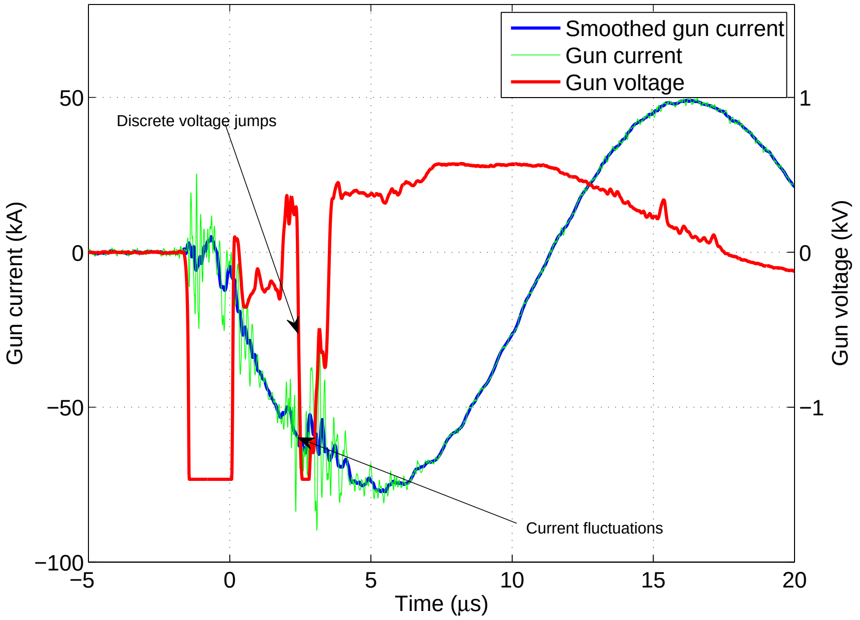

Figure 6.13: Current and voltage traces from co-helicity merging experiment. Shot #6296.

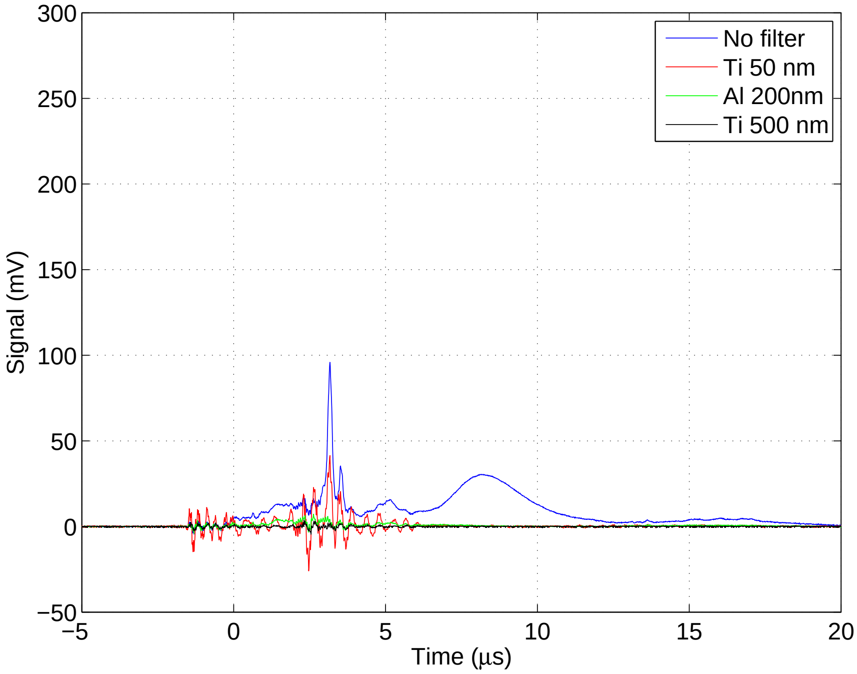

Figure 6.14: X-ray diode signals from co-helicity merging experiment. Shot #6296.

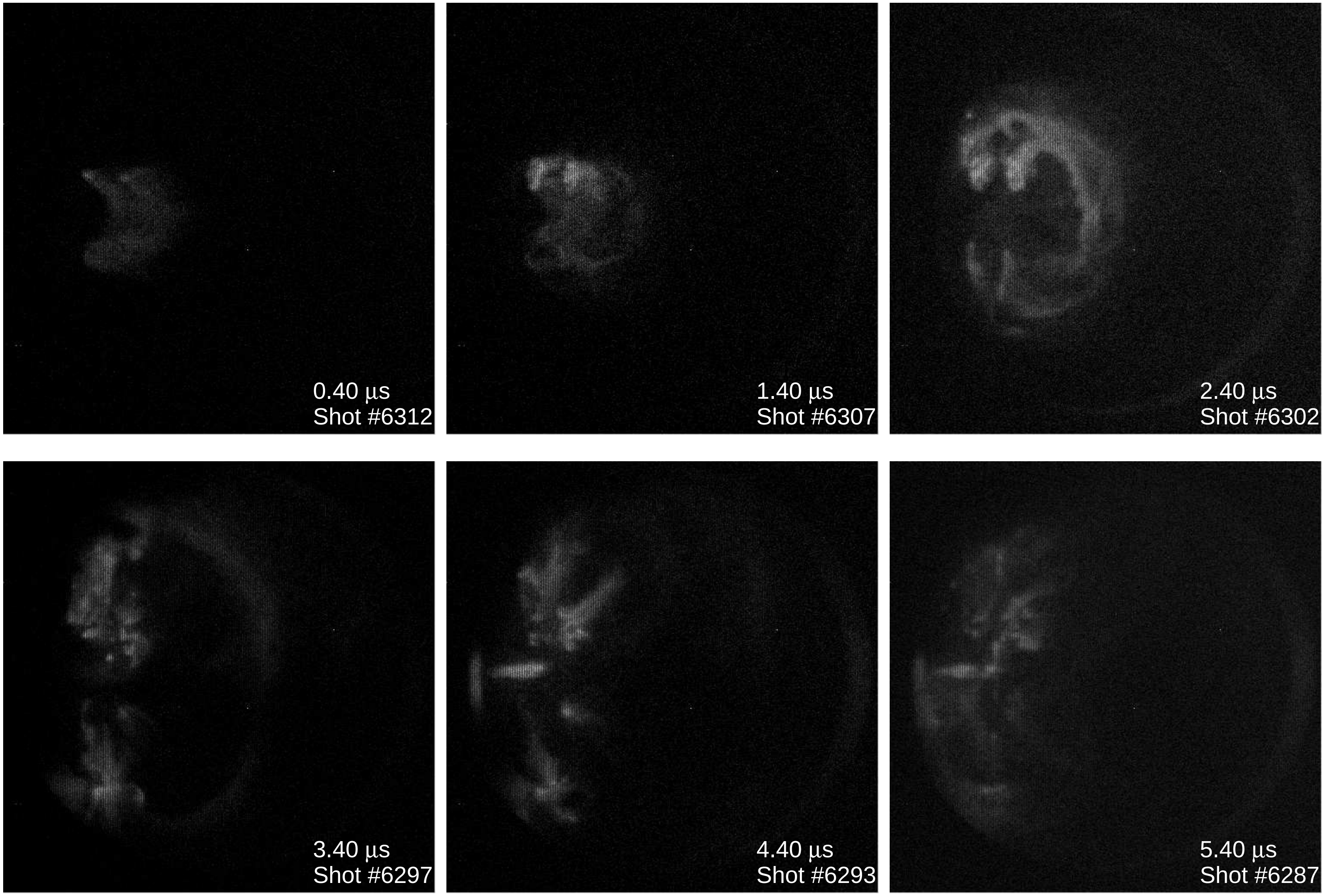

Figure 6.15: VUV/Soft X-ray images from co-helicity merging experiment.

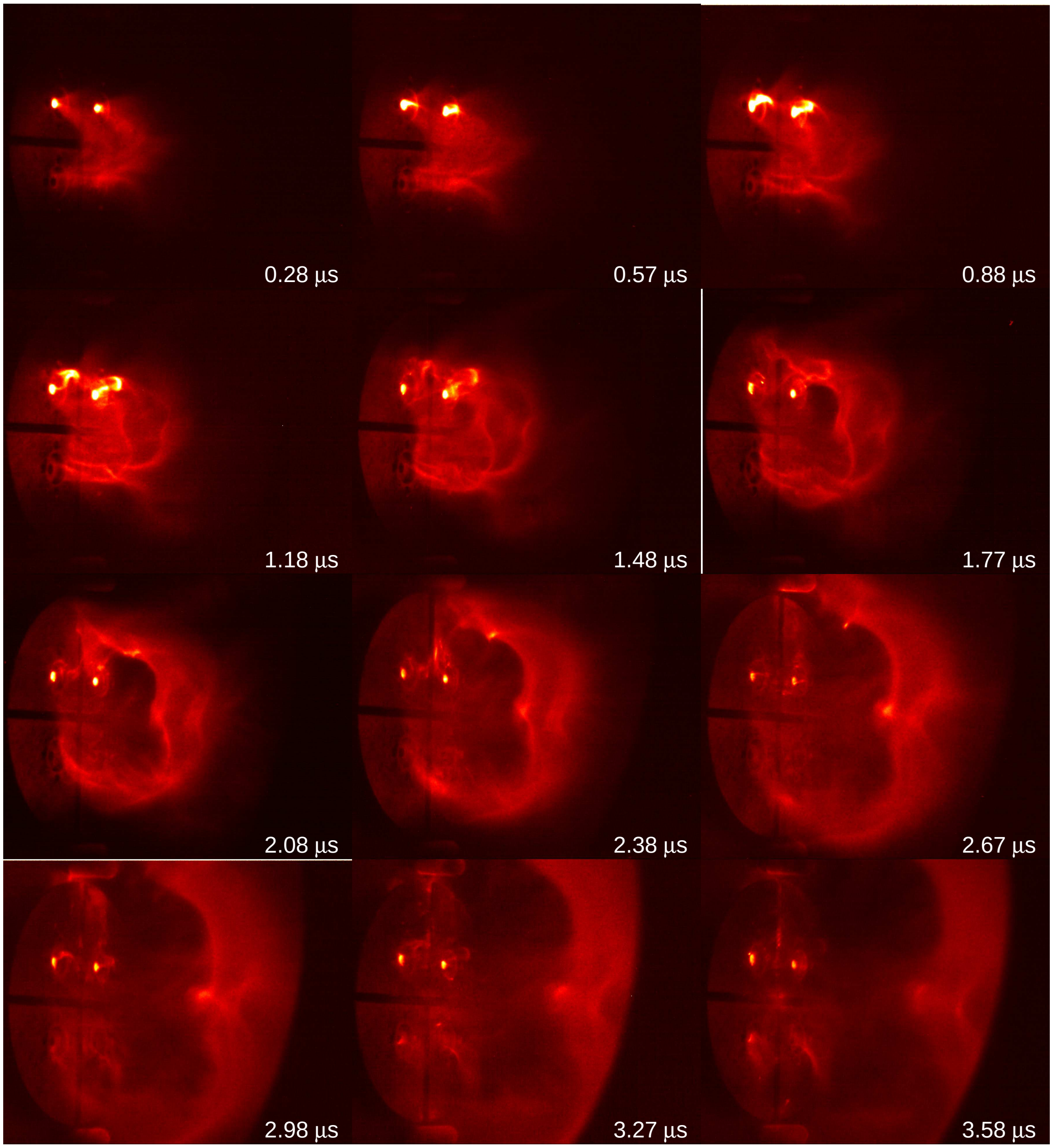

Figure 6.16: Fast camera images from counter-helicity merging experiment. Visible band. Shot #6273.

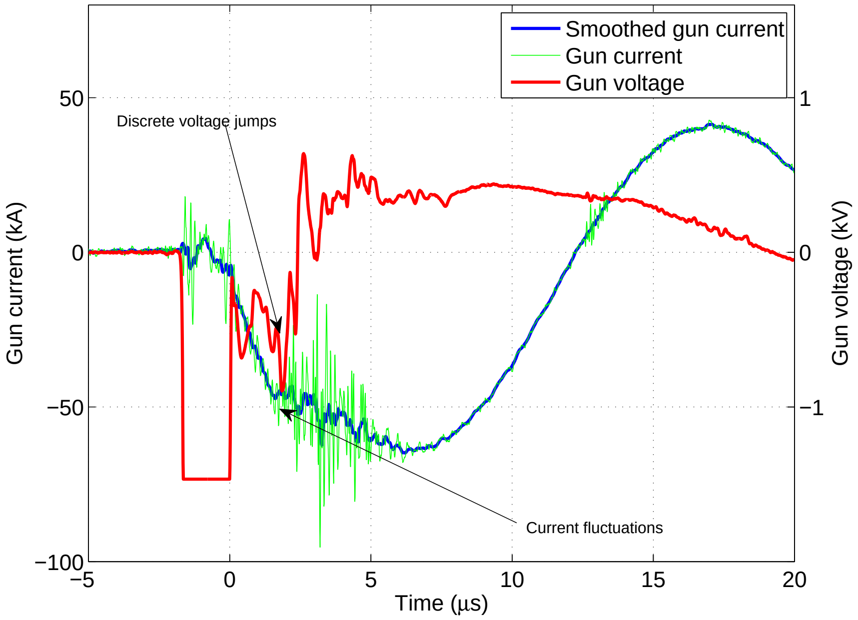

Figure 6.17: Current and voltage traces from counter-helicity merging experiment. Shot #6273.

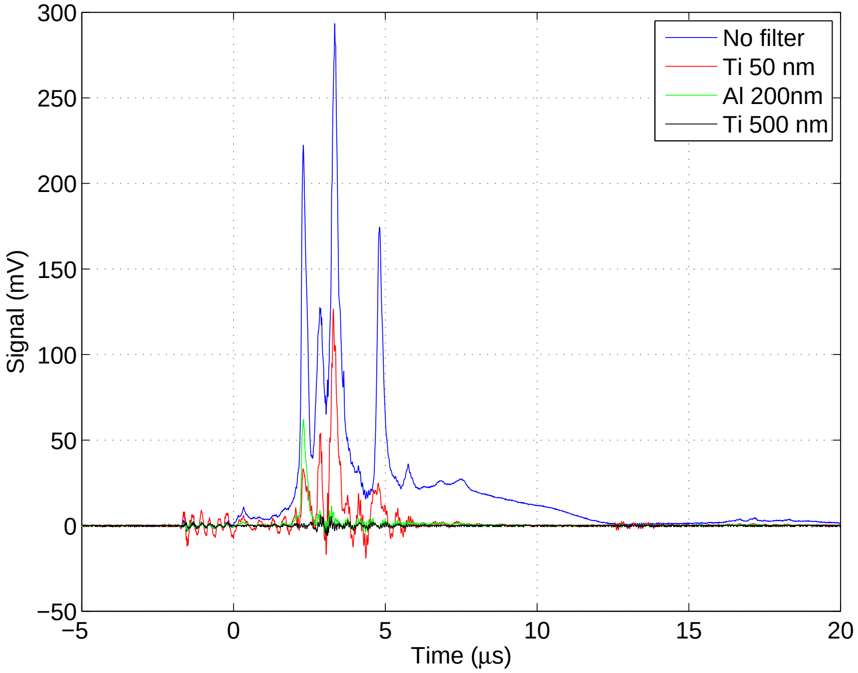

Figure 6.18: X-ray diode signals from counter-helicity merging experiment. Shot #6273.

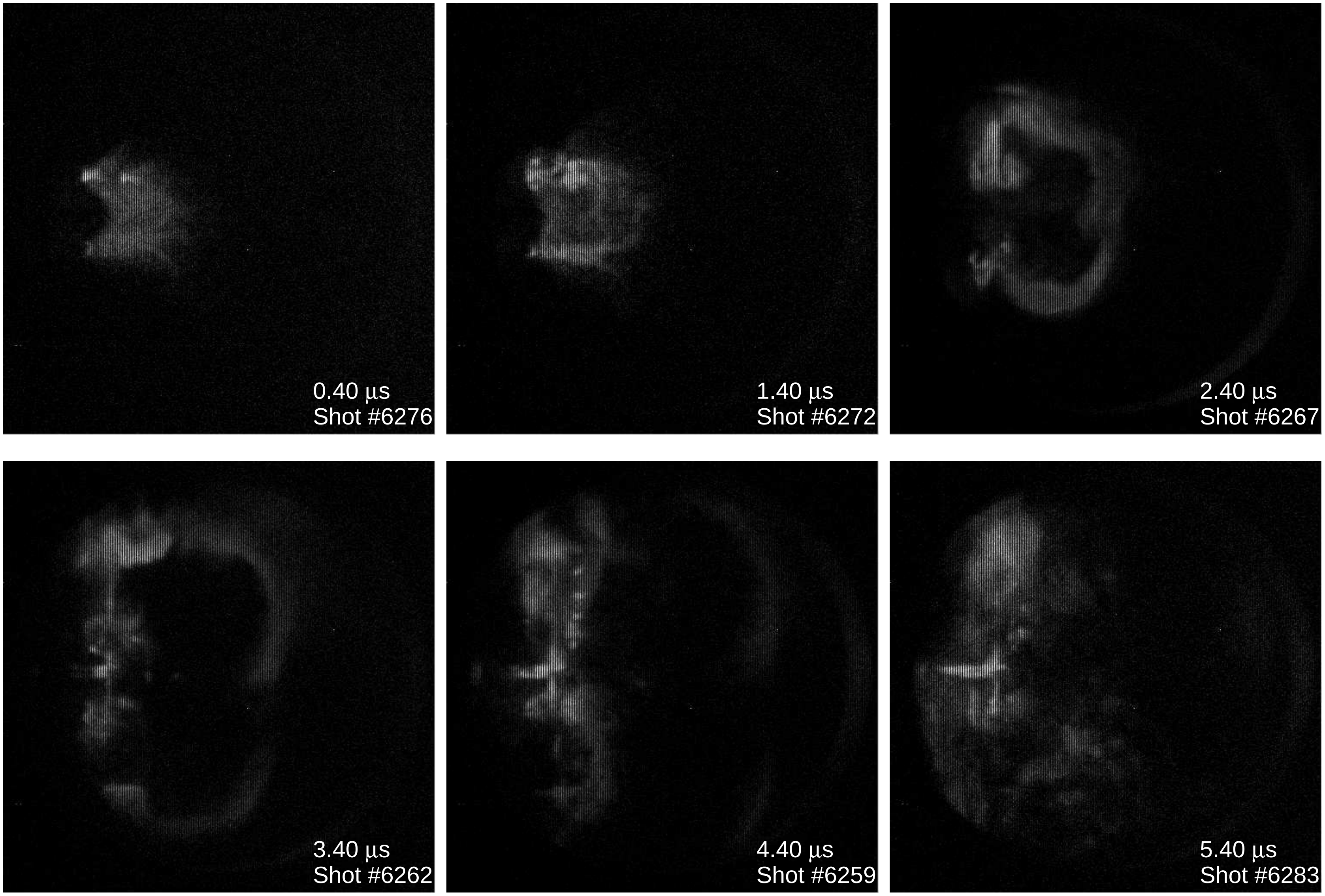

Figure 6.19: VUV/Soft X-ray images from counter-helicity merging experiment.

consists of a slowly varying background signal of $\sim 30-50$ mV along with sharp bursts of duration $\lesssim 1$ μs. These bursts usually range from $100 - 200$ mV and occur when the plasma is detaching form the electrodes (between $3.5 - 4.5$ μs after breakdown). The bursts occur at the same time as the discrete jumps are seen in the voltage across the electrodes.

The contrast of each individual VUV/SXR image from the single prominence experiment (figure 6.11) has been manually enhanced. It shows an expanding flux tube which detaches from the electrodes between $2.4 - 3.4$ μs.

2. Co-helicity: It is seen from figure 6.12 that the two plasma filled flux tubes expand due to the hoop force. They start writhing at ~ 1 μs and also tend to merge at ~ 2 μs. The slightly merged flux tubes detach from the electrodes at ~ 3 μs. The voltage and current traces (figure 6.13) across the electrodes show discrete voltage jumps and current fluctuations at $\sim 3 - 4$ μs after breakdown, indicating plasma detachment. The X-ray diode signals from the co-helicity merging experiment (figure 6.14) again indicate that the radiation from the co-helicity merging experiment is limited to $\lesssim$ 10 eV (similar to the single prominence experiment). Usually one (or sometimes two) bursts are observed in the signal from the unfiltered diode. The first burst usually occurs at ~ 3.4 μs after breakdown. As compared to the single prominence experiment, the first X-ray burst (corresponding to the plasma detachment from the electrodes) occurs slightly earlier.

   The contrast-enhanced VUV/SXR images from the co-helicity merging experiment (figure 6.15) show two distinct flux tubes until 2.4 μs after the discharge. Images from after 4 μs show bright arcing between electrodes, unlike the single prominence experiment.

3. Counter-helicity: It is seen from figure 6.16 that the two plasma filled flux tubes expand due to the hoop force. They start writhing at ~ 1 μs and also tend to merge at ~ 2 μs because of the pinch force from the parallel currents in adjacent flux tubes. The central dip at the apex of the flux tubes is brighter than the apex from the co-helicity merging experiment (figure 6.12). The voltage and current traces (figure 6.17) across the electrodes show discrete voltage jumps and current fluctuations at $\sim 3-5$ μs

after breakdown, indicating plasma detachment. The X-ray diode signals from the counter-helicity merging experiment (figure 6.18) are significantly different from the signals from co-helicity merging experiment. Usually $3-4$ bursts are observed in the X-ray diode signals, compared to just one in the co-helicity experiment. Compared to the co-helicity experiment, these bursts are higher in magnitude ($100-700$ mV). The sharp peaks in the Ti 50 nm and Al 200 nm traces in figure 6.18 indicate that the the photon energies are up to ~ 75 eV, which is considerably higher than photon energies in the co-helicity merging experiment. Also, the first burst in the X-ray diode signal is usually 3 μs after the breakdown, which is approximately $0.3-0.4$ μs before the first burst observed in the co-helicity merging experiment. This indicates that the merged flux tubes in the counter-helicity experiment tend to go kink unstable and detach from the electrodes earlier than the corresponding merged flux tubes in the co-helicity experiment.

The contrast-enhanced VUV/SXR images from the counter-helicity merging experiment (figure 6.19) are also significantly different than the images from the co-helicity experiment (figure 6.15). Comparing the images at 2.4 μs indicates that the flux tubes have already merged in the counter-helicity experiment and are still distinct in the co-helicity experiment. The intensity of the radiation from the bulk of the flux tubes in the counter-helicity experiment is also greater than the radiation observed from the co-helicity experiment. When the merged flux tubes detach from the electrodes (images at 2.4 and 3.4 μs in figure 6.19), an intense spot is observed near the cathodes. Such a bright region is not observed in the co-helicity experiment.

6.3.1 Interpretation

There are two distinct reconnection events in the co- and counter-helicity merging experiments. The first is when the adjacent flux tubes merge, and the second is when the flux tubes detach from the electrodes.

During the merging of the flux tubes in the counter-helicity experiment, the oppositely directed toroidal magnetic fields in adjacent flux tubes are annihilated. The annihilation of the toroidal field releases more energy than the merging of the flux tubes in the co-helicity experiment. Thus the bulk plasma is brighter in the counter-helicity experiment than in the co-helicity experiment. Since the bulk plasma mostly radiates in the VUV range, the radiation is most likely from line emission. This can be investigated by VUV spectroscopy.

Annihilation of the toroidal magnetic field also makes the flux tube in counter-helicity experiment more susceptible to kink instability. Thus the merged flux tube in the counter helicity experiment goes unstable and detaches from the electrode before the corresponding flux tube in the co-helicity experiment. The reason why the detachment leads to significantly higher energy photons in the counter-helicity experiment than in the co-helicity experiment is still unclear. The bursts in X-rays from the counter-helicity experiment are in a significantly higher energy band (up to 80 eV) and might be Bremsstrahlung.

6.4 Future Work

The results presented in this chapter provided some insight into the dynamics of flux tube merging in the experiment and the production of high energy photons. The following steps are suggested to further enhance the understanding of the experiments:

1. The gas orifice foot points at the cathode are much brighter than the anode foot points. This can be seen in all the visual and X-ray images from section 6.3. It is certainly a non-MHD effect, and the spectra of the emitted photons should be diagnosed using different energy filters.

2. The X-ray images from the counter-helicity experiment were taken at 1 μs intervals (see figure 6.19). Images should be taken at much more frequent intervals and with different foil filters to help understand the origin and spectra of the X-ray bursts.

3. The application of an external strapping field [80] will inhibit the detachment of the flux tubes from the electrodes. Such a scenario will be beneficial to focus only on the reconnection of the adjacent flux tubes before they detach from the electrodes.

4. The bursts of X-rays from the experiment corresponded to the flux tubes detaching from the electrodes. However, such bursts were absent when the kinked plasma jets detached from the spheromak electrodes (see chapter 5). The reason for this is not understood.

Chapter 7

Summary

Chapter 1 described the concept of spheromaks as viable magnetic fusion reactors. Spheromaks rely on the conservation of magnetic helicity as plasmas relax to an equilibrium state. Chapter 2 considered the problem of sustaining magnetic helicity in a steady state driven spheromak. It was shown that resistive MHD equilibrium is not possible when a plasma has closed flux surfaces and thus a true equilibrium is not possible in a driven spheromak. Furthermore, it was shown that a time dependent change of open flux to closed flux is essential to maintain helicity in a spheromak in quasi equilibrium.

Chapter 3 described the discharge circuit of the Caltech spheromak experiment. Various resistances and inductances in the discharge circuit were found, and it was shown that the inductance and resistance of the ignitron are the most dominant. It was also shown that the discharge circuit was an under damped current source with low energy coupling efficiency.

A homodyne and a heterodyne interferometer were built to measure the plasma density in the Caltech spheromak experiment. These interferometers were described in chapter 4. The heterodyne interferometer had about a factor of two better signal to noise ratio as compared to the homodyne interferometer, and was also much easier to align. It measured typical line-average densities of $\sim 10^{21}/\mathrm{m}^2$ with an error of $\sim 10^{19}/\mathrm{m}^2$. Chapter 4 also showed that the phase auto correlation function of a laser is periodic in length. Thus the traditionally assumed requirement of keeping the path lengths equal in an interferometer is not necessary. This fact was utilized to simplify the design of both the homodyne and the heterodyne interferometers.

The planar electrode structure of the Caltech spheromak provides an excellent opportunity to study the dynamics of magnetic helicity injection. Strong collimated jets have been observed previously in the experiment. The density and velocity measurements from these jets were described in detail in chapter 5. These flows are generated by by MHD forces because of the slight flaring of the plasma jet. The flow velocity was found to be Alfvénic with respect to the toroidal magnetic field. Also, the thermal pressure in the jets was balance by the toroidal magnetic field energy density.

The design of a VUV/SXR imaging system for the Caltech solar coronal loop simulation experiment was described in chapter 6. It was found that the bright energetic photons were radiated when the plasma flux tube detached from the electrodes. In the counter-helicity experiment, the detachment caused the plasma flux tube near the electrodes to be be extremely bright in the VUV/SXR images. In general, the plasma flux tubes from the counter-helicity experiment were found to be brighter in VUV/SXR range, and also more susceptible to being kink unstable.

Appendix A

Alignment of the Interferometers

The appendix describes the alignment procedure of the two interferometers. Section A.1 describes in detail certain critical procedures in the alignment process. Sections A.2 and A.3 describes the steps in aligning the homodyne and heterodyne interferometers respectively.

A.1 Alignment Techniques

This section describes in detail certain techniques to align the interferometers described earlier. The techniques described in this section were motivated by the work of Galvez [91].

A.1.1 Ensuring a Constant Height of the Beam Above the Optical Table

The first and the most critical step in aligning the interferometers is to ensure that the beam coming out of the laser is parallel to the optical table. The height of the beam was chosen to be the height of the detector. The technique for adjusting the laser for a parallel beam is shown in figure A.1.

The desired height of the beam was marked on the screen. The screen was then placed close to the laser at position #1 (see figure A.1). The laser mount was adjusted to change

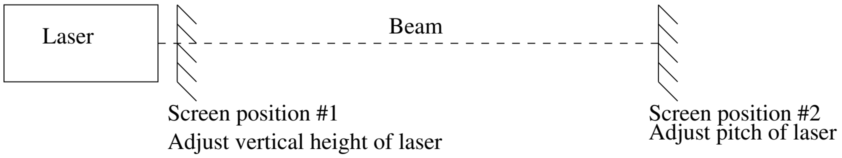

Figure A.1: Adjusting a laser to align the beam parallel to the optical table.

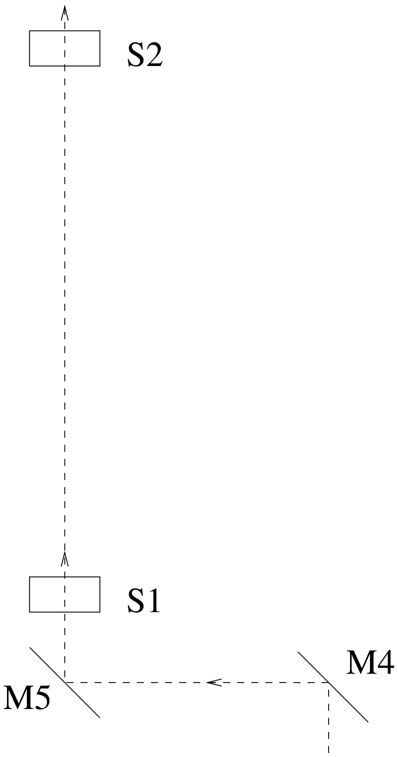

Figure A.2: Adjusting the scene beam of the heterodyne interferometer to pass through the sapphire windows.

the height of the laser so that the beam struck the screen at the desired height. The screen was then placed at a long distance from the laser (position #2). The pitch of the laser was adjusted to ensure that the beam struck the screen again at the desired height. The whole process was repeated a few times to align the beam parallel to the optical table.

A.1.2 Steering the Heterodyne Interferometer's Scene Beam through Sapphire Windows

Figure A.2 shows the arrangement used to steer the scene beam through the sapphire windows for the heterodyne interferometer (see figure 4.6). Mirror M5 is located directly below and in close proximity to the lower sapphire window S1. The first step involved adjusting mirror M4 to ensure that the scene beam was reflected by M5 to the approximate center of S1. For the second step, M5 was adjusted to steer the beam through the lower sapphire window to the approximate center of the upper sapphire window S2. The two

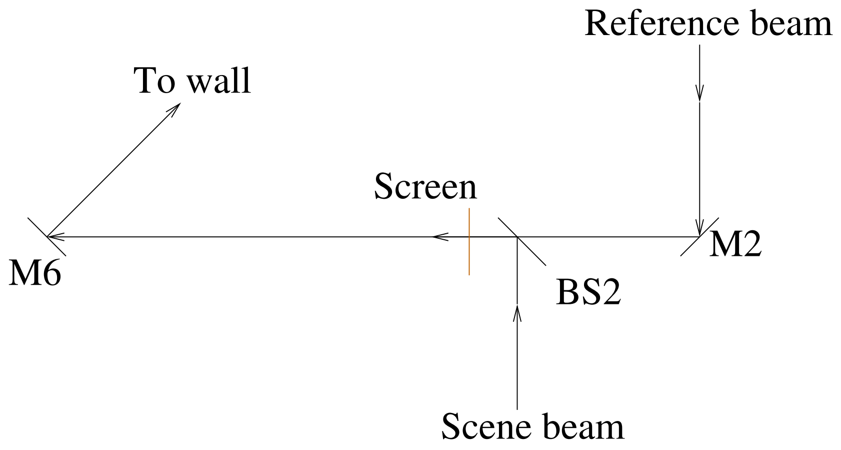

Figure A.3: Alignment for the overlap of the scene and reference beams of the heterodyne interferometer.

steps were repeated iteratively. If, however, the beam was obstructed by the chamber walls during the second step, then the alignment process was restarted at the first step.

A.1.3 Combining the Scene and Reference Beams of the Heterodyne Interferometer

As discussed in point 3 of section 4.5.4, the requirements for the overlap of the scene and the reference beams for the heterodyne interferometer are very challenging. The alignment procedure for overlapping the two beams is shown in figure A.3. For the first step, the screen was placed next to the cube beam splitter BS2, and the mirror M2 was adjusted so that the beam spots from the scene and reference beams overlapped on the screen. For the second step, the screen was removed and the mirror M6 was used to steer the beams to a distant wall a few meters away. Next, BS2 was adjusted to ensure that the beam spots from the scene and reference beams overlapped on the distant wall. The steps were repeated until a perfect overlap was achieved.

A.2 Alignment Procedure for the Homodyne Interferometer

Figure A.4 shows the arrangement of the various optical components of the heterodyne interferometer on the optical bench. The homodyne interferometer for the Caltech spheromak experiment was aligned by the following sequence of techniques (refer to figure 4.4):

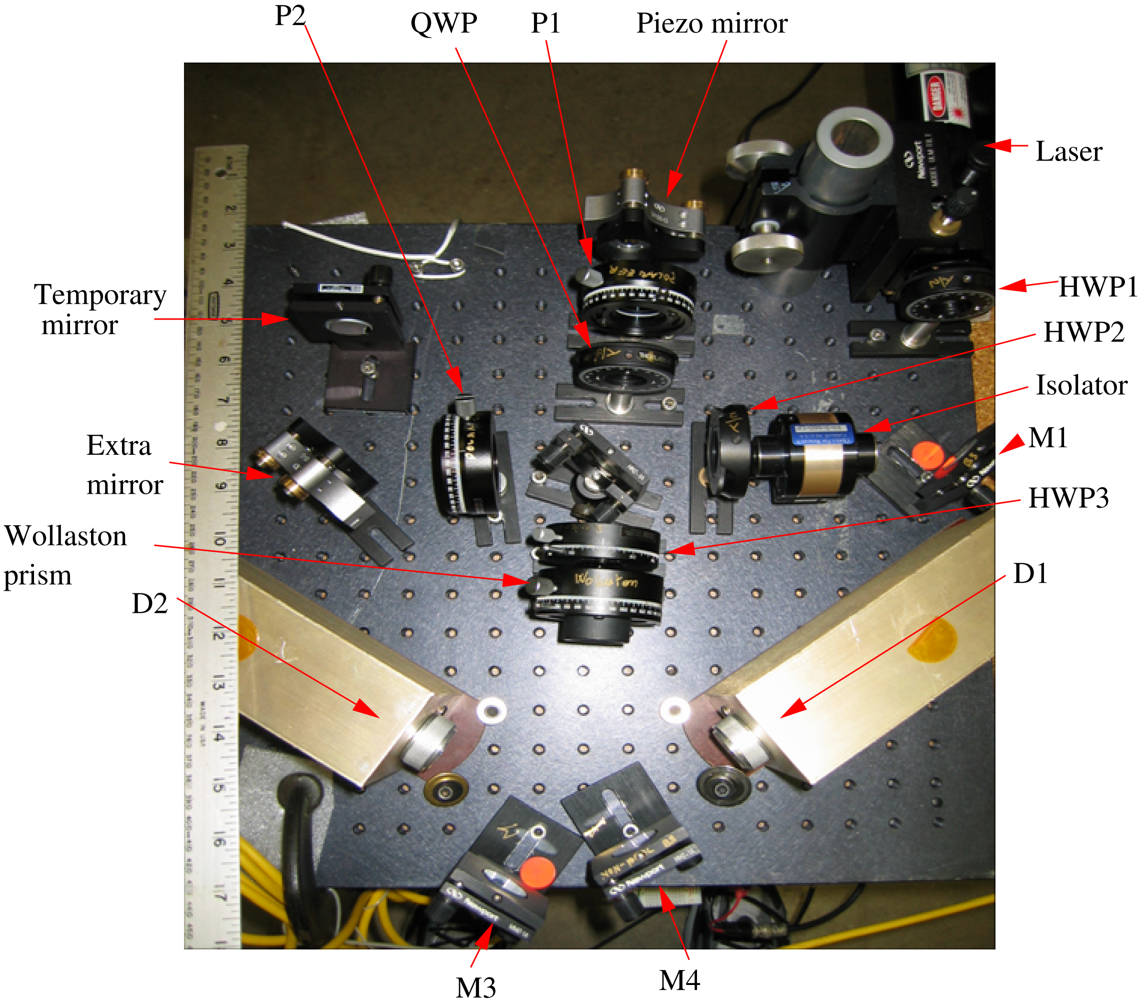

Figure A.4: Image of the 18” × 18” optical table showing the various optical components of the homodyne interferometer.

1. The laser beam was set up to be parallel to the optical table.

2. Half wave plate HWP1 was oriented to set the polarization of the laser beam to be either vertical or horizontal. Vertically or horizontally polarized light is desired because such a polarization is unaltered by reflections. A Wollaston prism can be used to check if the beam is horizontally or vertically polarized.

3. The mirror M1 was adjusted to align the beam approximately parallel to the grid on the optical table.

4. The two polarizers on the ends of the isolator were adjusted as per the manufacturer's specification to ensure near perfect isolation of the laser beam.

5. The isolator was placed to intercept the beam. The isolator was rotated about its post and the mirror M1 was adjusted to ensure that the beam at the output of the isolator was strongest and unobstructed.

6. The polarization vector of the light coming out of the isolator is rotated. The half wave plate HWP2 was adjusted to again polarize the laser beam either horizontally or vertically.

7. The non polarizing beam splitter was adjusted so that the split beams propagated almost orthogonally. The tilt of the beam splitter was adjusted so that the scene beam was parallel to the ground and hits the mirror M2 at the bottom of the chamber.

8. The piezo vibrating mirror was placed and adjusted so that the reflected reference beam follows the path of the incoming beam. It was helpful to ensure that the beam spots were coinciding on HWP2.

9. The optical axis of P1 was aligned vertically. The optical axis of the QWP was adjusted to make a 45° angle with P1's axis. The axis of P1 was found by noting that when the axis was horizontal, P1 would completely obstruct an incident vertically polarized beam. Also, the optical axis of any wave plate can be found by noting that if the wave plate intercepts a linearly polarized beam with the polarization angle along the optical axis of the wave plate, then the polarization of the beam is unaffected.

10. The second polarizer P2 was placed in the scene beam's path with its optical axis vertical.

11. It was advantageous to align the whole interferometer on the optical bench before worrying about the passage of the beam through the plasma. A mirror was temporarily placed on the optical bench to intercept the scene beam's path after P2. The path lengths of the scene and reference beams were maintained to be approximately equal. The temporary mirror was adjusted so that the reflected beam traces the incoming beam's path. Again, it was helpful to align the spots on HWP2.

12. The beams on the other end of the beam splitter must be perfectly combined. The beams were steered to a distant screen. When perfectly aligned, the beam spots on the screen were still overlapping. If not, the piezo mirror and/or the extra mirror placed in the previous step were adjusted.

13. Once perfectly aligned, the circularly polarized reference beam and will be interfered with the vertically polarized scene beam.

14. As discussed after equation (4.12), if the polarization angle of the linearly polarized beam makes an angle of 45° with the geometric axis of the Wollaston prism, the output of the two detectors will be almost equal in magnitude. To achieve this, another half wave plate HWP3 was placed in the path of the interfering beams, with the optical axis of the wave plate making an angle of $22\frac{1}{2}^\circ$ with the vertical direction. Note that HWP3 does not effect the circularly polarized beam.

15. The Wollaston prism was placed in the path of the interfering beams after the half wave plate.

16. An optical post was mounted at the likely position of each detector (D1 and D2). The mirrors M3 and M4 were adjusted so that the beams strike the center of the posts at a height equal to the height of the detectors. The piezo mirror was vibrated at ~ 1 Hz, and visible fringes were observed on the posts.

17. The posts were replaced by the detectors. The piezo mirror was vibrated at a frequency of ~ 1 kHz and the signals from the detectors were monitored on the oscilloscope.

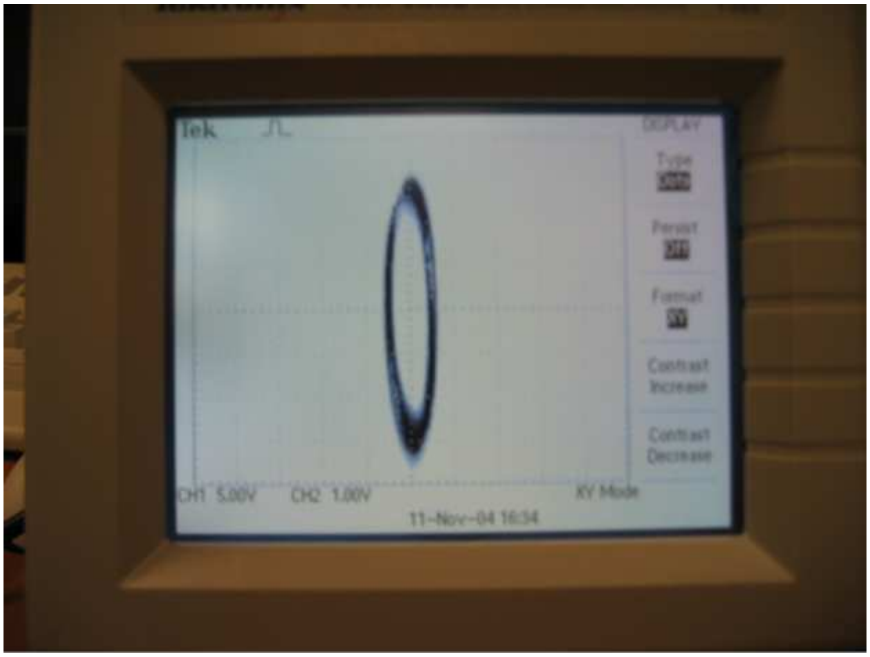

Figure A.5: The $x - y$ "ellipse" from the signals of the two detectors of the homodyne interferometer.

18. Mirrors M3 and M4 were adjusted to maximize the signal strength.

19. If needed, the overlap of the scene and reference beams was improved by finely adjusting the piezo mirror and the temporary mirror. This increased the signal strengths of the detectors.

20. If the outputs of the detectors had unequal amplitude, HWP3 was finely adjusted so that the signal amplitudes were approximately equal.

21. On the oscilloscope, the two signals from the detectors were observed in an $x - y$ plot or Lissajous figure. If the signals were in quadrature then the plot resembled a circle. The voltage setting of one of the channels was set to an extreme so that the circle turned to an ellipse resembling figure A.5. If the major axis of the ellipse was not entirely horizontal or vertical, the signals were not in quadrature. To achieve quadrature, the quarter wave plate QWP was finely adjusted until the major axis of the ellipse became horizontal or vertical.

    The previous step completes the calibration of the interferometer. The next steps describe the process of aligning the scene beam through the vacuum chamber.

22. The temporary mirror in the path of the scene beam was removed, and the mirror M2 at the bottom of the chamber was adjusted to steer the scene beam through the sapphire windows.

23. The spherical mirror on top of the chamber was adjusted so that the reflected beam traced the incoming beam's path. It was helpful to place a temporary translucent screen in the scene beam's path when adjusting the spherical mirror to align the reflected beam. When the spherical mirror was adjusted, quadrature signals were observed on the oscilloscope.

24. If the signal observed on the oscilloscope was low in amplitude, then the interferometer might have been operating at a minimum of the phase auto-correlation function of the laser as discussed in section 4.3. If this is the case, increasing the path length of the scene beam changed the signal amplitude. This could be achieved by moving the optical table back and forth or changing the location of the spherical mirror on its mount.

A.3 Alignment Procedure for the Heterodyne Interferometer

Figure A.6 shows the arrangement of the various optical components of the heterodyne interferometer on the optical bench. The heterodyne interferometer for the Caltech spheromak experiment was aligned by the following sequence of techniques (refer to figure 4.6):

1. The laser beam was set up to be parallel to the optical table.

2. The isolator was placed so that it intercepted the laser beam. Its position was adjusted so that the beam came through the center of the polarizer at the end and its shape was not distorted.

3. Half wave plate HWP1 was placed between the laser and the isolator. To align its optical axis, it was rotated so that the output from the isolator went to a minimum. At this point the polarization of the beam entering the isolator was orthogonal to the

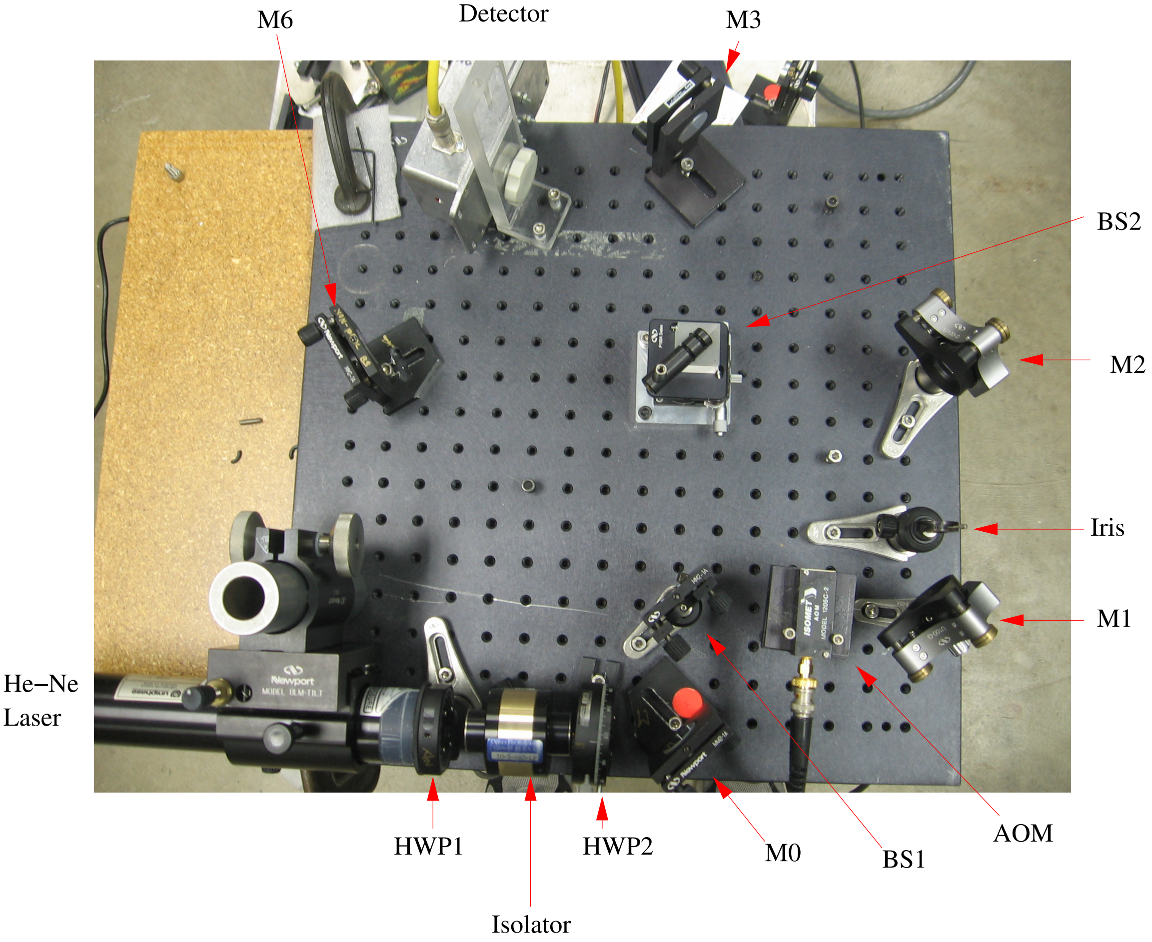

Figure A.6: Image of the 18” × 18” optical table showing the various optical components of the heterodyne interferometer.

axis of the input polarizer of the isolator. To align the polarization, the axis of HWP1 was rotated by an extra 45°.

4. The axis of half wave plate HWP2 was adjusted to vertically polarize the laser beam. The polarization angle was checked using a Wollaston prism.
5. The mirror M0 and beam splitter BS1 were placed at their respective positions.
6. The acousto-optic modulator (AOM) was positioned so that it intercepted the reference beam. It was rotated so that maximum power was coupled into the first harmonic or equivalently so that the first harmonic was the brightest.
7. The iris was placed so that it blocked all beams except for the first harmonic.
8. The mirrors M1, M2 and M3 and beam splitter BS2 were adjusted to steer the beam. Mirror M3 was adjusted to steer the beam onto the center of the aperture of mirror M4.
9. The mirrors M4 and M5 were adjusted to steer the beam through the sapphire windows onto the spherical mirror SM. The process of steering the beam through the windows was easier than the homodyne design due to the extra mirror beneath the chamber (refer to figure 4.4).
10. The spherical mirror SM on top of the chamber was adjusted so that the beam fell back on BS2 as shown in the figure 4.6.
11. Mirror M2 and beam splitter BS2 were adjusted iteratively so that the scene and the reference beams overlapped almost perfectly. This was achieved by the technique described in section A.1.3.
12. Mirror M6 was aligned to direct the interfering beams onto the detector. The RF electronics were switched on, and the quadrature signals were monitored on the oscilloscope. M5 was adjusted to maximize the signal strength.
13. If the signal observed on the oscilloscope was low in amplitude, then the interferometer might have been operating at a minimum of the phase auto-correlation function of the laser as discussed in section 4.3. If so, increasing the path length of the scene

beam changed the signal amplitude. This could be achieved by moving the optical table back and forth or by changing the location of the spherical mirror on its mount.

Bibliography

[1] J. D. Huba. NRL Plasma Formulary. 2002.

[2] ITER, March 2009. URL `http://www.iter.org/`.

[3] Paul M. Bellan. Spheromaks: A Practical Application of Magnetohydrodynamic Dynamos and Plasma Self-Organization. Imperial College Press, 2000.

[4] FESAC Panel Staff. Report of the FESAC toroidal alternates panel. Technical report, November 2008. URL `http://fusion.gat.com/tap`.

[5] P. M. Bellan and J. F. Hansen. Laboratory simulations of solar prominence eruptions. volume 5, pages 1991–2000. AIP, 1998. doi: 10.1063/1.872870. URL `http://link.aip.org/link/?PHP/5/1991/1`.

[6] S. C. Hsu and P. M. Bellan. A laboratory plasma experiment for studying magnetic dynamics of accretion discs and jets. Monthly Notices of the Royal Astronomical Society, 334, 2002. doi: 10.1046/j.1365-8711.2002.05422.x. URL `http://dx.doi.org/10.1046/j.1365-8711.2002.05422.x`.

[7] P. M. Bellan. Fundamentals of Plasma Physics. Cambridge University Press, 2006.

[8] Jeffrey P. Freidberg. Plasma Physics and Fusion Energy. Cambridge University Press, 2007.

[9] L. Woltjer. A theorem on force-free magnetic fields. Proceedings of the National Academy of Sciences of the United States of America, 44(6):489–491, 1958. URL `http://www.pnas.org/content/44/6/489.short`.

[10] J. B. Taylor. Relaxation of toroidal plasma and generation of reverse magnetic fields. Physical Review Letters, 33(19):1139–1141, Nov 1974. doi: 10.1103/PhysRevLett.33.1139. URL `http://link.aps.org/doi/10.1103/PhysRevLett.33.1139`.

[11] Cris W. Barnes, J. C. Fernández, I. Henins, H. W. Hoida, T. R. Jarboe, S. O. Knox, G. J. Marklin, and K. F. McKenna. Experimental determination of the conservation of magnetic helicity from the balance between source and spheromak. Physics of Fluids, 29(10):3415–3432, 1986. doi: 10.1063/1.865858. URL `http://link.aip.org/link/?PFL/29/3415/1`.

[12] S. You, G. S. Yun, and P. M. Bellan. Dynamic and stagnating plasma flow leading to magnetic-flux-tube collimation. Physical Review Letters, 95(4):045002, Jul 2005. doi: 10.1103/PhysRevLett.95.045002. URL `http://link.aps.org/doi/10.1103/PhysRevLett.95.045002`.

[13] S. C. Hsu and P. M. Bellan. Experimental identification of the kink instability as a poloidal flux amplification mechanism for coaxial gun spheromak formation. Physical Review Letters, 90(21):215002, May 2003. doi: 10.1103/PhysRevLett.90.215002. URL `http://link.aps.org/doi/10.1103/PhysRevLett.90.215002`.

[14] Tektronix, Inc., March 2009. URL `http://www.tek.com/`.

[15] DRS Technologies, Inc., March 2009. URL `http://www.drsdi.com/`.

[16] C. A. Romero-Talamás, P. M. Bellan, and S. C. Hsu. Multielement magnetic probe using commercial chip inductors. Review of Scientific Instruments, 75(8):2664–2667, 2004. doi: 10.1063/1.1771483. URL `http://link.aip.org/link/?RSI/75/2664/1`.

[17] Gunsu Soonshin Yun. Dynamics of Plasma Structures Interacting with External and Self-Generated Magnetic Fields. PhD thesis, California Institute of Technology, July 2007. URL `http://resolver.caltech.edu/CaltechETD:etd-07242007-162442`.

[18] P. K. Browning, G. Cunningham, S. J. Gee, K. J. Gibson, A. al Karkhy, D. A. Kitson, R. Martin, and M. G. Rusbridge. Power flow in a gun-injected spheromak plasma. Physical Review Letters, 68(11):1718–1721, Mar 1992. doi: 10.1103/PhysRevLett.68.1718. URL `http://link.aps.org/doi/10.1103/PhysRevLett.68.1718`.

[19] H. S. McLean, S. Woodruff, E. B. Hooper, R. H. Bulmer, D. N. Hill, C. Holcomb, J. Moller, B. W. Stallard, R. D. Wood, and Z. Wang. Suppression of MHD fluctuations leading to improved confinement in a gun-driven spheromak. Physical Review Letters, 88(12):125004, Mar 2002. doi: 10.1103/PhysRevLett.88.125004. URL `http://link.aps.org/doi/10.1103/PhysRevLett.88.125004`.

[20] T. R. Jarboe, W. T. Hamp, G. J. Marklin, B. A. Nelson, R. G. O'Neill, A. J. Redd, P. E. Sieck, R. J. Smith, and J. S. Wrobel. Spheromak formation by steady inductive helicity injection. Physical Review Letters, 97(11):115003, 2006. doi: 10.1103/PhysRevLett.97.115003. URL `http://link.aps.org/abstract/PRL/v97/e115003`.

[21] B. W. Stallard, E. B. Hooper, S. Woodruff, R. H. Bulmer, D. N. Hill, H. S. McLean, R. D. Wood, and SSPX Team. Magnetic helicity balance in the sustained spheromak plasma experiment. Physics of Plasmas, 10(7):2912–2924, 2003. doi: 10.1063/1.1580121. URL `http://link.aip.org/link/?PHP/10/2912/1`.

[22] W. C. Turner, G. C. Goldenbaum, E. H. A. Granneman, J. H. Hammer, C. W. Hartman, D. S. Prono, and J. Taska. Investigations of the magnetic structure and the decay of a plasma-gun-generated compact torus. Physics of Fluids, 26(7):1965–1986, 1983. doi: 10.1063/1.864345. URL `http://link.aip.org/link/?PFL/26/1965/1`.

[23] Ignitron, February 2008. URL `http://en.wikipedia.org/wiki/Ignitron`.

[24] Ignitrons for capacitor discharge and crowbar applications. Personal Copy.

[25] W. James Sarjeant and R. E. Dollinger. High-Power Electronics, chapter 7, pages 231–237. TAB professional and Reference Books, 1989.

[26] GL-7703 product information, March 2009. URL `http://catalog.rell.com/rellecom/Images/Objects/8200/8103.PDF`.

[27] M. Stanway and R. Seddon. Ignitron firing time and jitter. Personal Copy.

[28] S. Woodruff, B. I. Cohen, E. B. Hooper, H. S. Mclean, B. W. Stallard, D. N. Hill, C. T. Holcomb, C. Romero-Talamas, R. D. Wood, G. Cone, and C. R. Sovinec. Controlled and spontaneous magnetic field generation in a gun-driven spheromak. Physics of

Plasmas, 12(5):052502, 2005. doi: 10.1063/1.1878772. URL `http://link.aip.org/link/?PHP/12/052502/1`.

[29] Charles J. Michels and Fred F. Terdan. Characteristics of a 5-kilojoule, ignitron-switched, fast-capacitor bank. Technical report, Lewis Research Center, Ohio, 1965.

[30] Richard C. Dorf and James A. Svoboda. Introduction to electric circuits. John Wiley and Sons, Inc., 2006.

[31] Yun-Sik Jin, Hong-Sik Lee, Jong-Soo Kim, Young-Bae Kim, and G.-H. Rim. Novel crowbar circuit for compact 50-kJ capacitor bank. Plasma Science, IEEE Transactions on, 32(2):525–530, April 2004. ISSN 0093-3813. doi: 10.1109/TPS.2004.826028. URL `http://dx.doi.org/10.1109/TPS.2004.826028`.

[32] Zhehui Wang, Paul D. Beinke, Cris W. Barnes, Michael W. Martin, Edward Mignardot, Glen A. Wurden, Scott C. Hsu, Thomas P. Intrator, and Carter P. Munson. A penning-assisted subkilovolt coaxial plasma source. Review of Scientific Instruments, 76(3): 033501, 2005. doi: 10.1063/1.1855071. URL `http://link.aip.org/link/?RSI/76/033501/1`.

[33] M.E. Savage. Final results from the high-current, high-action closing switch test program at Sandia National Laboratories. Plasma Science, IEEE Transactions on, 28 (5):1451–1455, Oct 2000. ISSN 0093-3813. doi: 10.1109/27.901213. URL `http://dx.doi.org/10.1109/27.901213`.

[34] P. Acedo, H. Lamela, T. Estrada, and J. Sánchez. Operation of a CO_2-HeNe laser heterodyne interferometer in the TJ-II stellarator. volume 24B, pages 1252–1255. 27^{th} EPS Conference on Controlled Fusion and Plasma Physics, June 2000. URL `http://web.gat.com/conferences/meetings/eps00/start.htm`.

[35] Dan R. Baker and Shu-Tso Lee. Dual laser interferometer for plasma density measurements on large tokamaks. Review of Scientific Instruments, 49(7):919–922, 1978. doi: 10.1063/1.1135492. URL `http://link.aip.org/link/?RSI/49/919/1`.

[36] T. N. Carlstrom, D. R. Ahlgren, and J. Crosbie. Real-time, vibration-compensated CO_2 interferometer operation on the DIII-D tokamak. Review of Scientific Instruments,

59(7):1063–1066, 1988. doi: 10.1063/1.1139726. URL `http://link.aip.org/link/?RSI/59/1063/1`.

[37] J. Irby, R. Murray, P. Acedo, and H. Lamela. A two-color interferometer using a frequency doubled diode pumped laser for electron density measurements. Review of Scientific Instruments, 70(1):699–702, 1999. doi: 10.1063/1.1149489. URL `http://link.aip.org/link/?RSI/70/699/1`.

[38] Yasunori Kawano, Akira Nagashima, Katsushiko Tsuchiya, So-ichi Gunji, Shin-ichi Chiba, and Takaki Hatae. Tangential CO_2 laser interferometer for large tokamaks. Journal of plasma and fusion research, 73(8):870–891, June 1997. ISSN 09187928. URL `http://ci.nii.ac.jp/naid/110003826925/`.

[39] Horacio Lamela, Pablo Acedo, the Optoelectronics and Laser Technology Group, and James Irby. Laser interferometric experiments for the TJ-II stellarator electron-density measurements. Review of Scientific Instruments, 72(1):96–102, 2001. doi: 10.1063/1.1333040. URL `http://link.aip.org/link/?RSI/72/96/1`.

[40] Yasunori Kawano, Akira Nagashima, Shinichi Ishida, Takeshi Fukuda, and Tohru Matoba. CO_2 laser interferometer for electron density measurement in JT-60U tokamak. Review of Scientific Instruments, 63(10):4971–4973, 1992. doi: 10.1063/1.1143515. URL `http://link.aip.org/link/?RSI/63/4971/1`.

[41] C. J. Buchenauer and A. R. Jacobson. Quadrature interferometer for plasma density measurements. Review of Scientific Instruments, 48(7):769–774, 1977. doi: 10.1063/1.1135146. URL `http://link.aip.org/link/?RSI/48/769/1`.

[42] D. D. Lowenthal and A. L. Hoffman. Quasi-quadrature interferometer for plasma density radial profile measurements. Review of Scientific Instruments, 50(7):835–843, 1979. doi: 10.1063/1.1135935. URL `http://link.aip.org/link/?RSI/50/835/1`.

[43] Bahaa E. A. Saleh and Malvin Carl Teich. Fundamentals of Photonics. John Wiley and Sons, 1991.

[44] W. B. Bridges. Light sources for optical holography. Private communication.

[45] Anthony E. Seigman. Lasers. University Science Books, 1986.

[46] Robert J. Collier, Christoph B. Burckhardt, and Lawrence H. Lin. Optical Holography. Academic Press, Inc., 1971.

[47] Optics for Research Inc., March 2009. URL `http://www.ofr.com`.

[48] Newport Corporation, March 2009. URL `http://newport.com`.

[49] Analog Modules, Inc., March 2009. URL `http://www.analogmodules.com/`.

[50] Raymond Peter Golingo. Formation of a sheared flow Z-pinch. PhD thesis, University of Washington, 2003.

[51] OSI Optoelectronics, March 2009. URL `http://www.osioptoelectronics.com`.

[52] B. V. Weber and D. D. Hinshelwood. He-Ne interferometer for density measurements in plasma opening switch experiments. Review of Scientific Instruments, 63(10):5199–5201, 1992. doi: 10.1063/1.1143428. URL `http://link.aip.org/link/?RSI/63/5199/1`.

[53] R. Kristal and R. W. Peterson. Bragg cell heterodyne interferometry of fast plasma events. Review of Scientific Instruments, 47(11):1357–1359, 1976. doi: 10.1063/1.1134545. URL `http://link.aip.org/link/?RSI/47/1357/1`.

[54] Gunsu S. Yun, Setthivoine You, and Paul M. Bellan. Large density amplification measured on jets ejected from a magnetized plasma gun. Nuclear Fusion, 47(3):181–188, 2007. URL `http://stacks.iop.org/0029-5515/47/181`.

[55] L. M. Smith, D. R. Keefer, and N. W. Wright. A fiber-optic interferometer for *in situ* measurements of plasma number density in pulsed-power applications. Review of Scientific Instruments, 74(7):3324–3328, 2003. doi: 10.1063/1.1582389. URL `http://link.aip.org/link/?RSI/74/3324/1`.

[56] M. A. Van Zeeland, R. L. Boivin, T. N. Carlstrom, T. Deterly, and D. K. Finkenthal. Fiber optic two-color vibration compensated interferometer for plasma density measurements. Review of Scientific Instruments, 77(10):10F325, 2006. doi: 10.1063/1.2336437. URL `http://link.aip.org/link/?RSI/77/10F325/1`.

[57] John Marshall. Performance of a hydromagnetic plasma gun. Physics of Fluids, 3(1): 134–135, 1960. doi: 10.1063/1.1705989. URL `http://link.aip.org/link/?PFL/3/134/2`.

[58] T. D. Butler, I. Henins, F. C. Jahoda, J. Marshall, and R. L. Morse. Coaxial snowplow discharge. Physics of Fluids, 12(9):1904–1916, 1969. doi: 10.1063/1.1692758. URL `http://link.aip.org/link/?PFL/12/1904/1`.

[59] Kurt F. Schoenberg, Richard A. Gerwin, Jr. Ronald W. Moses, Jay T. Scheuer, and Henri P. Wagner. Magnetohydrodynamic flow physics of magnetically nozzled plasma accelerators with applications to advanced manufacturing. Physics of Plasmas, 5(5): 2090–2104, 1998. doi: 10.1063/1.872880. URL `http://link.aip.org/link/?PHP/5/2090/1`.

[60] K.F. Schoenberg, R.A. Gerwin, I. Henins, R.M. Mayo, J.T. Scheuer, and G.A. Wurden. Preliminary investigation of power flow and performance phenomena in a multimegawatt coaxial plasma thruster. Plasma Science, IEEE Transactions on, 21 (6):625–644, Dec 1993. ISSN 0093-3813. doi: 10.1109/27.256783. URL `http://dx.doi.org/10.1109/27.256783`.

[61] M. Zuin, R. Cavazzana, E. Martines, G. Serianni, V. Antoni, M. Bagatin, M. Andrenucci, F. Paganucci, and P. Rossetti. Kink instability in applied-field magneto-plasma-dynamic thrusters. Physical Review Letters, 92(22):225003, Jun 2004. doi: 10.1103/PhysRevLett.92.225003. URL `http://link.aps.org/doi/10.1103/PhysRevLett.92.225003`.

[62] T. B. Reed. Determination of streaming velocity and the flow of heat and mass in high-current arcs. Journal of Applied Physics, 31(11):2048–2052, 1960. doi: 10.1063/1.1735494. URL `http://link.aip.org/link/?JAP/31/2048/1`.

[63] U. Shumlak, B. A. Nelson, and B. Balick. Plasma jet studies via the flow Z-pinch. Astrophysics and Space Science, 307(1):41–45, Jan 2007. doi: 10.1007/s10509-006-9218-5. URL `http://www.springerlink.com/content/h724757274241160`.

[64] Cris W. Barnes, T. R. Jarboe, G. J. Marklin, S. O. Knox, and I. Henins. The impedance and energy efficiency of a coaxial magnetized plasma source used for spheromak formation and sustainment. Physics of Fluids B: Plasma Physics, 2(8):1871–1888, 1990. doi: 10.1063/1.859459. URL `http://link.aip.org/link/?PFB/2/1871/1`.

[65] James Chen and Jonathan Krall. Acceleration of coronal mass ejections. Journal of Geophysical Research, 108(A11), 2003. doi: 10.1029/2003JA009849. URL `http://dx.doi.org/10.1029/2003JA009849`.

[66] Masanori Nakamura, Hui Li, and Shengtai Li. Stability properties of magnetic tower jets. The Astrophysical Journal, 656(2):721–732, 2007. URL `http://stacks.iop.org/0004-637X/656/721`.

[67] T. Uyama, Y. Honda, M. Nagata, M. Nishikawa, A. ozaki, N. Satomi, and K. Watanabe. Temporal evolution of the decaying spheromak in the CTCC-I experiment. Nuclear Fusion, 27(5):799–813, 1987.

[68] S. C. Hsu and P. M. Bellan. On the jets, kinks, and spheromaks formed by a planar magnetized coaxial gun. Physics of Plasmas, 12(3):032103, 2005. doi: 10.1063/1.1850921. URL `http://link.aip.org/link/?PHP/12/032103/1`.

[69] Deepak Kumar and Paul M. Bellan. Heterodyne interferometer with unequal path lengths. Review of Scientific Instruments, 77(8):083503, 2006. doi: 10.1063/1.2336769. URL `http://link.aip.org/link/?RSI/77/083503/1`.

[70] H. Li, R. V. E. Lovelace, J. M. Finn, and S. A. Colgate. Magnetic helix formation driven by keplerian disk rotation in an external plasma pressure: The initial expansion stage. The Astrophysical Journal, 561(2):915–923, 2001. URL `http://stacks.iop.org/0004-637X/561/915`.

[71] D. Lynden-Bell. On why discs generate magnetic towers and collimate jets. Monthly Notice of the Royal Astronomical Society, 341(4):1360–1372, 2003. doi: 10.1046/j.1365-8711.2003.06506.x. URL `http://dx.doi.org/10.1046/j.1365-8711.2003.06506.x`.

[72] F. J. Weinberg. Optics of Flames. Butterworth, 1963.

[73] Robert C. Weast, editor. Handbook of Chemistry and Physics. CRC Press, 56^{th} edition, 1975.

[74] Francis F. Chen. Introduction to Plasma Physics and Controlled Fusion. Plenum press, 1983.

[75] P. M. Bellan. Why current-carrying magnetic flux tubes gobble up plasma and become thin as a result. Physics of Plasmas, 10(5):1999–2008, 2003. doi: 10.1063/1.1558275. URL `http://link.aip.org/link/?PHP/10/1999/1`.

[76] C. Cote. Power Balance and Characterization of Impurities in the Maryland Spheromak. PhD thesis, The University of Maryland, College Park, 1993.

[77] V. H. Chaplin, M. R. Brown, D. H. Cohen, T. Gray, and C. D. Cothran. Spectroscopic measurements of temperature and plasma impurity concentration during magnetic reconnection at the Swarthmore spheromak experiment. Physics of Plasmas, 16 (4):042505, 2009. doi: 10.1063/1.3099603. URL `http://link.aip.org/link/?PHP/16/042505/1`.

[78] S. Masuda, T. Kosugi, H. Hara, S. Tsuneta, and Y. Ogawara. A loop-top hard x-ray source in a compact solar flare as evidence for magnetic reconnection. Nature, 371: 495–497, October 1994. doi: 10.1038/371495a0. URL `http://dx.doi.org/10.1038/371495a0`.

[79] J. Freddy Hansen. Laboratory Simulations of Solar Prominences. PhD thesis, California Institute of Technology, May 2001. URL `http://resolver.caltech.edu/CaltechETD:etd-08192008-160303`.

[80] J. Freddy Hansen and Paul M. Bellan. Experimental demonstration of how strapping fields can inhibit solar prominence eruptions. The Astrophysical Journal Letters, 563 (2):L183–L186, 2001. URL `http://stacks.iop.org/1538-4357/563/L183`.

[81] D. M. Rust and A. Kumar. Evidence for helically kinked magnetic flux ropes in solar eruptions. The Astrophysical Journal Letters, 464(2):L199–L202, 1996. URL `http://stacks.iop.org/1538-4357/464/L199`.

[82] International Radiation Detectors, Inc., March 2009. URL `http://www.ird-inc.com/`.

[83] Lebow Company, March 2009. URL `http://lebowcompany.com`.

[84] Eric Gullikson. X-ray interactions with matter, March 2009. URL `http://henke.lbl.gov/optical_constants/filter2.html`.

[85] B. L. Henke, E. M. Gullikson, and J. C. Davis. X-ray interactions: Photoabsorption, scattering, transmission, and reflection at E=50 − 30000 eV, Z=1 − 92. Atomic Data and Nuclear Data Tables, 54(2):181–342, July 1993.

[86] R. T. Snider, R. Evanko, and J. Haskovec. Toroidal and poloidal soft X-ray imaging system on the DIII-D tokamak. Review of Scientific Instruments, 59(8):1807–1809, 1988. doi: 10.1063/1.1140119. URL `http://link.aip.org/link/?RSI/59/1807/1`.

[87] X-Ray and Specialty Instruments, March 2009. URL `http://xsiinc.com/`.

[88] Berkeley Nucleonics Corporation, March 2009. URL `http://www.berkeleynucleonics.com/`.

[89] Meade Corporation, March 2009. URL `http://meade.com/`.

[90] J. F. Hansen, S. K. P. Tripathi, and P. M. Bellan. Co- and counter-helicity interaction between two adjacent laboratory prominences. Physics of Plasmas, 11(6):3177–3185, 2004. doi: 10.1063/1.1724831. URL `http://link.aip.org/link/?PHP/11/3177/1`.

[91] E. J. Galvez, March 2009. URL `http://departments.colgate.edu/physics/research/Photon/root/Apparatus/alignment.htm`.